Sister Rod Destructive Examinations (FY23)

Spent Fuel and Waste Disposition

Prepared for
US Department of Energy

Spent Fuel and Waste Science and Technology

Oak Ridge National Laboratory
Rose Montgomery and Bruce Bevard

January 31, 2024
M2SF-24OR010201024
ORNL/SPR-2023/3192

This report was prepared as an account of work sponsored by an agency of the United States Government. Neither the United States Government nor any agency thereof, nor any of their employees, makes any warranty, express or implied, or assumes any legal liability or responsibility for the accuracy, completeness, or usefulness of any information, apparatus, product, or process disclosed, or represents that its use would not infringe privately owned rights. Reference herein to any specific commercial product, process, or service by trade name, trademark, manufacturer, or otherwise, does not necessarily constitute or imply its endorsement, recommendation, or favoring by the United States Government or any agency thereof. The views and opinions of authors expressed herein do not necessarily state or reflect those of the United States Government or any agency thereof.

SUMMARY and STATUS

This report documents work performed under the Spent Fuel and Waste Disposition's Spent Fuel and Waste Science and Technology program for the US Department of Energy (DOE) Office of Nuclear Energy (NE). This work was performed to fulfill Level 2 Milestone M2SF-24OR010201024, "FY23 ORNL Testing on Sibling Pins," within work package SF-24OR01020102 and is an update to the work reported in M2SF-23OR010201024, M2SF-22OR010201047, M2SF-21OR010201032, M2SF-19ORO010201026, and M2SF-19OR010201028.

High-level purpose of this work: As a part of DOE NE High Burnup Spent Fuel Data Project, Oak Ridge National Laboratory (ORNL) is performing destructive examinations (DEs) of high burnup (HBU) (>45 GWd/MTU) spent nuclear fuel (SNF) rods from the North Anna Nuclear Power Station operated by Dominion Energy. The SNF rods, called *sister rods* or *sibling rods*, are all HBU and include four different kinds of fuel rod cladding: standard Zircaloy-4 (Zirc-4), low-tin (LT) Zirc-4, ZIRLO, and M5. The DEs are being conducted to obtain a baseline of the HBU rod's condition before dry storage and are focused on understanding overall SNF rod strength and durability. Composite fuel and defueled cladding will be tested to derive material properties. Although the data generated can be used for multiple purposes, one primary goal for obtaining the post-irradiation examination data and the associated measured mechanical properties is to support SNF dry storage licensing and relicensing activities by (1) addressing identified knowledge gaps and (2) enhancing the technical basis for post-storage transportation, handling, and subsequent disposition. ORNL's tests are performed using fueled segments and complements previous and current test results using defueled cladding segments.

Status: This report documents the status of the ORNL Phase 1 DEs of seven sister rods and outlines the DE tasks performed and the data collected to date, as guided by the sister rod test plans [1,2,3]. Table S-1 summarizes the DE status.

The DEs are performed using a phased approach, and the Phase 1 DEs being performed at ORNL include:

- Full-length rod heat treatments (FHT) of three selected sister rods to examine the effects of temperatures reached during dry storage preparation.
- Rod internal pressure and void volume measurements of the three FHT rods and three corresponding baseline rods, as well as two additional rods selected for depressurization/gas transmission tests and fatigue lifetime tests.
- Fission gas sampling and analysis.
- Depressurization and gas transmission tests.
- Rough segmentation of the selected rods for mechanical tests and rod characterization.
- Fuel sampling and burnup analysis.
- Metallography (MET).
- Cladding total hydrogen measurements.
- Mechanical testing (e.g., Cyclic Integrated Reversible-Bending Fatigue Tester [CIRFT]), four-point bend (4PB), axial tension, microhardness, ring compression, and burst tests).
- Collection and characterization of dust-sized particulate and aerosols released during fuel fracture.
- Experimental waste characterization, packaging, and disposal.

FY23 Accomplishments: The MiniMight (designed and fabricated by ORNL) was installed in the hot cell and one aerosol collection test was completed and the resulting specimens are being analyzed. The results from AERO-1 were further examined and size-specific and isotope-specific release fractions were

calculated. Fixturing has been established for completing the pressurized segment experiments. The four-point bend data recorded during the aerosol collection experiment is being evaluated. A tensile test grip for use with fueled rod specimens was further evaluated out-of-cell and waits for the new load frame for testing to commence. A replacement microhardness tester has been procured and will be ready for hot cell use in FY24. Finite element modeling of the RCT configuration using cracked pellet models provided insight into observations of fracture patterns during fueled RCT testing but greatly overpredicted the load-bearing capability of rods in the transverse direction. Further evaluation of the needed setup for fueled burst tests indicated that the costs outweigh the benefits of the test data, and the program elected to defer the test.

The use of an etchant on fueled microscopy specimens was approved and several specimens have been repolished and etched. The nucleation of cladding hydrides on pellet cracks was observed on several additional views, confirming the FY19 finding. This is an important detail to understand in the context of the overall effect of reoriented hydrides and suggests there are stress concentrations in the cladding at the pellet crack locations, which would not be present when testing for hydride reorientation in empty cladding samples. A specimen from a rod location where a pellet-pellet gap had been observed was analyzed for total cladding hydrogen content, with one specimen taken from the gap area, and three other specimens taken from locations where the pellet was present. A graphical method of calculating the areal hydride fraction was developed and selected views were analyzed.

Detailed isotopic analyses of 12 specimens were completed, as funded by the Nuclear Regulatory Commission, and the results are included herein for completeness.

Post-test calibrations of the in-cell fatigue tester were completed. Non-zero mean strain fatigue testing was completed, and the uncertainties in the strain amplitudes and flexural rigidities were updated. Potential rod-to-rod and rod-to-basket impact loads were further considered and are not expected to cause or exacerbate fatigue damage.

ORNL developed a protocol for disposal of the various types of liquid waste associated with the work and is proceeding with liquid waste disposal.

Table S-1 lists the work performed in FY23 by DE.

Next stages of this work: To complete Phase 1 testing of the selected 7 Sister Rods, the following work must be completed:

- AERO, four more unpressurized tests are planned for FY24. Eight tests using pressurized segments are planned to follow the unpressurized tests in FY24.
- DE.02, optical microscopy (MET): Seven additional MET views are planned.
- DE.03, isotopic analyses: Three more specimens should be completed to characterize the phase 1 rods.
- DE.07, fueled 4PB, and DE.08, fueled axial tension: A replacement load frame has been procured and is expected to be available for continued testing in FY24. We expect to test the new axial tension grip design out-of-cell and then implement it in-cell with the new load frame to complete the 24 planned tension tests of the fueled segments.
- DE.09, Microhardness: Twelve sections remain to be measured for microhardness at elevated temperature.
- Waste disposal – ~5.5 phase 1 rods remain for disposal; 8 other rods are currently in storage pending phase 2 of the work.

Table S-1. DE status.

Planned DE		Status / Applicable Appendix	Comments
FHT	Heat-treat whole rods to 400°C, cool at ≤5°C/hr one ZIRLO, one M5, and one Zirc-4 rod	Complete / Appendix A	Three fuel rods were heat treated: one Zirc-4-clad (F35P17), one ZIRLO-clad (3F9N05), and one M5-clad (30AE14) rod. The target heat-up rates, soak temperatures and times, and cooldown rates were successfully achieved, except for the spent fuel rod heat treatment oven Zone 1 for rod 30AE14 (the upper ~550 mm), which reached temperatures as high as 485°C for approximately 1.75 h during the thermal soak. 30AE14's Zone 1 average temperature during the soak period was 452°C. The maximum pressure during the soak was estimated as 8.0 MPa at the 485°C peak temperature for ~1.75 h. The rod's temperature was corrected before cooldown, and cooldown was as expected.
RS	Segment seven rods	Complete / Appendix B	Test segments were cut from seven Phase 1 sister rods and placed into individual storage capsules. They are not stored in an inert gas atmosphere. Segments are further subsectioned for testing, as needed.
DEF	Defuel segments for Argonne National Laboratory (Argonne)	Complete / Appendix B	Twelve segments slated for testing at Argonne were defueled and shipped.
AERO	Collect aerosol particles released during selected tests	In progress / Appendix I	An aerosol collection system with fixturing and sampling devices was designed to characterize and quantify the respirable fraction of UO_2 particles released during rod fracture. The fixture is used in conjunction with 4PB tests. Modified collection stages were designed and added to a commercially available Sioutas cascade to allow for collection of a larger range of respirable particle diameters. Testing and computational fluid dynamics simulations indicate adequate performance of the system. The first test (AERO-1) was completed in FY22. During the test, 4,615.85 µg of dust-type particulate was collected. 494 µg was collected in the cascade sampler and was within the range of respirable AED. The total airborne release fraction from AERO-1 was calculated as 5.8E-05 ± 4.9E-06, and the

Planned DE		Status / Applicable Appendix	Comments
			respirable fraction was 0.107 ± 0.010. In FY23, a second aerosol collection test was completed, and the resulting aerosol samples are being analyzed. Pressurized specimen tests are planned in FY24.
DE.01	Measure internal pressure of five baseline and three heat-treated rods	Complete / Appendix C	The rod internal pressure and the void volume available inside the rod were measured for eight sister rods at room temperature (RT), and all pressures are within the publicly available database envelope. There is a clear correlation between the post-irradiated rod internal pressure and the as-designed fill pressure. The fission gas partial pressure trends well with the rod average burnup. The pressure and void volumes measured are consistent for rods from the same fuel vendor. The product of the partial pressure of the fission gas and the void volume, P_fV, is consistent from lab to lab for sister rods from the same assembly, except for the two rods from assembly F35. A comparison of P_fV indicates that the ZIRLO-clad rods might have experienced some change in pressure, void volume, or both due to the heat treatment applied, but the M5-clad rods do not exhibit the same effects. Comparisons with predictions from fuel rod performance codes FAST and BISON indicate a tendency for FAST to underpredict pressure and BISON to overpredict pressure.
	Measure rod void volume of five baseline and three heat-treated rods	Complete / Appendix C	Eight rods were measured. All measured volumes are on the lower side of the publicly available database envelope but are consistent with other rods of their design type. By comparing the measured volumes of the baseline and heat-treated ZIRLO-clad rods, as well as the P_fV for all ZIRLO-clad sister rods, it appears that the heat treatment resulted in an increase in void volume. The heat-treated M5-clad rod is within measurement uncertainty of the baseline rod, and the heat-treatment did not appear to affect the void volume. No conclusions could be made about the effects of the heat-treatment on the Zirc-4-clad rod based on a comparison with the LT Zirc-4 baseline rod or the Pacific Northwest National Laboratory Zirc-4-clad rod. Comparisons with predictions from fuel rod performance codes FAST and BISON indicate a tendency for FAST to overpredict void volume and BISON to underpredict void volume.
	Measure the transmissibility	Complete / Appendix C	Pellet stack gas transmissibility at RT was measured by using depressurization tests on eight rods and transmission tests on three rods. In all cases, gas was transmissible through the pellet stack at RT,

Planned DE		Status / Applicable Appendix	Comments
	of gas along the pellet stack		requiring between 30 min and 24 h to reach equilibrium conditions, depending upon the pressure differential applied. The data correlates well using the Muskat-Poiseuille porous media method. The permeability of the pellet stack varied over less than one order of magnitude for this set of rods and could indicate some common feature about HBU fuel. Graphs of the data with burnup, lifetime maximum high duty core index (HDCI), and operating lifetime average assembly middle-of-cycle predicted fuel temperature indicate that the derived permeability is correlated to fuel operating temperature and maximum HDCI but is not correlated to the rod average burnup. The permeability does appear to be closely related to the rod's manufacturer, and the pellet manufacturing process might be important in determining the permeability of the pellet stack. Although the flow regimes associated with the pellet stack transmissibility did not change significantly for the heat-treated fuel rods, it appears that the heat treatments might have induced a shift to higher evaluated permeability. The role of the cladding in the resulting permeability shift is unclear. However, the gas transmission tests do not address the ability of steam to move through the pellet stack or how this flow might compare to the inert gas flow rate. If the cladding was breached during normal operation, pressurized water would be forced into the pellet's interstitial regions or the rod plenum. When placed into dry storage, water in the pellet stack would be available for release. The effectiveness of vacuum drying to remove steam from the stack and the source term associated with the removed steam can be better understood by testing. In FY22, an apparatus was designed, and steam transmission testing was performed on discarded fuel rod segments using the apparatus. Evaluation of the system's performance indicates that over-tightening the seals with the rod segment may reduce or prevent steam flow to the segment, making the quantitative porosity values measured unreliable. However, qualitatively, the tests indicate that steam transmission along the stack is slow in comparison with inert gas and air.
	Collect fission gas samples and analyze	Complete / Appendix C Appendix D	Fission gas samples were collected and analyzed, and results are consistent with publicly available data. ORNL and Pacific Northwest National Laboratory (PNNL) fission gas analyses are consistent with one another, and the data are as expected when differences in fission gas partial pressure are considered. The fission gas released from the pellets to the rod void space ranges from 1.6 to 3.6%.

Planned DE		Status / Applicable Appendix	Comments
DE.02	Perform optical microscopy (MET)	In progress / Appendix B	Cladding/pellet views and measurements are available for all Phase 1 rods. Specific features, including waterside oxide thickness, remaining cladding wall thickness, pellet-side oxide thickness, HBU rim, and cladding inner and outer diameter were measured. Where applicable, comparisons with nondestructive examinations (NDEs) were provided. Section views were inspected for hydride orientation, and radial hydrides are visible in the heat-treated M5-clad specimen and the ZIRLO-clad heat-treated specimen. There is a high hydride density in the heat-treated Zirc-4 specimen, and a large hydride blister was found in one MET view. The few radial hydrides are short. The baseline ZIRLO-clad specimen includes short radial hydrides. The other baseline specimens did not have radial hydrides. An axial MET was created at a pellet-pellet gap. Axial and radial METs do not show a change in the hydride precipitation density through the gap. A section of the cladding was analyzed for total hydrogen content to determine whether the total cladding hydrogen content varies between the pelleted region and the pellet-pellet gap. In FY23, the use of an etchant on fueled specimens was approved by the Irradiated Fuels Examination Laboratory (IFEL), and several specimens have been repolished and etched. Discussions of these specimens have been integrated to Appendix B. The addition of these samples resulted in changes to the previously reported dimensions in Table 2 and Appendix B. The nucleation of cladding hydrides on pellet cracks was observed on several additional views, confirming the FY19 finding. This is an important detail to understand in the context of the overall effect of reoriented hydrides and suggests there are stress concentrations in the cladding at the pellet crack locations, which would not be present when testing for hydride reorientation in empty cladding samples.
DE.03	Perform cladding total hydrogen measurements of selected samples	Complete / Appendix B	All 20 planned Phase 1 priority 1 cladding hydrogen tests have been completed, and the specimen average cladding hydrogen content ranges from 34 to 152 wppm for M5, 130 to 616 wppm for ZIRLO, and 130 to 1,440 wppm for LT Zirc-4/Zirc-4 for clad specimens measured. The results trend well with measured local average waterside oxide layer thickness. In FY23, a specimen from a rod location where a pellet-pellet gap had been observed was analyzed, with one specimen taken from the gap area, and three other specimens taken from locations where the pellet was present. Theory indicates that hydrogen in the cladding should migrate to the gap location because it was colder during operation in the reactor. MET views from the longitudinal specimen did

Planned DE		Status / Applicable Appendix	Comments
			not identify a higher density of hydride precipitates in the gap region. Cladding hydrogen measurements indicate a higher concentration just below the gap location.
	Analyze fuel burnup to confirm predicted and extrapolated values	In progress / Appendix D	Eleven specimens were sent to the ORNL Radiochemical Engineering Development Center for burnup analysis (Nd, U, Pu only). Three are complete. Additionally, other sponsors are funding isotopic analyses of additional sister rod specimens (~51 isotopes measured). Isotopic analyses have been completed for 12 specimens: 3 burnup-only tests funded by DOE and 9 tests funded by NRC. The results are as expected.
DE.05	Perform CIRFT tests to determine static, dynamic, and cumulative effects and fatigue lifetime	Complete / Appendix F Appendix G	Thirty-five tests using CIRFT were completed on 29 specimens. The results are consistent with other rods of the same type that were tested in the past but fall on the lower side of the database, especially the rods with Zirc-4 and LT Zirc-4 cladding. One dynamic test was removed from the fatigue database because, after closer examination of the data, it was determined the rod failed during the preceding static test. The heat treatments applied to selected rods resulted in a shorter fatigue lifetime, which is suspected to be due to reduced flexural rigidity. The flexural rigidity measured for the baseline sister rods is consistent with, although on the lower side of, previously tested 17 × 17 specimens for M5-, ZIRLO-, and LT Zirc-4 clad specimens. The heat-treated rods have a lower flexural rigidity than the corresponding baseline rod, except for the Zirc-4 clad specimens, which have a higher flexural rigidity possibly related to the design's longer pellet length. However, because of the recent calculation of large uncertainty in the CIRFT-measured flexural rigidity values (see Appendix G), there is now less certainty in these observed trends. ORNL replotted the fatigue data in terms of strain amplitude. A strain-based fatigue lifetime limit was developed in Appendix F2 based on the precedents established by O'Donnell and Langer in development of the historic fatigue limits established based on empty cladding and coupon tests of zirconium-based alloys. Strain amplitude was concluded to be more appropriate because it is independent of the composite nature of the fuel rod and because strain is directly measured in the shipping tests that provide representative data for the expected applied fatigue cycles, which means it can be compared directly with the strain amplitude fatigue data. When comparing fatigue data of high

Planned DE		Status / Applicable Appendix	Comments
			burnup fuel rods to zirconium-based alloys or cladding only data, there is a clear observation of degraded fatigue performance. It is suspected that this degradation is due to stress concentration in the cladding where there are discontinuities in the pellet (i.e., cracks or pellet-pellet interfaces). In FY23, post-test calibration checks of the in-cell CIRFT were completed. Non-zero mean strain testing was completed. The uncertainties in the strain amplitudes and flexural rigidities were updated to reflect more recent evaluations, and a discussion was added on why rod-to-rod and rod-to-basket impact loads during normal transportation are not expected to cause or exacerbate fatigue damage.
DE.07	Conduct four-point bend (4PB) tests	In progress / Appendix E Appendix H	All Phase 1 4PB tests are complete except for those planned for aerosol collection. Tests were conducted at room temperature (RT) and at 200°C. The flexural strength and strain at fracture, 0.2% offset yield strength, and flexural modulus were calculated for the tests completed. Generally, the heat-treated M5 and ZIRLO-clad specimens have higher ductility than the baseline specimens, and annealing of irradiation defects resulting from the heat treatments are suspected as a contributing factor to the difference in specimen performance. The mass lost from the specimen resulting from fracture was measured during the 4PB tests. There was no trend of pellet mass loss related to test temperature, although the RT fractures seemed more energetic than the 200°C fracture. Each pellet weighed approximately 5.1–7.0 g, so the maximum mass released from the cladding represents about ¼ of a pellet, whereas the more typical 0.4 g mass released is less than ⅒ of a full pellet. The uncertainty of the 4PB test in ORNL's configuration was calculated and integrated with the results. In the process of calculating the uncertainties, errors in the previously reported (dated 11/30/2020) stress and strain calculations were found and corrected in Section 12.1. To better understand the results of the 4PB tests and the functionality of the pellet in the composite rod in bending, finite element models of the test segment with an explicit crack geometry were developed. The results indicate that pellet-to-cladding bonding and pellet cracks play a large role in the strength of the composite rod.

Planned DE		Status / Applicable Appendix	Comments
			In FY23, the MiniMight test frame was used to perform one 4PB test with aerosol collection. The data are being evaluated. An MTS load frame is being procured.
DE.08	Conduct axial tensile tests	In progress / Appendix E	A tensile test grip for the fuel rod specimen has been developed and is being evaluated out of cell. In cell tests must wait for the new load frame to be installed.
DE.09	Conduct microhardness tests	In progress / Appendix E	Nine specimens have been tested to date (28 indents per specimen) at room temperature. M5 has a lower hardness than the ZIRLO, Zirc-4, and LT Zirc-4 samples that is attributed to M5's recrystallized-annealed microstructure, as opposed to the other alloys, which are cold-worked and stress-relief annealed (CWSRA). CWSRA HV appears to be strongly correlated with estimated local burnup (as a surrogate for fluence). The same cannot be said for M5, but only 3 datapoints are available. Another interpretation of the HV data could be that the FHT resulted in a hardness reduction, especially for the M5 cladding. In FY23, a replacement microhardness tester has been procured and will be ready for hot cell use in FY24 to complete elevated temperature microhardness tests.
DE.10	Conduct fueled ring compression tests (RCT)	Complete / Appendix E	Seventeen fueled RCT tests were completed, including FHT and baseline specimens tested at RT and 200°C. There is no appreciable difference in the maximum load-bearing capability of the segments from RT to 200°C. Cladding type also does not greatly influence the load-bearing capability, and there does not appear to be a difference related to the heat-treatment applied to some of the rods. The main observed variant is the orientation of the major cracks in the pellet because these appear to nucleate fracture of the adjacent cladding and determine the pellet fracture plane. The observed transverse-bearing load of the specimen is 16.4 kN (3,690 lbf) on average, with a minimum load-bearing capability of 12.3 kN (2,766 lbf) for the tested segments. The load-bearing capability of the fueled specimen is about eight times higher than that of a defueled cladding specimen. Finite element modeling of the RCT configuration using cracked pellet models provided insight into observations of fracture patterns during fueled RCT testing but greatly overpredicted the load-bearing capability of rods in the transverse direction. In FY23, additional refinements of the finite element model have improved model predictions.

Planned DE		Status / Applicable Appendix	Comments
DE.14	Perform burst tests	Priority reduced by the program / Appendix E	Existing equipment at the Irradiated Fuels Examination Laboratory (IFEL) is not capable of achieving the pressures needed at the proposed test temperatures. ORNL collaborated with PNNL to design a new system to pressurize segments for burst that is similar to their system, with the exception that ORNL needed to use a gas (due to the intact fuel pellets). In FY22, ORNL developed a pressurization system; however, based on PNNL's burst test results, the system pressure was not high enough to induce burst. In FY23, the work scope priority was reduced and the task has been deferred.
N/A	Leach test	Complete / Appendix J	A leach test was performed using DI water and two fractured post-CIRFT specimens. The results indicate that SNF dissolution follows a trend in which there is an initial instant release of radioisotopes of Cs, Sr, Mo, and Np, followed by a gradual matrix dissolution of U, Pu, Eu, Nd, La, Pr, Sm, and Gd. Less volatile isotopes of Ru, Rh, and Ce are dependent on matrix dissolution in order to be leached. The circumferential samples with less exposed fuel surface area leached more than the axial samples in the majority of the isotopes during the timespan studied. The PCI layer may be more vulnerable to leaching because of its increased quantity of grain boundaries and pores.
N/A	Waste disposal	Ongoing	In FY22, ORNL addressed the method of disposal of acidic liquid and solid wastes, and 78.03 in. of the 2,280 in. of rod length in ORNL's sister rod inventory was packaged for disposal. In FY23, ORNL further developed and demonstrated protocols for disposal of the various types of waste associated with the Sister Rod experimental waste and is proceeding with disposal.

ACKNOWLEDGMENTS

Many thanks to our US Department of Energy Office of Nuclear Energy sponsor, Ned Larson, along with the Spent Fuel and Waste Science and Technology storage and transportation program leadership for their continued support. The sister rod project would not have been possible without the vision and support of the Electric Power Research Institute, Westinghouse, Framatome, and Dominion Energy.

This work would not have been possible without the support and expertise provided by the leadership and staff members of the ORNL's Irradiated Fuel Examination Laboratory.

This page is intentionally blank.

CONTENTS

LIST OF FIGURES

LIST OF TABLES

REVISION HISTORY

Date	Changes
3/29/2019	Initial release.
9/27/2019	Revised to include additional data and incorporate comments from the previously released report.
10/29/2020 (programmatic draft not publicly available)	Revised format of report to include detailed information in appendices and included additional data obtained in FY20. Issued for project review and comment.
11/30/2020	Comments from review of the 10/29/2020 draft were incorporated, the document numbering was revised to reflect its M2 status and the date was changed.
10/29/2021 (programmatic draft not publicly available)	Modified in its entirety: Sections 6, 12.1, 12.2, 12.4, 12.5, 13. Added sections: Section 14 (leach testing). Table 4 was modified to include fission gas release. Other minor changes were made throughout. Added Appendices: G (CIRFT uncertainty calculations), H (four-point bend uncertainty calculations), I (SNF aerosol released during rod fracture); and J (Leach of isotopes from fuel in the presence of deionized water). Updated Appendices: B (Segmentation, defueling, MET, Cladding hydrogen) was updated with the results of cladding hydrogen tests; C (Rod Internal Pressure, Void Volume and Gas Transmission Tests) was updated with fission gas release calculations; E (Mechanical Testing) was updated to include the results of microhardness tests, to add measurement uncertainties to the results, and to correct errors in Table E-2, Table 17, Figure E-10 and Figure E-11; Appendix F (Fatigue Testing) was updated to include measurement uncertainties and to add the results of SEM examinations of the fracture surfaces.
3/31/2022	Comments on the 10/29/2021 document were incorporated and the document date and ID number were revised to reflect its M2 status.
10/28/2022 (programmatic draft not publicly available)	Work completed during FY22 was added in Sections 5, 6, 8.2, 11, 12.1, 12.3, 12.4, 13.2, 13.3, 15, and 16. An error was discovered in a mass calculation in the Section 14 leach testing, and minor changes were made to correct the error. For this draft M3 document, changes and additions to the FY21 report have been highlighted in yellow to aid program review.
1/13/2023	Comments received from the team were incorporated throughout and the document ID number was revised to reflect its M2 status and the issue date was changed

Date	Changes
10/31/2023 (programmatic draft not publicly available)	All sections were updated to address the work completed in FY23. The values in the tables and the graphs presented have been updated to include new information obtained in FY23.
1/31/2024	The IFBA data shown on Figure 9 has been corrected from 0°C to 25°C to be consistent with the rest of the data shown.

ACRONYMS

AERO	aerosol collection capability
AED	aerodynamic equivalent diameter
Argonne	Argonne National Laboratory
CIRFT	cyclic integrated reversible-bending fatigue tester
DE	destructive examination
DEF	defueling
DI	deionized
DOE	US Department of Energy
FGR	fission gas release
FHT	full-length fuel rod heat treatment
FIAP	fractional inventory in aqueous phase
FRR	fractional release rate
FY	fiscal year
GTRF	grid-to-rod fretting
HBU	high burnup
HDCI	high duty core index
HPUF	hydrogen pickup fraction
HV	Vickers hardness
ICP-MS	inductively coupled plasma mass spectroscopy
ID	inner diameter
IFBA	integral fuel burnable absorber
IFEL	Irradiated Fuels Examination Laboratory
IHM	initial heavy metal
LT	low tin
MET	metallography
NE	Office of Nuclear Energy
NDE	nondestructive examination
OD	outer diameter (including the waterside oxide layer)
ONH	oxygen / nitrogen / hydrogen
ORNL	Oak Ridge National Laboratory
PCI	pellet-cladding interaction
PNNL	Pacific Northwest National Laboratory
PV	the product of the rod internal pressure and void volume
PWR	pressurized water reactor
RCT	ring compression test
RT	room temperature
RS	rough segmentation
SEM	scanning electron microscopy
RH	remote-handled

SNF	spent nuclear fuel
SOP	shielded overpack
SRSS	square-root-sum-square
TEM	transmission electron microscope
TRU	transuranic

SPENT FUEL AND WASTE SCIENCE AND TECHNOLOGY
SISTER ROD DESTRUCTIVE EXAMINATIONS

1. Introduction

As a part of the US Department of Energy (DOE) Office of Nuclear Energy (NE) High Burnup Spent Fuel Data Project, Oak Ridge National Laboratory (ORNL) is performing destructive examinations (DEs) of high burnup (HBU) (>45 GWd/MTU) spent nuclear fuel (SNF) rods from the North Anna Nuclear Power Station operated by Dominion Energy. The goals of the High Burnup Spent Fuel Data Project are to "provide confirmatory data for model validation and potential improvement, provide input to future SNF dry storage cask design, support license renewals and new licenses for Independent Spent Fuel Storage Installations, and support transportation licensing for high burnup SNF" [1]. The SNF rods, called *sister rods* or *sibling rods*, are all HBU and include four different kinds of fuel rod cladding: standard Zircaloy-4 (Zirc-4), low-tin Zircaloy-4 (LT Zirc-4), ZIRLO, and M5 [2, 3]. The sister rods have similar characteristics to SNF that was placed in dry storage in a modified TN-32B cask because they were extracted from fuel assemblies of the same design and with similar operating histories (symmetric partners) or from the actual fuel assemblies that are included in the TN-32B cask.[1] Details about the sister rods, their operation in the North Anna Nuclear Power Station, and the HBU Spent Fuel Data Project are provided in References 1 through 4.

The 25 sister rods were subjected to nondestructive examinations (NDEs) at ORNL's Irradiated Fuels Examination Laboratory (IFEL), as described in Montgomery et al. [4]. The NDEs included visual and dimensional inspections, gamma scanning, eddy current, and rod surface temperature measurements. Following the NDEs, 10 of the 25 sister rods were shipped from ORNL to Pacific Northwest National Laboratory (PNNL) for defueled cladding mechanical tests. Several segments from the remaining 15 sister rods at ORNL were defueled and shipped to Argonne National Laboratory (Argonne).

DEs are being conducted to obtain a baseline of the HBU rod's condition before dry storage and to investigate specific conditions of dry storage through small-scale and separate effects tests. The ORNL testing performed is focused on understanding overall SNF rod strength and durability and tested composite fuel and empty cladding to derive material properties. Although the data generated can be used for multiple purposes, one primary goal for obtaining the post-irradiation examination data and the associated measured properties is to support SNF dry storage licensing and relicensing activities by (1) addressing identified knowledge gaps and (2) enhancing the technical basis for post-storage transportation, handling, and consolidation activities.

The 15 rods available at ORNL for DE are described in Table 1. The planned DEs include full-length rod heat treatments simulating the peak dry storage cladding temperature, rod internal pressure and void volume measurements, fission gas analysis and release ratios, fuel burnup, gas transmission testing, metallography (MET), cladding total hydrogen measurements, four-point bend (4PB) and axial tension tests, microhardness tests, ring compression tests (RCTs), and burst tests. The mechanical testing will be performed using fueled segments and is expected to complement previous and current mechanical test

[1] Except for the Zirc-4 rods taken from assembly F35 and the LT Zirc-4 rods taken from assembly 3A1. These rods are not exact sister rods to any rods in the dry storage cask but were the closest available. Furthermore, assembly F35 was operated as a test assembly and was irradiated for four cycles of operation to high burnup.

results for defueled cladding segments. The DE scope necessarily includes preparatory tasks—such as rod segmenting, defueling, and heat treatments—and those activities are discussed within this report.

Throughout this document, the following terms are used:

- *Rod*: the full-length sister rod, unpunctured or punctured, but not segmented, with the exception that a rod used for gas transmission testing (lower end cap removed only) can continue to be called a *rod.*
- *Segment*: a length of cladding with pellets cut from the parent rod to be directly used in testing or to be further modified for use in examinations.
- *Specimen*: a segment modified for use in a DE.
- *Sample*: a small portion of material taken from a segment or specimen for local property testing.

The DEs are performed using a phased approach, as described by Saltzstein [2]. This report documents the status of the ORNL Phase 1 DEs, outlines the DE tasks performed, and documents the data collected to date, as guided by the sister rod test plans [2, 3]. Testing is performed and documented per the requirements of the ORNL sister rod test plan [3], which includes applicable consensus standards (e.g., American Society for Testing and Materials), regulatory requirements (e.g., DOE orders), and adherence to the laboratory and Fuel Cycle Technologies quality assurance plans. In compliance with the ORNL sister rod test plan, measuring and test equipment necessary to conduct the examinations are controlled and calibrated at the facilities that perform the work in accordance with approved laboratory procedures.

Unless otherwise specified, examinations were completed at ambient temperature at standard pressure in air, including those using heat-treated specimens. Throughout the remainder of this document, the sister rods will be described using the format XXXYYY, where *XXX* represents the fuel assembly ID, and *YYY* represents the rod lattice position within the assembly. Individual sister rod segments are described using the format XXXYYY-RRRR-TTTT, where *XXXYYY* is the sister rod ID as previously described, *RRRR* is the lowest original rod elevation of specimen, and *TTTT* is the upper original rod elevation of the segment. If segments longer than 50 mm are subdivided to provide additional test specimens, then the ID is further adjusted to reflect the rod elevations originally occupied by the specimen. This nomenclature is intended to provide traceability to the elevation on the sister rod where each specimen originated.

This report is organized with the primary findings provided in the main body of the document and the more detailed calculations, evaluations, and explanations provided in appendices for each area of DE. Each appendix is meant to be a standalone document that provides all results, including those provided in the main body of the document, and therefore there is some duplicated information between the two.

Additionally, as a status report, this document is updated annually and is cumulative. The most recent release of the report with its appendices contains all data reported throughout the duration of the program.

Table 1. Sister rods selected for DE at ORNL [3].

Clad material	Sister rod	Rod average burnup (GWd/MTU)	Assembly average burnup (GWd/MTU)	Assembly operation	Key characteristics	Cask-stored sister(s)	
						Assembly identifier	Cask rod lattice location
M5	30AG09	53	52.0	30A was operated hot-hot-cold. Its last cycle was uprated ~1.6% about 3 months before the end of the cycle, making it the cycle with the highest power density of those represented. This assembly had the highest pellet enrichment. The assembly design included mid-span mixing grids, which should have lowered the rod operating temperature in the hot spans. All the M5 rods are expected to have relatively low rod internal pressure and cladding hydrogen content.	Sister rod to assembly rod in assembly 57A lance position with close proximity to the peak (hottest) cask rod position (I-7). The rod was operated in a guide tube adjacent location. Of the sister rods, predicted to have the highest decay heat.	57A	I07
M5	30AK09	54			The corresponding cask rod is next to a lance position with close proximity to the peak (hottest) rod position (I-7) in the cask	57A	I07
M5	30AD05*	54			D-5 and E-14 were operated in a guide tube adjacent location with (E-14) and without (D-5) burnable poisons. Because the poisons influence power output during irradiation, the rods are expected to have different characteristics, even though they have similar burnups.	57A	E14
M5	30AE14**	54				57A	D05
M5	5K7O14	53	53.3	5K7 was operated hot-hot-cold and had the highest pellet enrichment of the assembly batches represented. The assembly design included mid-span mixing grids, which should have lowered the rod operating temperature in the hot spans.	Approximately average assembly burnup; the rod was operated in a guide tube diagonal location. All M5 rods are expected to have relatively low rod internal pressure and cladding hydrogen content.	5K6 3K7 5K1	C04
ZIRLO	6U3I07	54	52.7	6U3 was operated hot-cold-cold. The 6U3 sister rods are expected to have relatively high rod internal pressure and cladding hydrogen contents.	This rod is a sister to three different fuel assemblies in the central, middle, and outer regions of the Research Project Cask basket. The rod was operated in a guide tube adjacent location.	3U4 3U9 3U6	I07 I11 I11
ZIRLO	6U3M09	55			This rod's cask sister is next to a lance position	3U4 3U9 3U6	E09
ZIRLO	6U3K09*	55			This rod's cask sister is next to a lance position	3U4 3U9 3U6	K09

Table 1. Sister rods selected for DE at ORNL [3].

Clad material	Sister rod	Rod average burnup (GWd/MTU)	Assembly average burnup (GWd/MTU)	Assembly operation	Key characteristics	Cask-stored sister(s)	
						Assembly identifier	Cask rod lattice location
ZIRLO	3F9N05**	54	52.3	3F9 was operated hot-hot-cold. Both sister rods appear to have experienced grid-to-rod fretting (GTRF) in-reactor; marks were observed at grid locations along the entire axial length. The 3F9 rods are expected to have moderately high rod internal pressure and cladding hydrogen content.	Rod is a good match for several cask rods with a relatively HBU.	4F1 3F6 6F2	N05 N05 N05
ZIRLO	3F9D07	52			Rod with an approximate average assembly burnup	4F1 3F6 6F2	D07
ZIRLO	3D8E14*	59	55.0	3D8 was operated hot-cold-cold. The 3D8 rods are expected to have moderate rod internal pressure and high cladding hydrogen content.	Rod with approximately the highest burnup in assembly and with the highest sister rod burnup.	5D9 5D5	N13 M04
ZIRLO	3D8B02	50			Rod with nearly the lowest burnup in assembly (selected based on pulling restriction).	5D9 5D5	B16 P16
LT Zirc-4	3A1B16	48	50.0	3A1 was burned hot and reached HBUs comparable with the other sister rods in only two cycles.	Rod with the lowest burnup in assembly; close to assembly periphery	OA4***	B16
LT Zirc-4	3A1F05*	51			Rod with the highest burnup in assembly; reasonably close to center of assembly. Areas of CRUD observed.	OA4 ***	F05
Zirc-4	F35P17**	60	57.9	Four cycles of operation. F35 operated its fourth cycle in D-bank with control rods partially inserted. Operated before North Anna's power uprates so lower power density. Lowest enrichment. At time of exams, predicted to have the lowest decay heat.	Rod located on the assembly periphery. Spalled oxide was observed. This rod is expected to have a high rod internal pressure combined with a relatively large cladding hydrogen content.	None (F40) ****	N/A

* Phase 1 baseline rod.
** Phase 1 full length heat-treated (FHT) rod.
*** The LT Zirc-4 rods taken from assembly 3A1 are not exact sister rods to 0A4 but were the closest available.
**** The Zirc-4 rods are not exact sister rods to F40 but were the closest available. Additionally, assembly F35 was operated as a test assembly and was irradiated for four cycles of operation to HBU.

2. Destructive Examination Scope

The Phase 1 DE tasks [2, 3] are as follows.

FHT	Full-length fuel rod heat treatments (FHT) of three sister rods: one ZIRLO, one M5, and one LT Zirc-4.
RS	Rough segmenting of the rods for allocation of segments to DE. Segments are stored in aluminum capsules, in air, until the time of the test.
DEF	Defueling of selected segments. Some segments are defueled as preparation for cladding-only DE; other segments are defueled to gather samples for fuel isotopic and burnup measurements.
AERO	Capture of aerosolized particles released from the segments in which fracture occurs during testing (e.g., 4PB); fixtures and sampling methods are developed to support this effort.
DE.01	Rod internal pressure measurement, rod void volume measurement, collection of fission gas specimens, gas transmission testing, fuel isotopics, and burnup measurements.
DE.02	MET.
DE.03	Cladding total hydrogen measurements.
DE.05	Cyclic integrated reversible-bending fatigue tester (CIRFT) zero mean strain tests in static, dynamic, and cumulative (scope deferred) test modes. Non-zero mean strain tests were identified and added to the program scope in FY22.
DE.07	4PB tests.
DE.08	Axial tension testing.
DE.09	Microhardness tests.
DE.10	RCTs.
DE.14	Burst tests (scope deferred).

DE.04, DE.06, DE.11, DE.12, and DE.13 were deferred to later phases of the test program [2].

Each section of this document summarizes and describes the status and results of the DEs. More detailed information is provided in the appendices.

This page is intentionally left blank.

3. Full-Length Fuel Rod Heat Treatments

In preparation for dry storage, the volume around the fuel assemblies in the canister cavity must be drained and dried. Typically, the most challenging thermal condition experienced by the fuel during dry storage occurs during the drying sequence or just after drying during canister transfer to the storage pad. To better understand the effects of the drying and transfer sequence, three full-length sister rods were subjected to a simulated dry storage peak cladding temperature before DE. A comparison of the FHT rod DE with the baseline rod DE will quantify any impacts related to increased fuel rod temperature before dry storage [1, 2, 3].

The rods were heated slowly (10°C/h), then held at 400°C (all axial elevations) for 8 h, and then slowly cooled (3.7°C/h) to ambient temperature. One Zirc-4-clad (F35P17), one ZIRLO-clad (3F9N05), and one M5-clad (30AE14) rod were heat treated. During heat treatment of the M5-clad rod, the oven controller malfunctioned during the 8 h soak, and the rod plenum end of the oven was at 485°C for ~1.75 h. It is unlikely that the higher temperature affected the behavior of the cladding hydrides because: (1) the M5-clad rod is expected to have very low hydrogen content and (2) the temperature was corrected before the cooldown sequence. The short time at the increased temperature could have resulted in additional annealing of irradiation defects; however, past data [5] indicate that a much longer time at temperature is required. Based on this information, it is unlikely that the short increase in soak temperature will influence the DE results; however, the difference in the heat-treatment conditions will be considered with the results of the DE as it becomes available.

Additional information related to the heat treatments applied is provided in Appendix A.

This page is intentionally left blank.

4. Rough Segmentation and Defueling

Seven Phase 1 rods were rough segmented (RS):

- 30AD05 (M5 clad, baseline),
- 30AE14 (M5 clad, FHT),
- 3D8E14 (ZIRLO clad, baseline),
- 3F9N05 (ZIRLO clad, FHT),
- F35P17 (Zirc-4 clad, FHT),
- 3A1F05 (LT Zirc-4 clad, baseline), and
- 6U3K09 (ZIRLO clad, baseline).

Many segments will be sub-sectioned and/or defueled in the process of specimen preparation for DE. For example, all DE.03 specimens are sub-sectioned from DE.03 segments and then defueled (DEF) before testing. In some cases, the removed fuel is the target of the test (e.g., DE.01 includes burnup measurements).

Appendix B provides details of the RS and DEF processes.

This page is intentionally left blank.

5. Metallography

Metallographic mounts (DE.02) are specified at several elevations of each Phase 1 sister rod to provide supplementary information—such as hydride distribution, oxide thickness, cladding wall thickness, and pellet HBU rim thickness—for correlation with other test data. MET images are available for all seven Phase 1 sister rods, but not all planned elevation views are available. Appendix B provides a list of the planned METs, the status, and a compilation of images and measurements for the completed elevations.

A summary of the available measurement data taken using the MET views is provided by rod and elevation in Table 2. From the group of Phase 1 rods, the Zirc-4 and LT Zirc-4 rods have the minimum remaining cladding wall thickness and maximum measured oxide thickness. For 3A1F05, the minimum remaining cladding wall thickness is 495 µm and the thickest waterside oxide thickness was 128 µm for the same rod, which also had very extensive oxide spalling. For F35P17, which was a 4-cycle lead rod and also had extensive spalling, the minimum remaining wall thickness is 466 µm and maximum waterside oxide thickness of 173 µm. The thickest pellet HBU rim measured is 198 µm for F35P17, consistent with its usage as a lead test rod over four cycles of operation and as the highest burnup sister rod in ORNL's collection. Figure 1 plots the average cladding wall thickness, waterside oxide thickness, and pellet-side oxide thickness for each MET measured as a function of the local estimated rod burnup. Figure 2 plots the average cladding outer diameter (OD), which includes the waterside oxide layer, cladding inner diameter (ID), which includes the pellet-side oxide layer, and pellet HBU rim thickness measured as a function of the local estimated rod burnup. The correlations investigated in Figure 1 and Figure 2 are based on the combined dataset (not by alloy type) and the number of observations is apparent on the plot ($n<30$). As noted in Table 2, the data for each rod is taken from different axial elevations from the rod. The use of burnup as a correlating parameter adjusts for the expected differences in rod performance related to specimen elevation on the fuel rod. Most of the measured performance parameters are also expected to vary azimuthally within the specimen (except for ID and OD) and the number of observations underlying the mean presented in Table 2 range from 3 to 55 observations. Of the parameters plotted with burnup in Figure 1 and Figure 2, those that appear to be correlated, even within the low range of burnup variability within the sister rod collection, are pellet-side average oxide thickness, cladding average ID (which is also assumed to be the pellet OD), and the pellet HBU rim thickness. When OD is sub-grouped by cladding alloy, there might be trends, but there are not enough data points to present a correlation. There does not appear to be an effect related to the FHT for the parameters measured. Generally, the NDE-provided measurements (taken pre-FHT) are consistent with the MET measurements. The MET measurements reported here and in Appendix B are considered to be the most accurate.

One primary application of the METs is visualizing the cladding hydrides and determining whether the applied heat treatments changed the hydride orientation.

- M5-clad rods
    - The hydrides in the baseline M5-clad rod (30AD05) are homogeneously distributed through the thickness of the cladding and are oriented circumferentially.
    - For the FHT M5-clad rod (30AE14), many radial hydrides are visible, particularly at the ID of the cladding. They preferentially precipitated at locations in which a pellet crack exists at the cladding ID.
- ZIRLO-clad rods
    - The precipitated hydrides in the baseline ZIRLO-clad rods are primarily located at the OD and ID of the cladding and are oriented circumferentially. For 3D8E14, there are many short hydrides in the central region of the wall that form a cross pattern, and there are several relatively long radial hydrides located at the cladding ID.

  - For the FHT ZIRLO-clad rod, the circumferential hydrides are more regularly distributed through the wall section, perhaps indicating the migration of hydrogen during FHT, and several radial hydrides are visible at the ID and near the OD of the cladding.

- Zirc-4-clad and LT Zirc-4-clad rods
  - Baseline rod 3A1F05 is heavily spalled, and there is a high density of circumferential hydrides near the waterside surface of the cladding. There is a lower density of circumferential hydrides through the remainder of the wall section. A few short radial hydrides are visible near the cladding ID.
  - The FHT Zirc-4-clad rod contains numerous circumferential hydrides that are visible throughout the thickness of the cladding. The few visible radial hydrides are very short.
  - A hydride blister was discovered on F35P17-2383-2402 and is shown in Figure 3.

Figure 3 provides selected MET images that illustrate the hydride content and orientation for the baseline and FHT sister rods. Additional views and descriptions are provided in Appendix B.

The NDE identified several pellet-pellet gaps among the sister rods. One gap, which was measured at 3 mm long and located at an elevation of 1,403 mm on baseline rod 3D8E14, was sectioned axially to allow for additional examination of the pellet and cladding. MET measurements revealed that the gap is actually less than 1 mm and was overestimated by the gamma scan likely due to the chamfers and dishes in the pellets. The axial view, shown in Figure 4 (also provided in Appendix B), allows axial and radial pellet cracks that occurred during reactor operation to be inspected. The pellet HBU rim is easily discernable and is enhanced at the pellet chamfer locations. The lower pellet has a small chip that relocated within the dish region, and at least one chamfer has loose chips. The axial section was then sectioned radially to view the hydride distribution through the cladding wall. Figure 5 (also provided in Appendix B) provides examples of the hydride distribution in the cladding in the gap and below the gap in the pellet body. There is not a visual difference in the hydride distribution in the gap compared with the cladding in the pellet body below the gap. Total cladding hydrogen measurements were performed in FY23 to better quantify any additional hydrogen (in solution or precipitated) in the pellet-pellet gap region of 3D8E14. The gap region did not contain more hydrogen than the areas within the pellet stack; it actually seemed to have less hydrogen than nearby areas that were in contact with a pellet. But the region just below the gap had a higher concentration of hydrogen. Otherwise, the measurements are consistent with other measurements at other elevations on the same rod. More details are available in Appendix B.

To improve the contrast of the precipitated hydrides in the fueled microscopy images, over the past 2 years, ORNL has been working to gain facility approval for the use of a hydrofluoric acid (HF) etchant. Although the etchant is a standard for use with defueled cladding, there were concerns about the contamination levels of the used etchant and its route for disposal. In September 2022, the first fueled METs were etched. In FY23, ORNL revisited its collection of fueled METs and etched 10 specimens to provide better contrast images. Additionally, 1 new specimen was etched and imaged. The sections were also remeasured, and the results, which are largely consistent with the previously reported dimensions, are reported in Appendix B.

Table 2. Summary of metallographic section measurements obtained to date.

The data provided within the table is based upon multiple measurements of the feature taken from the same metallographic image at different radial locations. Shaded cells indicate that no measurement is available for the specimen image at this time. An asterisk (*) indicates an average value based upon only 2 measurements of that feature from the image. Some features were also measured nondestructively as reported by Montgomery [4] and comparisons are provided in Appendix B, Table B-5. Some METs were imaged but not measured, and they are not included in this table.

Rod ID and original section elevations (mm)			Cladding type	Heat-treated rod?	Estimated local burnup (GWd/MTU)	µm												mm					
						Average measured cladding thickness	Maximum measured	Minimum measured	Average measured waterside oxide thickness	Maximum measured	Minimum measured	Average measured Pellet side oxide thickness	Maximum measured	Minimum measured	Average measured HBU rim thickness	Maximum measured	Minimum measured	Average measured rod Outer diameter	Maximum measured	Minimum measured	Average measured Cladding Inner diameter	Maximum measured	Minimum measured
30AD05	0678	0697	M5	no	58	545	551	540	5	8	4	9	11	6	70	87	54	9.415	9.431	9.403	8.283	8.300	8.268
30AD05	1280	1299	M5	no	59	545	549	541	4	7	2	9	12	6	84	132	51	9.470	9.488	9.446	8.358	8.368	8.339
30AD05	2410	2429	M5	no	59	558	573	546	28	41	20	11	26	6	72	111	48	9.446	9.462	9.432	8.247	8.279	8.230
30AD05	3240	3259	M5	no	55	543	558	535	11	15	3	11	16	7	62	89	43	9.389	9.416	9.374	8.279	8.288	8.273
30AE14	0653	0672	M5	yes	58	564	577	553	6	11	4	12	18	8	89	148	50						
30AE14	1677	1696	M5	yes	60	564	570	558	5	8	3	10	17	6	94	130	74	9.434	9.449	9.424	8.286	8.294	8.278
30AE14	2203	2222	M5	yes	60	561	566	551	9	14	5	8	15	4	106	145	66	9.440	9.466	9.400	8.292	8.296	8.287
30AE14	2675	2694	M5	yes	61	560	575	541	9	10	8	13	18	10				9.389	9.416	9.374	8.279*	8.288	8.273
30AE14	3399	3418	M5	yes	50	562	585	545	12	15	10	10	16	8	61	82	42	9.419	9.449	9.398	8.310	8.338	8.283
3D8E14	700	719	ZIRLO	no	62	569	584	552	7	17	2	9	19	3	90	117	60	9.507	9.521	9.499	8.342	8.359	8.329
3D8E14	1396	1403	ZIRLO	no	64	568	576	564	14	16	10	11	14	6	77	138	42	9.429	9.450	9.418	8.298	8.327	8.281
3D8E14	1403	1406	ZIRLO	no	64	568	577	557	12	12	12												
3D8E14	1406	1409	ZIRLO	no	64	569	580	559	15	16	14	11	17	7	79	110	52	9.471	9.496	9.430	8.326	8.338	8.313
3D8E14	2303	2322	ZIRLO	no	62	560	568	553	19	25	8	12	19	6	101	228	58	9.489	9.532	9.452	8.293	8.310	8.275
3D8E14	2655	2674	ZIRLO	no	64	549	564	531	34	41	31	15	18	12	70	108	52	9.466	9.495	9.424	8.330	8.344	8.306

Table 2. Summary of metallographic section measurements obtained to date, continued.

Rod ID and original section elevations (mm)			Cladding type	Heat-treated rod?	Estimated local burnup (GWd/MTU)	Average measured cladding thickness	Maximum measured	Minimum measured	Average measured waterside oxide thickness	Maximum measured	Minimum measured	Average measured Pellet side oxide thickness	Maximum measured	Minimum measured	Average measured HBU rim thickness	Maximum measured	Minimum measured	Average measured rod Outer diameter	Maximum measured	Minimum measured	Average measured Cladding Inner diameter	Maximum measured	Minimum measured
						µm												mm					
3D8E14	3206	3225	ZIRLO	no	59	545	555	537	47	57	24	10	15	4				9.503	9.520	9.467	8.310	8.314	8.305
6U3K09	2616	2635	ZIRLO	no	58	560	571	549	21	22	19	9	12	6	59	107	36	9.440	9.455	9.425	8.276	8.302	8.249
6U3K09	3506	3525	ZIRLO	no	43	560	566	550	27	31	23	10	15	7				9.401	9.424	9.394	8.250	8.255	8.243
3F9N05	0700	0719	ZIRLO	yes	56	563	569	556	8	11	3	11	16	7	78	121	46	9.441	9.456	9.419	8.286	8.306	8.267
3F9N05	2300	2319	ZIRLO	yes	57	567	577	559	19	26	4	10	16	5	95	111	75	9.427	9.440	9.422	8.310	8.321	8.296
3F9N05	2863	2882	ZIRLO	yes	58	554	563	547	30	38	24	12	16	8				9.450*	9.450	9.449	8.277*	8.277	8.275
3F9N05	3331	3350	ZIRLO	yes	51	554	559	544	39	60	27	9	12	6	35	51	27	9.480*	9.496	9.464	8.271*	8.271	8.270
3A1F05	1260	1279	LT Zirc-4	no	56	560	565	555	15	18	14	10	12	7	54	74	43	9.436*	9.436	9.436	8.299*	8.299	8.299
3A1F05	1585	1604	LT Zirc-4	no	56	550	558	538	29	33	26	11	14	10	71	95	48	9.438	9.468	9.422	8.312	8.320	8.299
3A1F05	2383	2402	LT Zirc-4	no	55	530	547	518	70	89	52	10	16	6	74	105	46	9.461	9.483	9.435	8.290	8.300	8.285
3A1F05	2735	2754	LT Zirc-4	no	54	518	630	494	94	128	43	12	17	9	61	90	38	9.485*	9.548	9.421	8.290*	8.300	8.280
3A1F05	3105	3124	LT Zirc-4	no	53	517	523	508	75	98	27	10	16	6	85	100	70	9.489	9.532	9.452	8.293	8.310	8.275
F35P17	1300	1319	Zirc-4	yes	65	539	548	530	47	68	27	10	14	5	88	119	68	9.480	9.499	9.468	8.291	8.292	8.287
F35P17	2383	2402	Zirc-4	yes	66	492	505	479	47	146	8	11	15	7	78	95	65	9.367	9.521	9.283	8.282	8.288	8.269
F35P17	2735	2754	Zirc-4	yes	66	524	591	510	81	86	73	15	27	10	101	115	94	9.438	9.517	9.385	8.319	8.366	8.274
F35P17	3050	3069	Zirc-4	yes	65	485	503	466	93	173	8	14	29	7	165	198	137	9.391	9.631	9.304	8.335	8.360	8.316

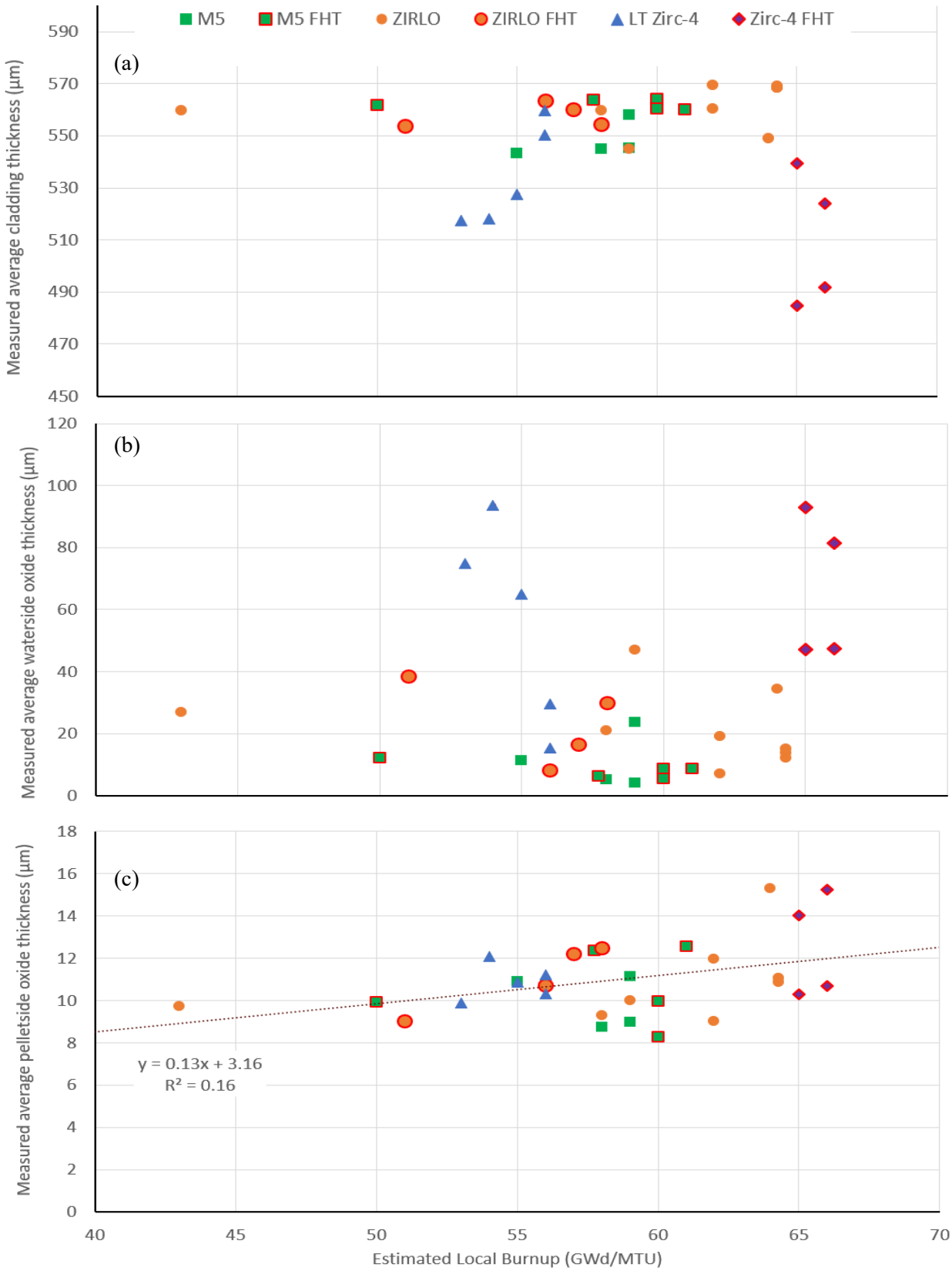

Figure 1. Metallographic measurements vs. estimated local burnup available for the Phase 1 rods: (a) remaining average cladding thickness, (b) average waterside oxide thickness, and (c) average pellet-side oxide thickness.

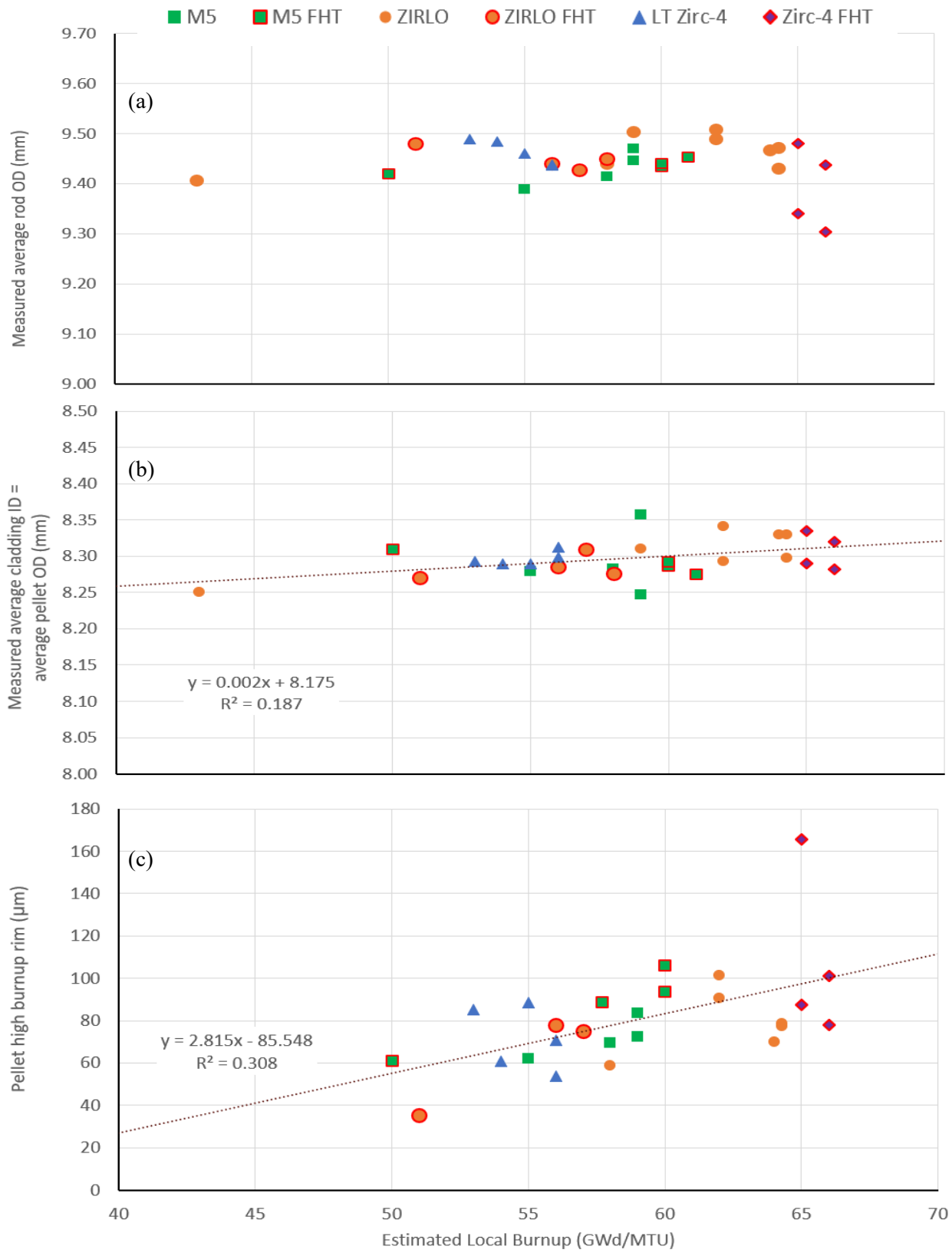

Figure 2. Metallographic measurements vs. estimated local burnup available for the Phase 1 rods: (a) average cladding OD, (b) average cladding ID, and (c) average pellet HBU rim thickness.

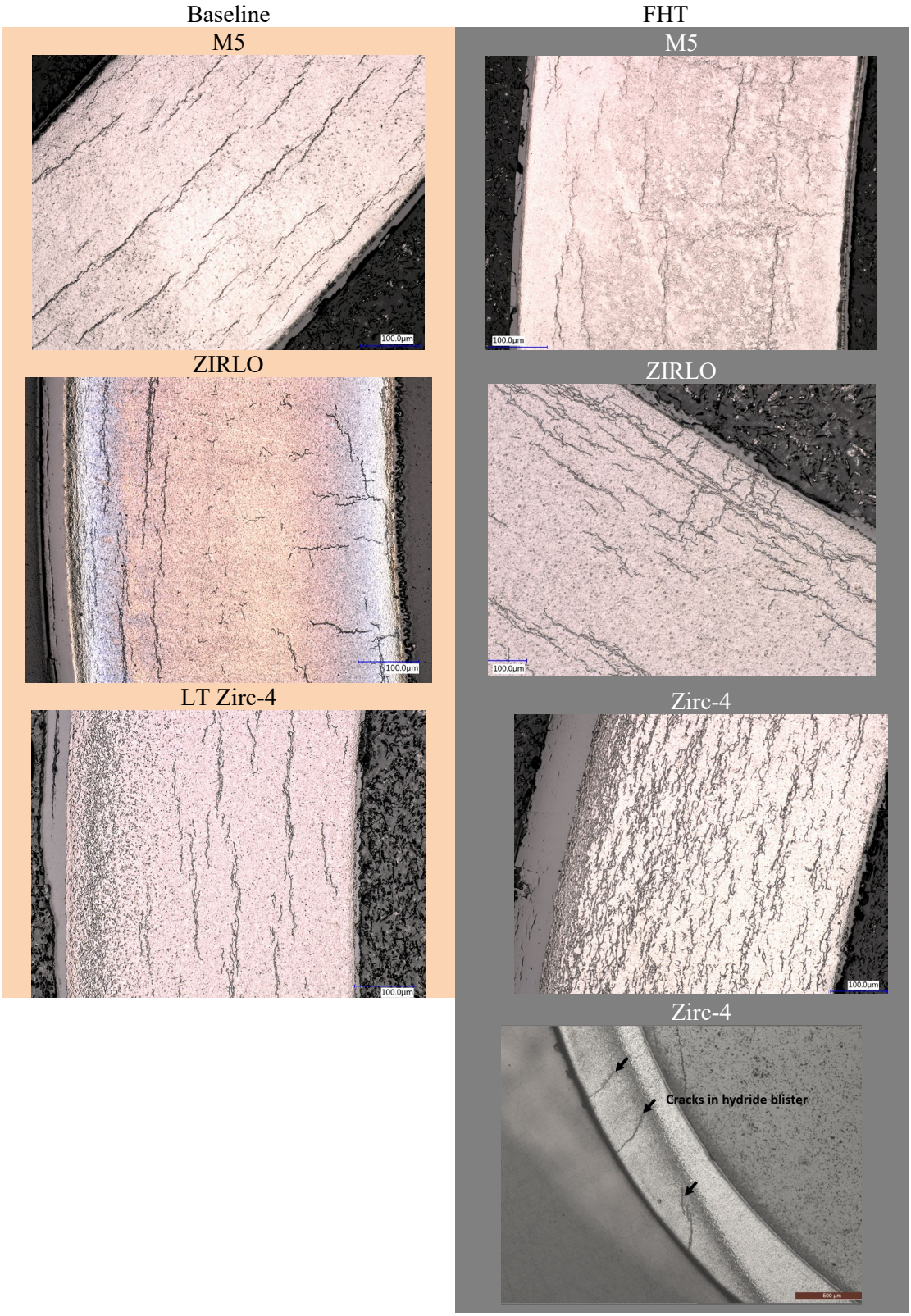

Figure 3. Selected METs illustrating primary hydride content and orientations for baseline and FHT sister rods.

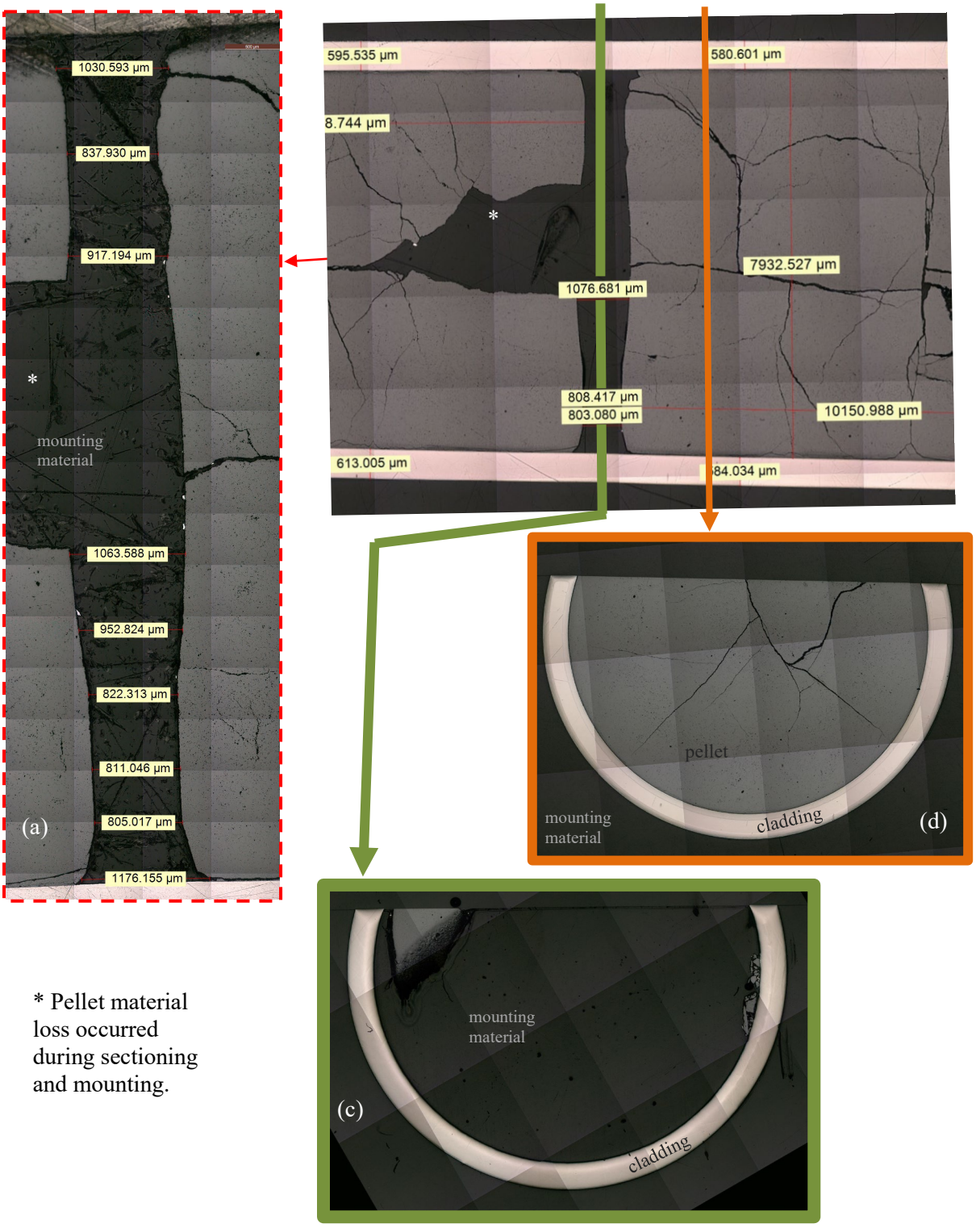

Figure 4. 3D8E14 at 1,403 mm elevation; (a) pellet-pellet gap measurements, (b) cropped axial section view and cross-sectional view locations, (c) cross-sectional view in the pellet-pellet gap, and (d) cross-sectional view of the pellet above the pellet-pellet gap.

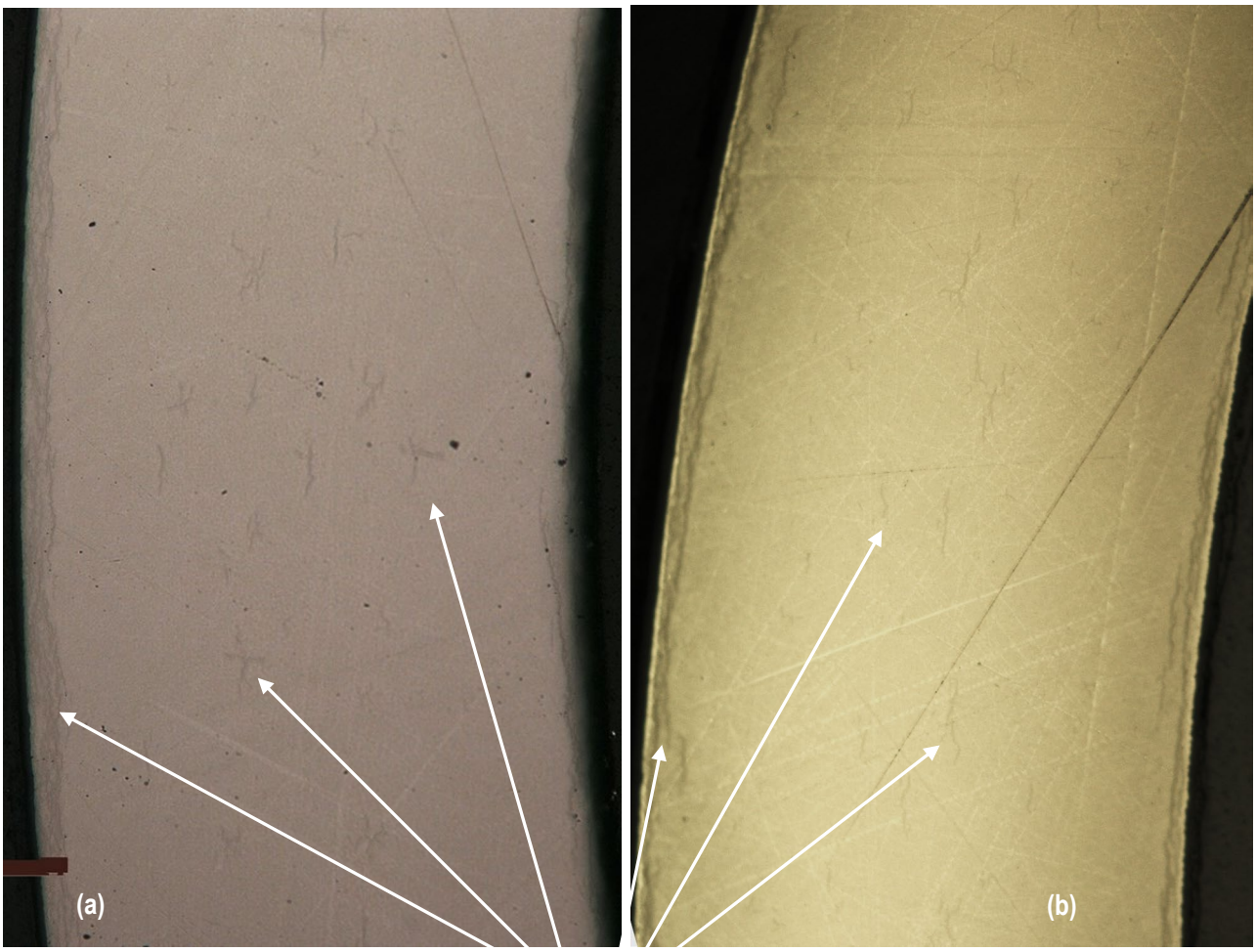

Figure 5. 3D8E14 centered at 1,403 mm elevation; cladding hydride distribution (a) in the pellet-pellet gap and (b) below the pellet-pellet gap in the pellet body.

This page is intentionally blank.

6. Cladding Hydrogen Measurements

All 20 of the planned Phase 1 priority 1 tests have been completed, and the results are tabulated in Table 3. Each specimen was cut from the parent segment using a slow-speed saw, defueled, and then subsectioned to provide an azimuthal sample for each quadrant (0, 90, 180, and 270°). Although the quadrants are not traceable to the position in the reactor, the azimuthal measurements can provide some indications of variations in cladding hydrogen content resulting from in-reactor temperature differences around the rod's circumference. A more detailed discussion of the method used to measure the total cladding hydrogen can be found in Appendix B, Section B-4.

Figure 6 plots the mass-weighted average measured cladding hydrogen concentration as a function of the local waterside oxide layer thickness, and as expected, the two are highly correlated. Figure 7 plots the average specimen's measured hydrogen content as a function of burnup with available previous measurements. The M5 data are slightly higher than previous data [27]. The Zirc-4 cladding data are higher than the previous envelope of data [27], but it should be remembered that F35P17 was a lead rod operated over 4 cycles to HBU. Previous data as a function of burnup are not currently available for comparison with the ZIRLO and LT-Zirc-4 data. In general, the measured cladding hydrogen concentration for the Sister Rods is higher than publicly available data [27,28]. The ORNL hydrogen concentration data are consistent with the PNNL hydrogen concentration results from the same set of fuel rods [29]. At present, there is no explanation for this finding. Additional measurements are planned.

The hydrogen pickup fraction (HPUF) in % was calculated and is listed in Table 3 and graphed in Figure 8 as a function of local waterside oxide thickness. The hydrogen pickup is generally consistent with available data. The oxide thickness used in the calculation is the MET-measured local average oxide thickness when available (Appendix B) and the nondestructively measured local average oxide thickness [4] when a nearby MET is not available.

Table 3. Average hydrogen content and pickup for samples measured to date.

Parent segment ID	Specimen ID	Cladding Alloy	Estimated local burnup (GWd/MTU)	4-quadrant average measured oxide thickness (μm)[a]	4-quadrant average measured hydrogen content (wppm)[b]	Average HPUF (%)[c]
30AD05-1280-1299	OH2	M5	59	4	34 ± 3	16.8 ± 9.3
30AD05-2410-2429	LH	M5	59	28	61 ± 3	4.4 ± 1.7
30AD05-3240-3259	AH	M5	55	12	142 ± 9	24.3 ± 13.6
30AE14-1677-1696	PH	M5	60	6	42 ± 15	15.5 ± 9.2
30AE14-2675-2694	JH2	M5	61	9	94 ± 5	21.4 ± 2.7
30AE14-3399-3418	BH	M5	50	12	152 ± 10	24.9 ± 4.6
3D8E14-2655-2674	HH	ZIRLO	63	34	495 ± 183	23.4 ± 8.4
3D8E14-3206-3225	CH	ZIRLO	59	47 / 49[d]	616 ± 59	32.2 ± 9.7[e]
3F9N05-1425-1444	MH	ZIRLO	59	13	130 ± 2	17.1 ± 7.6
3F9N05-2863-2882	DH	ZIRLO	58	30	395 ± 17	19.5 ± 7.9
3F9N05-3331-3350	IH	ZIRLO	51	39	594 ± 50	28.3 ± 11.2
3A1F05-1260-1279	SH	LT Zirc-4	56	15	130 ± 4	24.5 ± 4.9
3A1F05-1585-1604	UH	LT Zirc-4	56	29	278 ± 108	20.9 ± 0.5
3A1F05-2006-2025	QH	LT Zirc-4	56	64	572 ± 191	26.2 ± 6.4
3A1F05-2383-2402	NH	LT Zirc-4	55	70	680 ± 204	30.4 ± 13.2
3A1F05-2735-2754	GH	LT Zirc-4	54	90 / 107[d]	1,293 ± 126	17.2 ± 2.5[e]
3A1F05-3105-3124	EH2	LT Zirc-4	53	75 / 88[d]	667 ± 280	18.6 ± 7.5[e]
F35P17-1300-1319	RH	Zirc-4	65	47	449 ± 193	16.6 ± 5.6
F35P17-2735-2754	FH	Zirc-4	66	81	870 ± 242	19.8 ± 6.4
F35P17-3050-3069	KH	Zirc-4	65	93 / 154[d]	1,440 ± 245	25.6 ± 11.9[e]
3D8E14-1375-1450[f]	1396-1399 (below gap)	ZIRLO	64	15	157 ± 10	16.5 ± 10.5
3D8E14-1375-1450[f]	1400-1403 (below gap)	ZIRLO	64	14	216 ± 14	18.4 ± 11.3
3D8E14-1375-1450[f]	1403-1406 (gap)	ZIRLO	64	12	115 ± 7	20.0 ± 5.8
3D8E14-1375-1450[f]	1406-1409 (above gap)	ZIRLO	64	15	131 ± 9	26.8 ± 24.2

a. See Table 2 and Appendix B Section B-3 for more information on the oxide thickness measurements.

b. The uncertainty shown is the standard deviation of the 4 quadrant measurements as discussed in Section B-4.2 and may reflect expected variations in oxidation and hydrogen content around the circumference of the fuel rod.

c. The average HPUF is based on the average remaining cladding wall thickness and the average measured waterside oxide layer thickness, excluding measurements of spalled or peeled regions of the oxide. The uncertainty shown is based on the uncertainty of the parameters used in the average HPUF calculation. See Appendix H, Section H-3 for the uncertainty calculational approach.

d. Average / average excluding measurements where spalling occurred.

e. Calculation of the HPUF is based upon the average measurement of waterside oxide layer excluding spalled or peeled regions of the oxide.

f. This segment was identified as containing a pellet-pellet gap. After longitudinal sectioning, the exact location of the gap was revealed and specimens were cut in the gap (1,403 to 1,406 mm in elevation from rod bottom), below the gap (1,396 to 1,403 mm in elevation), and above the gap (1,406 to 1,409 mm in elevation). These specimens were analyzed individually. Specimens above and below the gap were in contact with a pellet during operation, while the gap region was not. The uncertainty of the hydrogen content measurement is the standard deviation of the measurements at the 4 elevations per the discussion in Appendix B Section B-4.2.

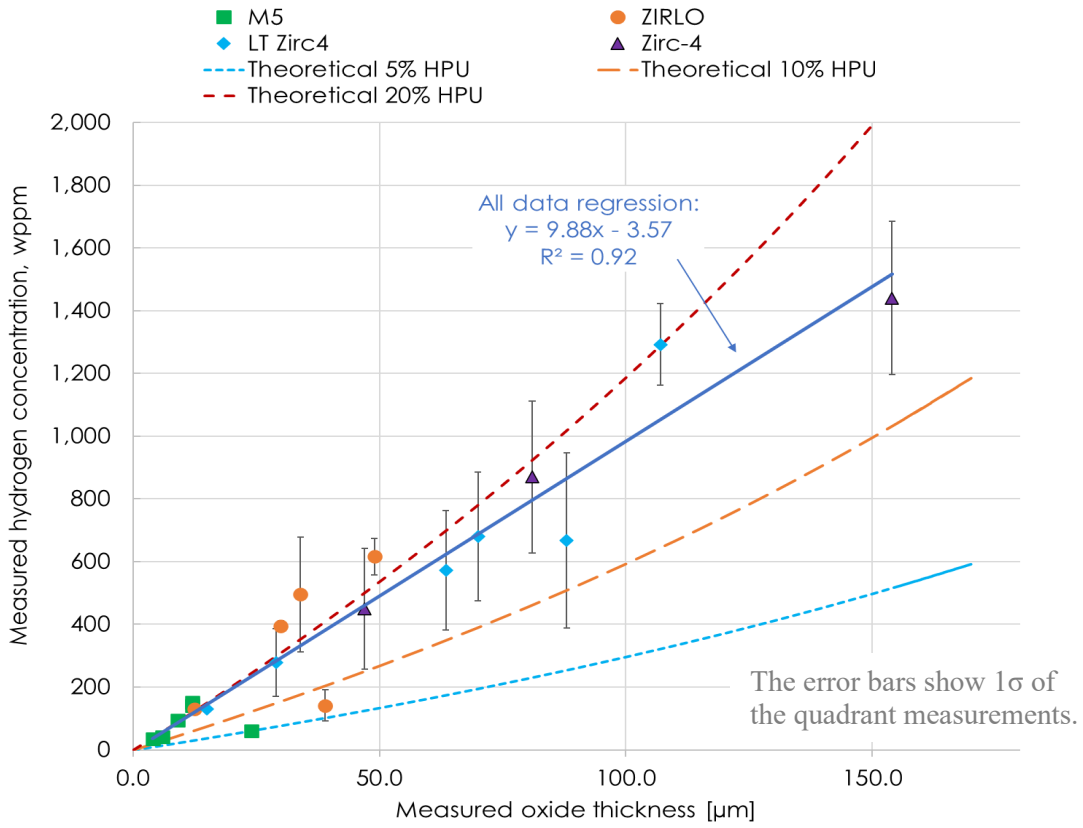

Figure 6. Mass-weighted average measured cladding hydrogen content as a function of measured average local oxide thickness.

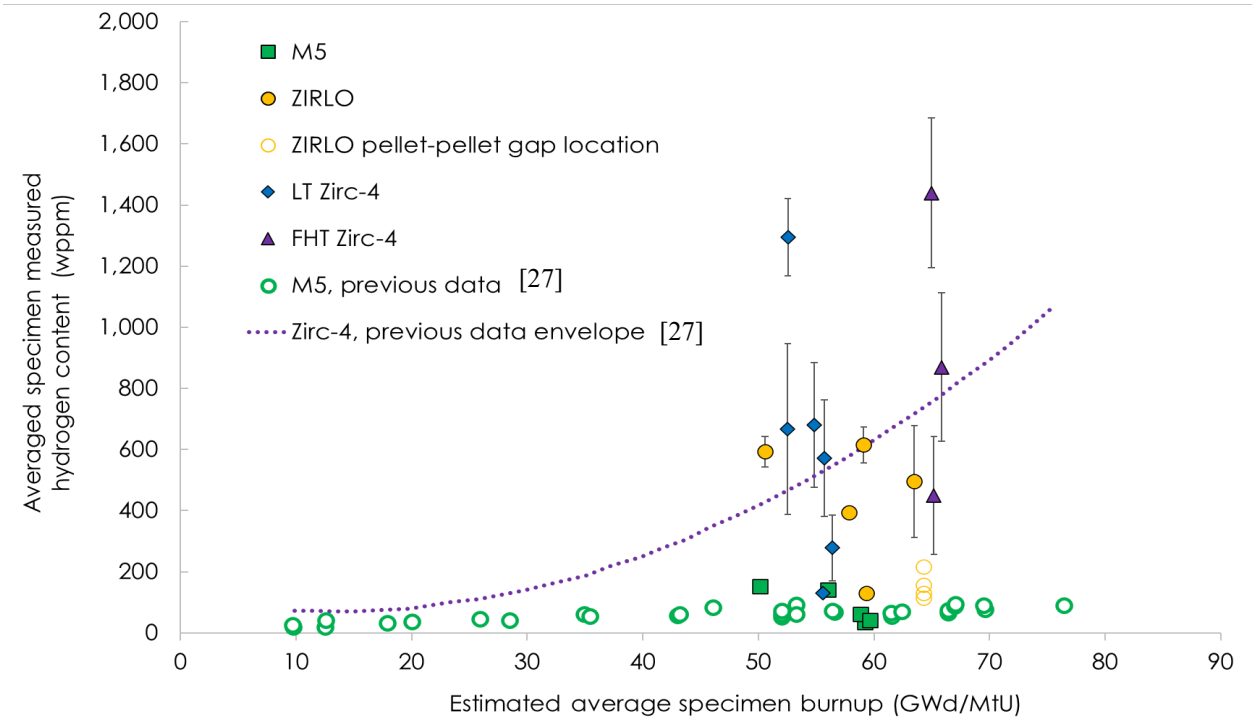

Figure 7. Average specimen's measured hydrogen content as a function of estimated local burnup by alloy and with available previous data.

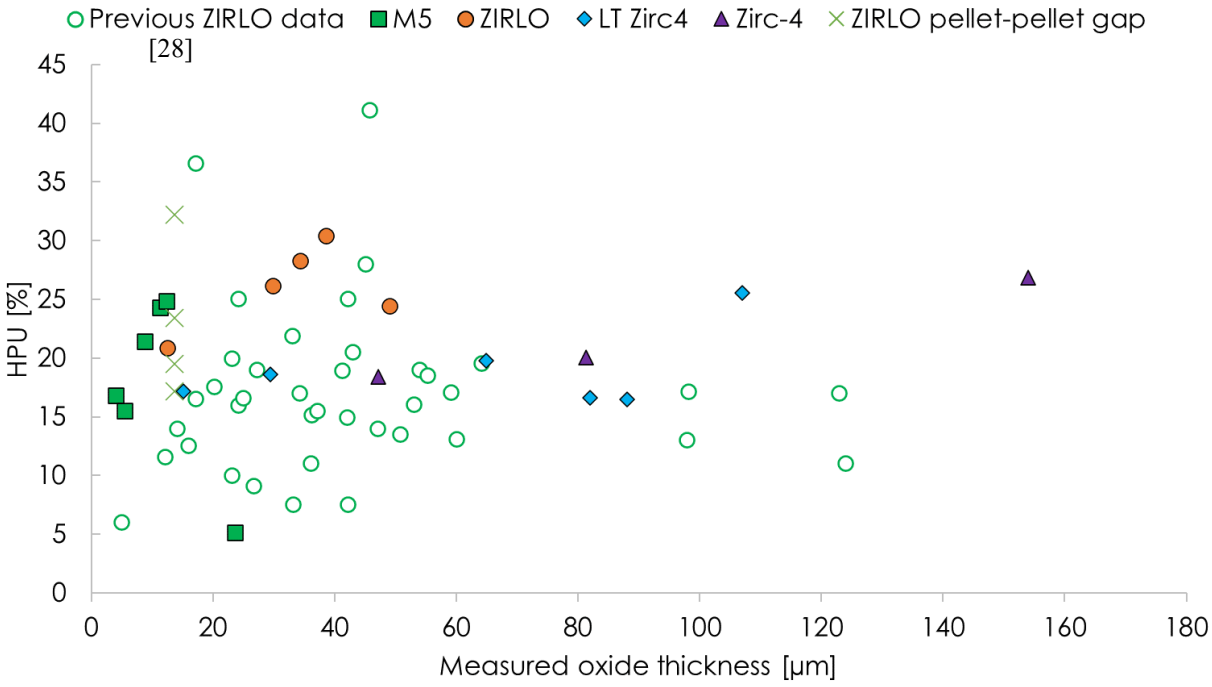

Figure 8. Cladding hydrogen pickup as a function of local oxide thickness.

7. Rod Internal Pressure Measurement and Rod Void Volume Measurement

Commercial nuclear fuel rods are pre-pressurized with helium before irradiation. The magnitude of pre-pressurization varies with fuel design; at manufacture, the sister rods were pre-pressurized between 1.7 and 2.5 MPa, depending on their design. Each fuel rod includes a spring in a plenum at the top of the rod to provide a small compression load on the fuel pellet stack inside the rod, mainly to ensure that gaps between pellets do not occur. During irradiation and subsequent storage, the rod internal pressure increases due to the production of fission gases (e.g., xenon, krypton) and volumetric changes resulting from swelling and irradiation growth. At manufacture, the rod includes spaces that are unoccupied by the fuel stack and spring, termed the *void volume*. The void volume changes during operation as the cladding creeps and grows due to irradiation and as cracks and porosity are formed within the pellets. For purposes of this discussion, the void volume is defined as including the volume in the plenum of the rod that is not occupied by the spring, the gap between the pellet OD and the cladding ID, the volume of any pellet chamfers and dishes, and the volume of pellet cracks and open porosity at the specified temperature. Because rod internal pressure and void volume are important parameters in determining rod performance throughout its lifetime, both were measured for each of the sister rods.

The gas pressure and void volume of a fuel rod was measured by puncturing the plenum region of the rod and using the ideal gas law in conjunction with known pressures and volumes. The plenum end of the fuel rod is sealed into an evacuated housing of known volume (the "tare" volume). After puncture, the pressure in the housing was measured. Then the gas was expanded into another chamber of known volume, and the new pressure was measured. This double expansion method allowed the rod's internal pressure and free internal volume to be determined. Once measurements were completed, the housing and now-accessible free rod volume were evacuated and backfilled with a known volume and pressure of gas, and the final gas pressure was measured. This process allowed a second two-step measurement of the rod's void volume and a second calculation for the rod's internal pressure. Appendix C discusses the design of the puncture system, system testing, experimental uncertainties, data analysis techniques, and many other important considerations in the highly sensitive measurement system used in the ORNL IFEL hot cell. The Phase 1 rod measurements, detailed data analysis, and comparisons with historical data are also provided in Appendix C.

The results of the rod internal pressure and void volume measurements for the eight sister rods punctured to date are summarized in Table 4 along with the 2σ uncertainty. The rod puncture left a very small hole in the plenum region of the rod, estimated to be less than 0.5 mm in diameter. The sister rod internal pressure is within the envelope of the available previous data [6] and is consistent with measurements of the 10 sister rods measured at PNNL [7]. Likewise, the sister rod measured void volumes are within the extents of past measurements [6] and are consistent with the sister rod measurements completed by PNNL [7]. The measured sister rod internal pressures are lower than four available data points for Westinghouse 17 × 17 rods that were fabricated with an Integral Fuel Burnable Absorber (IFBA) coating[2] on the fuel pellets [8]. None of the sister rods had IFBA coatings, but otherwise the IFBA rods are very similar to the sister rods. The FHT Zirc-4-clad sister rod, F35P17, was expected to be atypical because it was operated to HBU for four cycles as a lead test rod, but the measured results are well within the bounds of the previous data. The results are plotted with other available data in Figure 9.

[2] The coating is typically a thin layer of zirconium diboride on the OD of the pellets that is used for reactor reactivity control during reactor operation.

Table 4. Results of rod internal pressure and void volume measurements at 25°C with calculated fission gas release percent.

Rod ID	Cladding	Average Rod Burnup (GWd/MTU)	Pre-pressurization (MPa)	Measured pressure, two-step (MPa)	2σ (95% confidence interval) uncertainty	Volume (cc)	2σ (95% confidence interval) uncertainty	% Fission gas release
30AK09	M5	53	1.7	3.46	2.5%	9.89	4.0%	1.9
30AD05	M5	54	1.7	3.46	2.7%	10.63	3.7%	1.8
30AE14*	M5	54	1.7	3.22	2.6%	10.99	3.6%	1.8
3D8E14	ZIRLO	59	2.0	4.18	2.4%	11.73	3.4%	3.6
3F9N05*	ZIRLO	54	2.0	3.98	2.2%	12.74	3.2%	3.6
6U3K09	ZIRLO	55	2.0	3.64	2.5%	11.78	3.5%	1.6
3A1F05	LT Zirc-4	51	2.0	3.73	2.2%	12.94	3.2%	3.3
F35P17*	Zirc-4	60	2.5	4.68	3.8%	13.32	4.8%	N/A**

* The rod was heat-treated, as described in Section 3.
** Inventory predictions are not available.

The calculated partial pressure of the fission gas (i.e., the measured rod internal pressure minus the rod design pre-pressurization as adjusted for the change in void volume) with rod average burnup yields similar information, indicating a strong uptick in void volume fission gas partial pressure between 50 and 60 GWd/MTU. The rod internal pressure and rod void volume are specific to each vendor design/cladding type. For example, the Framatome-designed rods are consistent with each other, and the Westinghouse ZIRLO rods are consistent with each other, and there is a strong correlation between the end-of-life and beginning-of-life pressures ($R^2 > 0.6$)[3]. As discussed in Appendix C Section C-6.2, other parameters—such as the rod average burnup, assembly duty, average fuel temperature, and maximum fuel temperature—are not as strongly correlated ($0.4 < R^2 < 0.6$). This is likely due to the lack of a variety within the sister rods with respect to those parameters. The range of burnup within the group of rods is small, the dataset is small, and—considering measurement uncertainties and inaccuracies in available rod design and operational data—correlations with these parameters are not conclusive. When considering only the fission gas partial pressure, the design and operational data are correlated at about the same quality ($R^2 \approx 0.4$). More operating data for rods at other conditions are required to further correlate the measured pressure and volume data within the context of power operation.

[3] R^2 is used in ORNL's data evaluations as an indicator of correlated parameters. The value of R^2 that is indicative of a correlation between two parameters differs depending on the application. Information about the use of R^2 as an indicator of goodness of fit and examples of values used within the community are available in references [31 to 34]. In this work, we are not trying to rigorously define a correlation, imply that the proffered trend (e.g., linear with burnup) is the best mathematical form of the correlation, or suggest that the parameter is the only variable that could be correlated.

As a further comparison point, the product of the fission gas partial pressure and volume (P_fV) was examined because it tends to neutralize any lab-specific biases in the available data. The P_fV is relatively consistent for all Phase 1 sister rods except for a single data point: the Zirc-4-clad rod that was punctured in the pellet stack, F35K13 [7]. The sister rod data are consistent with the historical database, including a change in slope occurring between 50 and 60 GWd/MTU, as shown in Figure 9.

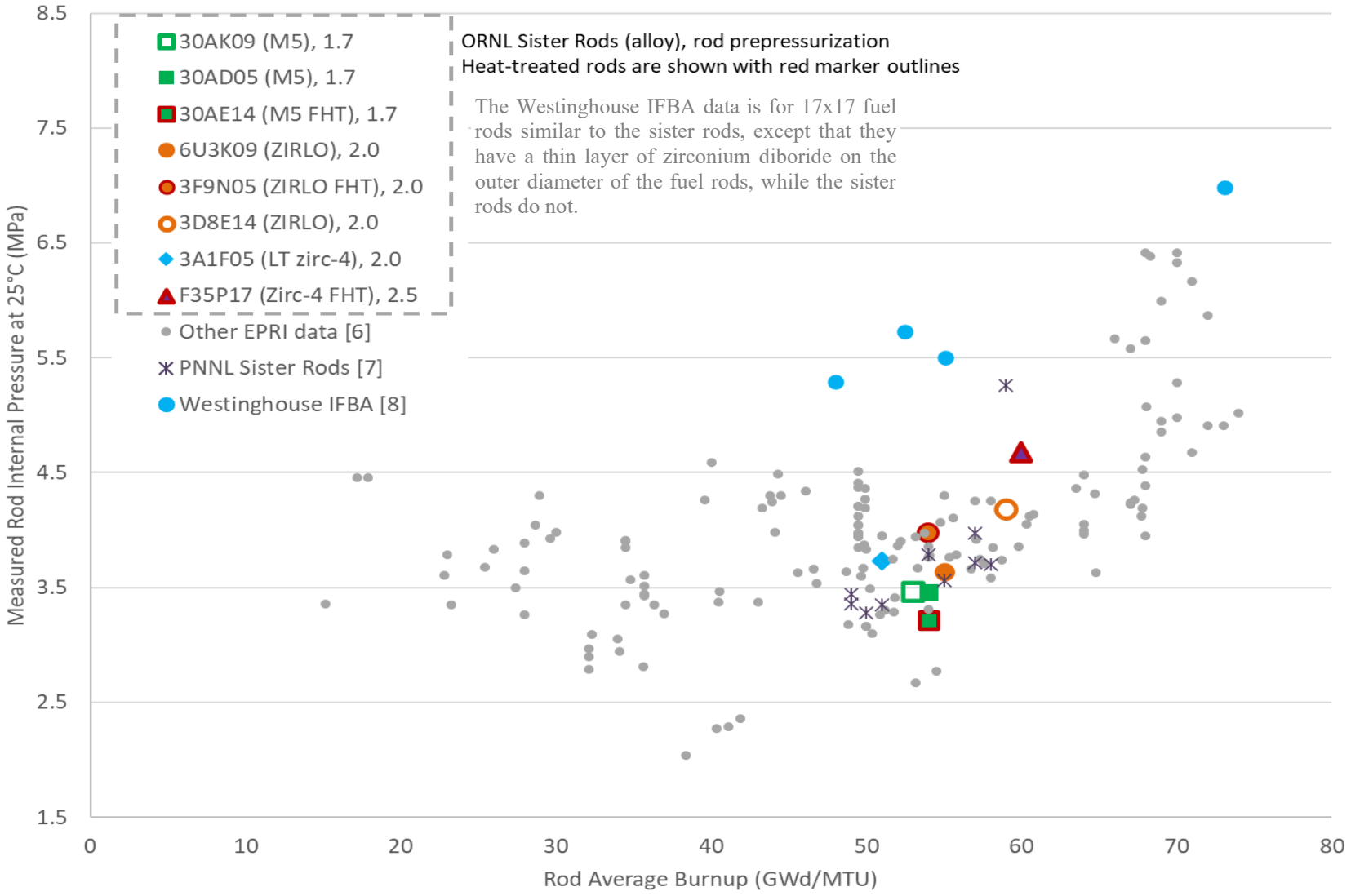

Figure 9. Sister rod measured rod internal pressure at 25°C.

7.1 Effect of FHT on Rod Internal Pressure and Void Volume

Comparisons of the measured rod internal pressure and void volume can provide some information about the effects, if any, of the heat treatments performed on three of the sister rods. For the ZIRLO-clad rods, the FHT rod has a higher void volume and a higher internal pressure than the corresponding baseline. Evaluating the measured pressure and void volume data independently of other data reported herein and considering the measurement uncertainty and expected variation in rod internal pressure and void volume related to operational differences, the difference between the baseline and FHT rod measurement results are not likely to be statistically different.

However, based on comparisons of the P_fV for all ZIRLO Phase 1 rods, there is evidence that the FHT 3F9N05 sister rod is different from the baseline rods, and there could have been an effect on either void volume or fission gas partial pressure related to the FHT.

When the same information is evaluated for the Phase 1 M5-clad sister rods, no effects related to FHT are evident. The M5 FHT rod had a higher void volume and lower pressure than the M5 baseline rods, but they are nearly within measurement uncertainty of each other.

To determine whether the heat treatment of the Zirc-4-clad rod made a difference in the rod internal pressure and void volume, it is preferable to compare the results with the baseline Zirc-4 rod measured by PNNL. The void volume measured by PNNL on the baseline Zirc-4 rod is ~0.7 cc lower than that measured by ORNL on the FHT rod, which is almost within the ORNL 2σ volume measurement uncertainty of 0.5 cc. The rod internal pressure measured by PNNL for the baseline Zirc-4 rod is ~12% higher than that measured by ORNL for the FHT rod. PNNL's measurements of that rod were obtained from the bottom of the fuel rod in the pellet stack. Other than the PNNL Zirc-4-clad rod, the closest comparable baseline sister rod is a LT Zirc-4-clad rod. The void volumes of the FHT Zirc-4 rod and the baseline LT Zirc-4 rod are within measurement uncertainty of each other, but the FHT Zirc-4 rod pressure is significantly higher than the baseline LT Zirc-4 rod. The pre-pressure of the Zirc-4 rod was 0.5 MPa higher than the LT Zirc-4, but this does not account for the almost 1 MPa difference observed in the rods' end-of-life rod internal pressures. Although the Zirc-4 and LT Zirc-4 rods are very similar, differences in the rods' mechanical designs could result in different end-of-life pressures and void volumes. Also, as mentioned previously, the Zirc-4 rod was a lead test rod operated to HBU over four cycles, whereas the LT Zirc-4 rod was part of a typical batch fuel assembly operated over two cycles. Given these differences and based only on a comparison of the rod internal pressure and void volume data, it is unclear whether there was an effect related to the heat treatments on the Zirc-4-clad rod.

7.2 Comparisons with Code Predictions

As listed in Table 5, blind predictions of the sister rod internal pressure and void volume were made by Geelhood [9] using the FAST code and by Stimpson [10] using BISON. The two codes represent two different approaches in fuel rod modeling with FAST providing models that are highly calibrated to a large body of empirical data and BISON operating through a more general first principles approach. This section compares the two predictions with the measured data.

BISON generally overpredicted pressure, whereas FAST underpredicted it. FAST pressure predictions for the ZIRLO-clad 6U3 rods were within ±5% of measured pressure, but other ZIRLO-clad rods from assembly 3F9 and 3D8 were within -25% of measured pressure. FAST underpredicted all the M5-clad rods with differences between -13 and -28%. The LT Zirc-4 rod pressure was also underpredicted (-18%), and FAST underpredicted the Zirc-4 rods (-15 and -25%). The average difference between the FAST pressure prediction and the measured value is -14%. Although the FAST code appeared to produce more accurate pressure predictions for ZIRLO-clad sister rods, the BISON predictions did not appear to have a trend

related to the cladding alloy. The BISON pressure prediction difference from measured ranged from +10 to +81% with an average difference of +40%. Five BISON rod simulations did not converge [10].

BISON underpredicted rod void volume, whereas FAST overpredicted it most of the time. As with pressure, the FAST void volume predictions for ZIRLO-clad rods from assembly 6U3 were more accurate than the predictions for other sister rods with the average difference ranging from 0 to +14%. Other than the trend noted for the 6U3 rods, there did not appear to be a cladding alloy-related trend within the FAST void volume predictions. The average difference from measured void volume for the FAST predictions was +20%. The BISON void volume prediction average difference from measured was -37%. The BISON void volume trends appeared relatively insensitive, producing nearly the same void volume for all rods.

The product of the rod internal pressure and void volume (PV) provides an additional metric to compare the measured rod data with the code predictions. When considering PV, the FAST prediction difference from measured ranged from -14 to +18%, with an average difference of 2%. For the BISON predictions, the difference from $P_m V_m$ ranged from +16% to -26% with an average difference of -11%.

When fission gas release is available for the sister rod measurements, it would be useful to compare it with the predicted fission gas release. Other operating data could be reviewed in a similar fashion to determine whether the improved modeling of a single parameter or a group of parameters can increase the accuracy of the internal pressure and void volume predictions.

Finally, to provide an additional viewpoint on whether the heat treatments applied to three of the sister rods resulted in a change of the rod internal pressure or void volume, the predictions were compared with ORNL's measurements. The variations from rod to rod that were measured are consistent with variations predicted by FAST. An additional FAST calculation was completed to simulate the applied sister rod heat treatments, and there was no change to the predicted fission gas release resulting from the short time at 400°C. There does not appear to be a consistent pattern when comparing the BISON results with the measured results, and the BISON simulations for 2 of the 3 heat-treated rods did not converge; the non-convergence is not related to the heat-treatment, which was not included in the BISON simulations.

Additional discussion and graphs comparing the predicted vs. measured results are provided in Appendix C.

Table 5. Comparison of measured and code-predicted rod internal pressure and void volume.

Rod ID	Cladding type	Average rod burnup (GWd/MTU)	Measured rod internal pressure (MPa)	Measured void volume (cc)	FAST predicted [9] rod internal pressure (MPa)	Fast predicted [9] void volume (cc)	BISON predicted [10] rod internal pressure (MPa)	BISON predicted [10] void volume (cc)
30AD05	M5	54	3.46	10.63	2.82	13.48	4.96	7.42
30AE14*	M5	54	3.22	10.99	2.82	13.50	5.06	7.44
30AK09	M5	53	3.46	9.89	2.82	13.26	4.50	7.34
30AP02 [7]	M5	49	3.36	10.8	2.80	12.85	3.69	7.40
5K7C05 [7]	M5	57	3.97	9.7	3.11	14.61	No result reported	No result reported
5K7K09 [7]	M5	54	3.79	10.5	2.72	13.96	5.82	7.55
5K7P02 [7]	M5	51	3.35	11.2	2.73	13.43	4.53	7.39
3D8E14	ZIRLO	59	4.18	11.73	3.19	15.28	7.56	7.51
3F9N05*	ZIRLO	54	3.98	12.74	3.46	14.76	No result reported	No result reported
3F9P02 [7]	ZIRLO	49	3.44	12.8	3.28	13.45	5.36	7.15
6U3K09	ZIRLO	55	3.64	11.78	3.47	13.41	4.56	7.10

Table 5. Comparison of measured and code-predicted rod internal pressure and void volume, continued.

Rod ID	Cladding type	Average rod burnup (GWd/MTU)	Measured rod internal pressure (MPa)	Measured void volume (cc)	FAST predicted [9] rod internal pressure (MPa)	Fast predicted [9] void volume (cc)	BISON predicted [10] rod internal pressure (MPa)	BISON predicted [10] void volume (cc)
6U3L08 [7]	ZIRLO	55	3.56	12.4	3.48	13.44	4.62	7.02
6U3M03 [7]	ZIRLO	57	3.72	11.9	3.53	13.57	4.95	6.97
6U3O05 [7]	ZIRLO	58	3.70	12.7	3.55	13.61	5.07	6.96
6U3P16 [7]	ZIRLO	50	3.28	13.1	3.37	13.16	4.29	7.40
3A1F05	LT Zirc-4	51	3.73	12.94	3.04	16.77	No result reported	No result reported
F35K13 [7]	Zirc-4	59	5.26	12.6	3.97	14.42	No result reported	No result reported
F35P17*	Zirc-4	60	4.68	13.32	3.99	14.55	No result reported	No result reported

* heat-treated as described in Section 3 prior to rod internal pressure and void volume measurement.

8. Pellet Stack Gas Depressurization, Gas Transmission, and Steam Transmission Testing

The typical design of pressurized water reactor (PWR) fuel rods includes a small gap between the pellet OD and the cladding ID and a plenum volume at the top of the fuel rod that provides void volume for the helium gas used to pre-pressurize the rods. In addition to the gap and plenum void volumes, the sister rods' pellets include chamfers and dishes, and those void volumes provide a relatively large reservoir throughout the pellet stack for pre-pressurization gas.

At beginning-of-life, these relatively large void volumes provide an open pathway for gas transmission up to the onset of pellet-cladding interaction (PCI). By the end of the first cycle, cladding creep-down and pellet swelling tend to close the gap between the pellet OD and the cladding ID, and after PCI, gas transmission is restricted because the gap is no longer open. The amount of PCI varies axially. Local fission gas production and its release to the rod void volume are variable along the axial length of the rod because power, fluence, and fuel temperature vary radially and axially within the fuel rod. However, as the rod is operated in the reactor, additional circulation paths through the pellet stack are developed, depending on local operating conditions. The process is somewhat stochastic and is related to thermal cycling of the fuel, crack development in the pellet due to thermal stresses, and crack self-healing. Once the fuel is discharged, the flow path within the pellet stack becomes essentially fixed. However, during interim storage and transportation the higher differential pressure between the rod internal pressure and the storage environment pressure may induce temporary or permanent cladding diameter increases that result in a larger rod void volume, offering additional circulation paths.

To characterize the ability for helium and fission gases to move through the pellet stack, gas depressurization and transmission tests were performed. Appendix C discusses the general setup of ORNL's gas transmission and depressurization tests, provides a more detailed discussion of the measurement procedures, derives the methods used to correlate the data, and presents the detailed results of the sister rod measurements. Additionally, to characterize the ability of steam to move through the stack (as would be the case for a rod breeched in reactor and subjected to vacuum drying conditions during preparations for dry storage), a steam transmission test was developed. Appendix C-8 discusses the system design and results obtained.

8.1 Results of the Gas Depressurization and Transmission Testing

The results of the testing are summarized in Table 6. For the gas transmission tests, two sister rods were tested at three different pressures, and the time vs. pressure recorded is shown in Figure 10. At the pressures used in the transmission tests, which are lower than the measured rod internal pressure, the time response of the system was ~30 min for one rod and ~3 h for the other. Both rods demonstrated a clear correlation of gas transmission time with the applied pressure. The pressure vs. time recorded for the depressurization tests is shown in Figure 11. Although some rods took longer than others to depressurize, none took longer than ~24 h to reach atmospheric pressure, demonstrating good communication along the pellet stack at room temperature (RT). All tests verified the ability of the argon gas used in the test to move through the pellet stack at RT and extrapolating the measured data to the as-measured rod internal pressure of the rods, all would be expected to fully depressurize within 30 minutes of a cladding breach.

The permeability of the pellet stack varied over less than one order of magnitude for this set of rods, which is modest and could indicate some common feature about HBU fuel. The average permeability for the HBU 17 × 17 PWR fuel rods is 4.25e-14 m^2 using the Muskat-Poiseuille model. 3A1F05 (LT Zirc-4) and F35P17 (heat-treated Zirc-4) have the largest permeability values. The variance in the measurements is likely due to the wide variety of claddings, pellets designs, and operating histories. A higher permeability value means the gas moves more easily through the pellet stack. The permeability maintains a relatively constant value

with pressure variation in the three rods on which the gas transmission test was repeated at varying starting pressures.

Evaluations of the data did not identify a close correlation of permeability with rod average burnup but did identify a direct correlation to the average assembly in-reactor fuel temperature and rod lifetime maximum in-reactor duty (see Appendix C, Figure C-23). The permeability is closely related to the rod manufacturer, indicating that the pellet manufacturing process and in-reactor operating temperature determine the permeability of the pellet stack. Furthermore, the permeability data strongly indicate that an offset in the permeability resulted from the heat treatment, likely related to a permanent increase in cladding diameter resulting from the increased rod internal pressure and lower cladding yield strength at FHT conditions. Unfortunately, post-heat-treatment rod diameter was not measured, and the cut segment diameters do not provide a good comparison point. Future FHT will include both pre- and post-FHT diameter measurements.

A natural extension of this work is to conduct the same tests at the fuel rod storage and transportation temperatures using a similar apparatus. Also, it would be prudent to measure gas transmissibility on rods that have been in dry storage for ~10 years to determine whether the flow paths have become restricted.

Table 6. Results of depressurization and transmission tests.

Rod	Cladding alloy	Heat-treatment	Applied pressure differential (MPa)	Muskat-Poiseuille permeability and regression model coefficient of determination	
				K (m^2)	R^2
3A1F05	LT Zirc-4	None	0.10	8.40E-14	0.999
			1.41	8.32E-14	0.999
			2.17	8.32E-14	1.000
			2.89	8.23E-14	1.000
			Average	*8.32E-14*	
F35P17	Zirc-4	FHT	0.10	9.96E-14	0.999
3F9N05	ZIRLO	FHT	0.10	7.30E-14	0.999
3D8E14	ZIRLO	None	0.10	4.08E-14	0.998
6U3K09	ZIRLO	None	0.10	1.99E-14	1.000
			1.55	1.62E-14	0.994
			2.82	2.05E-14	1.000
			Average	*1.89E-14*	
30AK09	M5	None	0.10	1.04E-14	0.999
			1.41	1.02E-14	0.999
			2.17	1.05E-14	1.000
			2.89	1.11E-14	1.000
			Average	*1.06E-14*	
30AD05	M5	None	0.10	1.15E-14	1.000
30AE14	M5	FHT	0.10	2.40E-14	1.000
			Average of all	***4.25E-14***	

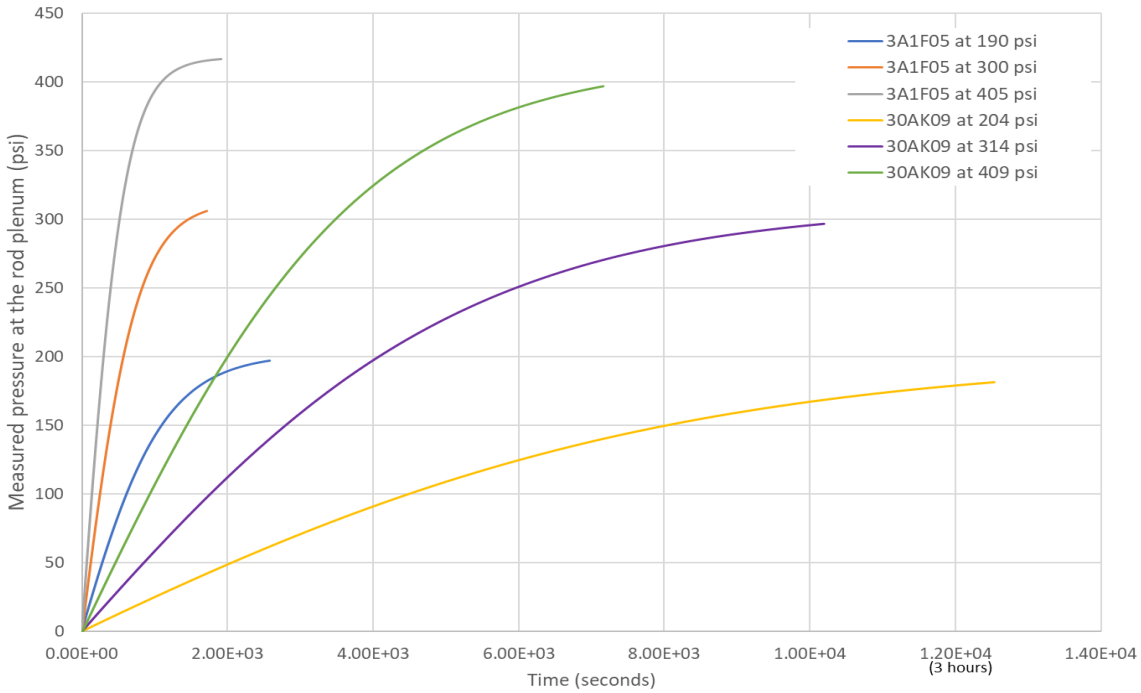

Figure 10. Results of gas transmission tests on two sister rods (three different pressures on each rod).

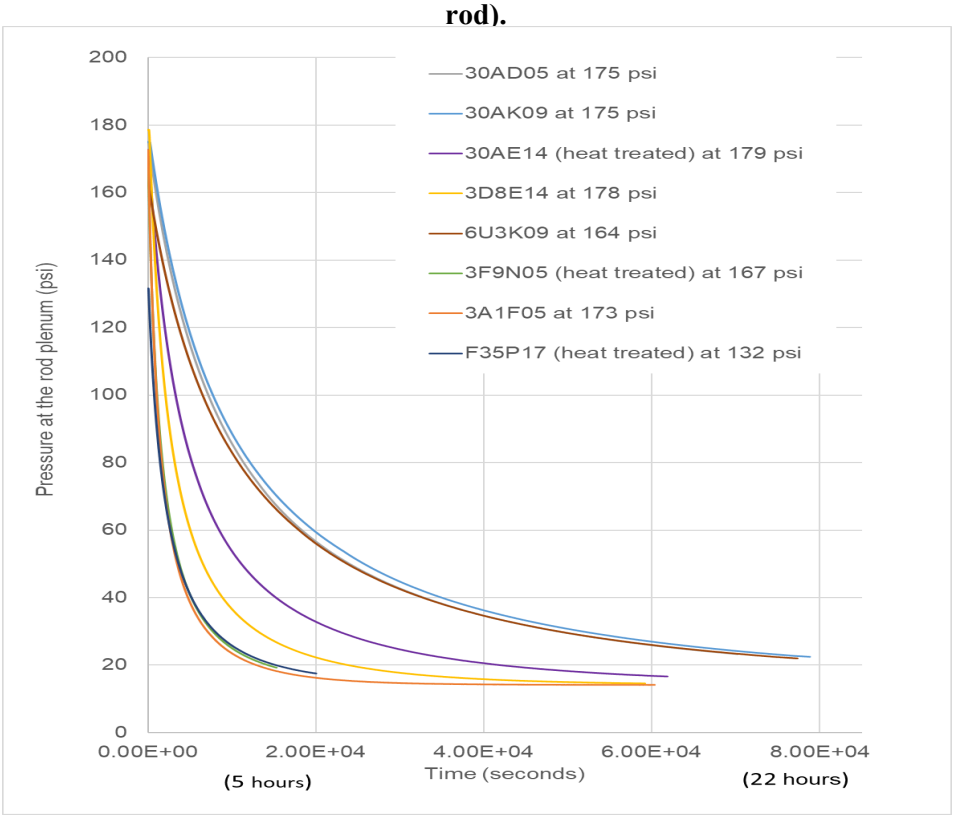

Figure 11. Results of the depressurization tests on eight sister rods (three rods were heat treated).

8.2 Results of Steam Transmission Testing

A steam transmission test was developed to examine the ability for water/steam to be removed during vacuum drying from a rod that was breached in-reactor. The initial concept of the test is described in Appendix C. While progress towards a successful test has been made and this section provides some qualitative information, this particular setup needs improvement to provide accurate results.

In developing the test method and fixturing, a total of 5 segments were tested for air, and 4 were tested for steam; these segments came from both high-burnup sister rods and moderately high-burnup MOX rods. The segments used were discards and the lengths of the segments reflect what was available for testing.

As a point of verification, the steam transmission setup was expected to be capable of reproducing the gas transmission results that were obtained on the full-length sister rods when scaled to the appropriate length (see Appendix C Section C-8.3 for the method used). Since burnup and pellet condition varies axially, the permeability also varies axially and an arbitrary segment from the rod is not representative of the whole rod permeability. Flow through the pellet stack can be limited by particular elevations where the flow path is more restricted (e.g., fewer cracks in the pellets or significant PCI is present). It is possible that the difference is a factor of 2 from elevation to elevation, but the full rod test (see Section 8.1) should encompass any restricted flow paths and a segment test shouldn't be significantly lower than the whole.

As listed in Table 7, the verification tests yielded permeabilities that were about half the full-length rod permeability. One sister rod segment had no flow after more than 20 hours of air testing. Posttest, it was discovered that it may be possible to overtighten the seal nut between the rod segment and steam source, inadvertently restricting flow to the rod segment. If there is a sensitivity to the fixture tightness, this can be easily eliminated by defueling 10 mm at the ends of the segments. Additional work is needed to fully understand the source of the differences in permeability. Despite the low air permeability values obtained, the test was continued to the steam transmission test.

Table 7. Results of the RT Air Verification Tests Completed Prior to Steam Testing.

Segment	Segment length (m)	Fit permeability (m^2)	Full length rod permeability (m^2)	Comment
30AD05-2519-2630	0.111	5.34e-15	1.15e-14	Permeability ratio of 0.46, segment near rod mid region
MX3B14-3235-3405*	0.170	8.30e-14	1.66e-13	Permeability ratio of 0.50, segment near rod plenum region
MX3B14-0799-0969*	0.170	1.14e-13	1.66e-13	Permeability ratio of 0.69, segment near rod lower region
3D8E14-1656-1804	0.148	2.92e-14	4.08e-14	Permeability ratio of 0.72, segment near rod mid region
30AE14-1696-1800	0.104	N/A	2.40e-14	No transmission observed in >20 hours; segment was not used for steam tests

* These were discarded segments from another group of 17x17 spent fuel rods and are not a part of the Sister Rods project.

Although the quantitative values obtained using this particular test setup and protocol may be flawed, they do provide a qualitative comparison point for steam transmission vs. gas transmission. Tens of hours were required to transmit steam through the pellet stack for the short segments tested. Overall, transmission of steam/water through the rod segments was observed, but the rate appears to be much slower than that for

the single-phase gases, and the behavior of the system was quite different than expected. An example of the data collected is provided in Figure 12 for 3D8E14-1656-1804, which was tested at a system temperature of 160ºC. To determine whether the behavior existed at other temperatures/pressures, a second run was conducted for segment MX3B14-3235-3405 at a system temperature of 115°C. Similar behavior was observed, and the estimated model permeabilities differed by a factor of approximately 5.

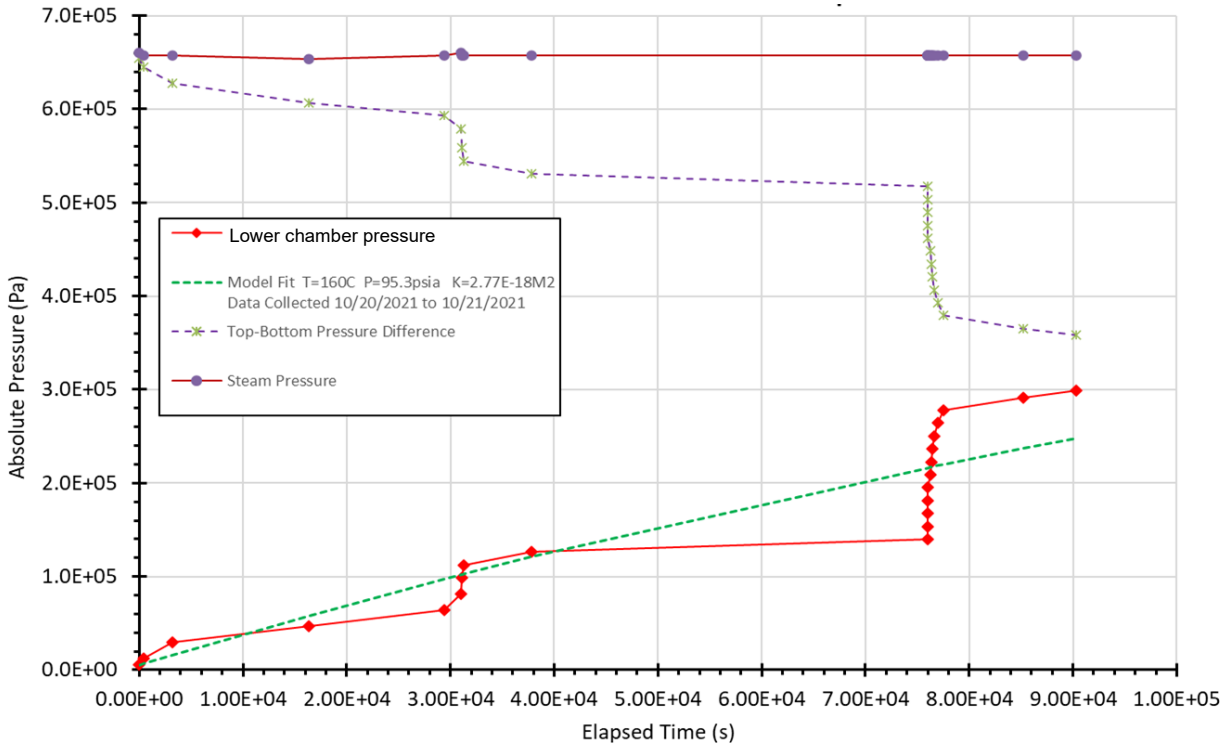

Figure 12. 30AD05-2519-2630 steam test showing step-like behavior and the bisecting model fit.

There were rapid fluctuations in many cases rather than a slow, asymptotic change, which made interpretation of the data difficult. Clearly something unusual is happening during these tests. Possible causes include boiling instabilities, two-phase flows, relocation of pellet fragments, chemical reactions, delays in vaporization leading to falling water droplets, and boiling point suppression from dissolved fission products. Given the observations, the model that best fits the data seems to be one that assumes that the steam was in a liquid phase during transport through the pellet stack. The cracks and pores in the fuel stack through which the steam must pass are assumed to impose flow/pressure conditions that allow the existence of mostly liquid water. Therefore, a simple 1D model assuming liquid Darcy flow in the fuel segment that flashes into steam as it exits was used as a starting point to evaluate the data and is described in Appendix C. This model could include boiling instabilities if developed to a higher degree. As is, it is only a rough approximation, but it provides a starting point.

Although it is not clear that the evaluated permeabilities derived for the steam transmission tests are correct due to the possibility of the choked inlet, given the simple model results shown in Table 8 one can state that steam gas transmission is grossly hindered as compared with dry gases, as demonstrated by the low apparent permeability measured.

Table 8. Summary of Steam Permeabilities

Segment	Fit permeability (m^2)	Test Temperature (°C)
30AD05-2519-2630	2.77E-18	160
MX3B14-3235-3405*	1.50E-16	160
MX3B14-3235-3405*	2.78E-17	115
MX3B14-0799-0969*	3.25E-16	160
3D8E14-1656-1804	4.59E-17	160

* These were discarded segments from another group of 17x17 spent fuel rods and are not a part of the Sister Rods project.

The condensed steam in the lower chamber at the conclusion of the first steam test (sample 30AD05-2519-2630) was collected and analyzed using inductively coupled plasma mass spectrometry (ICP-MS). The objective was twofold: (1) to obtain the source term of instant release fractions from steam dissolution of a fuel rod sample, and (2) to estimate the presence of particulate fines that could aerosolize during vacuum drying of failed fuel. Two separate samples were evaluated: (1) the liquid water with any dissolved isotopes (the *dissolved* sample) and (2) solid fines that were pulled from the rod segment by the steam (the *digested* sample). The digested sample includes the fines present in the sample container and the (> 0.45 μm) particulates gathered by filtration from a post-test rinse of the steam test exit chamber. The digested material is thought to be carried by the steam/water during the transmission process and was either insoluble or large enough that it did not fully dissolve into the steam/water under the test timescales. The experiment lasted for approximately 24 hours, but the solids were extracted from the water approximately 1 year after the test was completed (sample collected 10/22/2021; sample analyzed 08/25/2022). It is also speculated that some of the collected solid material could also have come from the sample's cladding ID.

Analysis of the solid particles (digested sample set) yielded several isotopes, including actinides and fission products. There was more solid SNF material entrained within the steam flow than was dissolved in the steam. The concentration of ^{139}I, ^{127}I, ^{88}Sr, $^{133/137}Cs$, and ^{97}Mo in the dissolved sample was higher than the concentration of the isotopes available within the stack of pellets tested, meaning that these isotopes are readily released. In comparison with static leaching experiments at RT (see Section 14 of this document and Appendix J), the amounts of cesium and iodine released were higher.

The entrained solids and dissolved SNF mass released in the steam during vacuum drying can be deposited on other surfaces inside a spent fuel canister and potentially be aerosolized if the canister is opened or breached. Based on the findings, three factors must be considered during vacuum drying: (1) effectiveness of vacuum drying at removing the water in the rod through the cladding defect, (2) amount of dose in the form of dissolved/leached fuel particles and gaseous fission products released with the water, and (3) particle size distribution of the leached material and whether it falls in the respirable range.

9. Fission Gas Sample Isotopic Composition and Calculated Fission Gas Release

A fission gas sample was taken from each punctured sister rod. Gaseous fission products evolve in all UO_2 nuclear fuel pellets at all axial elevations during reactor operation. They are located near the site of the fission, within the fuel grains, at a grain boundary, or at free surfaces on the pellet. The gaseous fission products form small bubbles within the pellet since the xenon and krypton gases produced are virtually insoluble in UO_2. Although much of the fission gas remains trapped within the fuel pellet microstructure as porosity, some fraction of the fission gas is released to the interior void volume of the fuel rod and contributes to an increase in the fuel rod internal pressure.

According to the Electric Power Research Institute, less than 5% of the fission gas produced in the pellet stack during normal operation is released to the rod void volume [6]. The quantity of fission gas released from the pellet to the rod void volume during reactor operation has been the topic of much study because the gross rod pressure and localized rod pressure are important to rod performance during reactor transients, such as loss-of-coolant accidents and reactivity-initiated accidents. The percentage of fission gas released is calculated as the moles of fission gas in the rod void volume divided by the total calculated fission gas produced during operation.

The eight sister rod fission gas samples were analyzed by the ORNL Nuclear Analytical Chemistry and Isotopic Laboratories group, and the details of the analysis are provided in Appendix D. Measured gas concentrations for the eight sister rod gas samples collected are provided in Table 9. Six of the sister rod samples were measured up to three times on nonconsecutive days, and the determined fission gas concentrations were averaged for those samples. The concentrations measured were determined by linear regression monitoring ^{84}Kr and ^{132}Xe, which are naturally occurring isotopes present at 56.99 and 26.91 atom%, respectively. The isotopic concentration in the sister rod samples was determined by measuring the current responses corresponding to the ^{84}Kr and ^{132}Xe isotopes and comparing those with the current response of the known concentration calibration standards. The total uncertainty values reported are the combined uncertainties of the duplicate measurements at a 95% level of confidence. The number of digits in the reported mole% and their uncertainties are provided for information and are not intended to convey a significant degree of reliability.

Based on inspection of Table 9, there is generally good agreement between the M5 rods and the LT Zirc-4 and Zirc-4 clad rods. However, per the data in Table 9, one ZIRLO rod (6U3K09) appears to have about half the fission gas content (krypton and xenon) compared with two other ZIRLO rods that were measured at ORNL. When the PNNL sister rod data [7] are included in the dataset, as illustrated in Figure 13, 6U3K09 is clearly consistent with the remainder of the dataset, whereas the other two ORNL-measured ZIRLO rods are too high with the deviation not explained by measurement uncertainty. When all the data are plotted as a function of the independently measured fission gas partial pressure, the data are consistent, as shown in Figure 14, except for one Zirc-4 rod (F35K13), which is ~1.4 MPa above other sister rods. Based on Figure 14, the differences in the measured rod fission gas composition of the two ZIRLO-clad rods appear to be simply a consequence of higher fission gas release for those rods. Although not shown here, when xenon is graphed, the same trends are observed. Regardless of cladding alloy, all sister rods have a different operational duty. The source of higher fission gas release will be investigated once more detailed information on the measured rod burnup and predicted rod fission gas production are available.

The isotopic data reported in Table 10 and Table 11 include natural and fission product krypton and xenon isotopes.

Table 9. Sister rod gas sample measured elemental composition, mole%*.

	Sample ID											
Detected gas**	30AK09 (M5) SR-Gr-02			30AD05 (M5) SR-Gr-05			30AE14 (M5, heat treated) SR-Gr-06			3A1F05 (LT Zirc-4) SR-Gr-04		
Krypton	1.60	±	0.15	1.41	±	0.19	1.45	±	0.22	1.97	±	0.25
Xenon	15.31	±	1.33	14.10	±	0.70	14.11	±	1.49	18.46	±	1.72
Helium***	83.09	±	1.10	84.49	±	0.59	84.44	±	1.62	79.57	±	1.83
	Sample ID											
Detected gas**	6U3K09 (ZIRLO) SR-Gr-01			3D8E14 (ZIRLO) SR-Gr-03			3F9N05 (ZIRLO, heat treated) SR-Gr-07			F35P17 (Zirc-4, heat treated) SR-Gr-08		
Krypton	1.11	±	0.10	2.36	±	0.30	2.23	±	0.30	1.93	±	0.25
Xenon	10.45	±	1.47	22.44	±	1.41	20.08	±	2.01	19.87	±	1.99
Helium***	88.44	±	1.41	75.20	±	1.41	77.69	±	1.62	78.20	±	1.62

* Reported uncertainties are the total combined uncertainties at the 95% level of confidence. Two decimal places are provided in the reported values for information only and are not intended to imply a significant degree of reliability. The precision contribution for samples 01–06 was the standard deviation of the values measured in August 2018 and September 2018. Because only a single dataset was measured for samples 07 and 08, for conservatism, the precision contribution to the total uncertainty for those data was taken as the worst-case scenario observed for samples 01–06.

** Some residual air present in the sampling system were detected, and the resulting oxygen and nitrogen content was neglected when determining the fission gas component percentages and FGR in the fuel rod (Table 12).

*** The measured helium includes the pre-pressurization helium and any helium produced as fission/decay products.

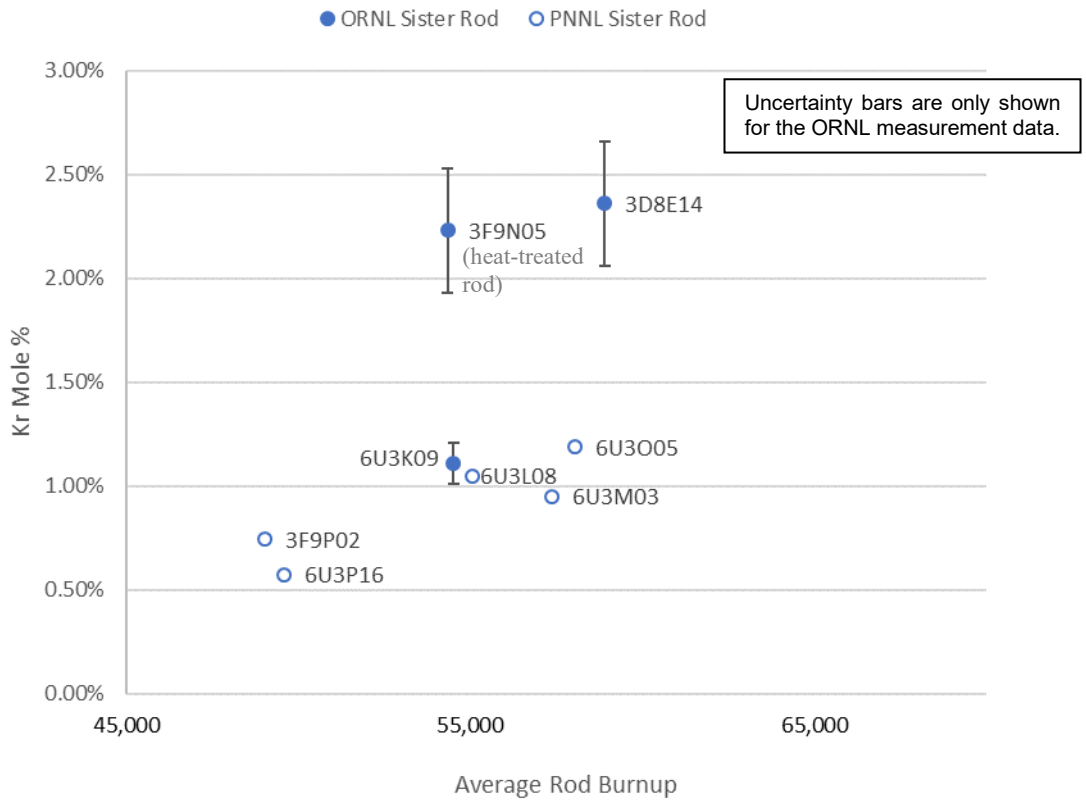

Figure 13. The measured krypton content of the rod fission gas for ZIRLO-clad sister rods.

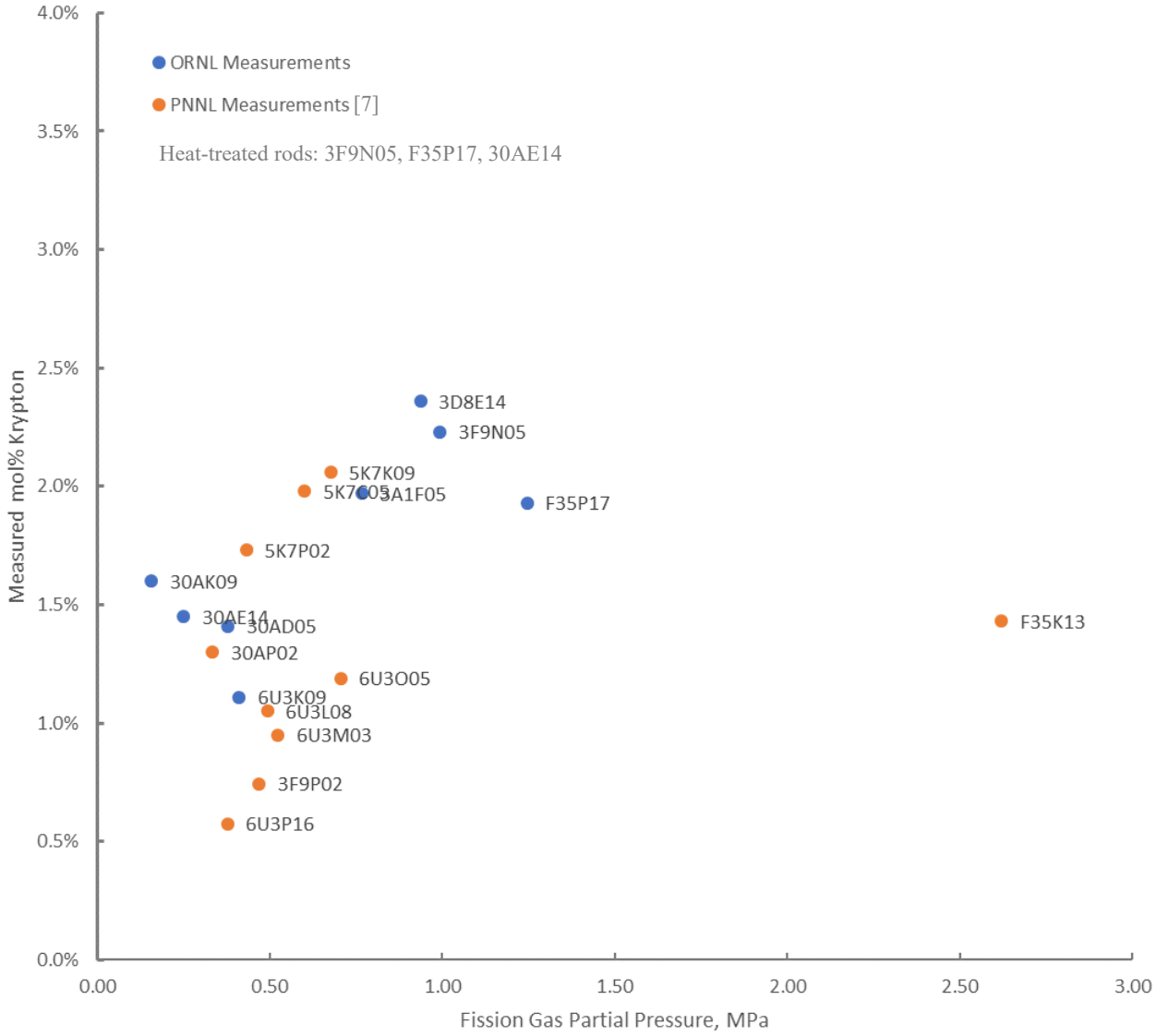

Figure 14. Measured krypton content of the rod fission gas as a function of the independently measured fission gas partial pressure.

Table 10. Fission gas isotope ratios, atom% ratio.

Sample	30AK09 (M5)			30AD05 (M5)			30AE14 (M5, heat treated)			3A1F05 (LT Zirc-4)		
Isotope ratio	SP-Gr-02*			SP-Gr-05*			SP-Gr-06*			SP-Gr-04*		
$^{82}Kr/^{84}Kr$	0.021	+/-	0.009	0.018	+/-	0.007	0.019	+/-	0.008	0.023	+/-	0.003
$^{83}Kr/^{84}Kr$	0.322	+/-	0.009	0.307	+/-	0.008	0.318	+/-	0.010	0.310	+/-	0.002
$^{85}Kr/^{84}Kr$***	0.121	+/-	0.007	0.121	+/-	0.008	0.123	+/-	0.009	0.059	+/-	0.003
$^{86}Kr/^{84}Kr$	1.533	+/-	0.014	1.525	+/-	0.009	1.535	+/-	0.011	1.512	+/-	0.000
$^{128}Xe/^{132}Xe$	0.005	+/-	0.003	0.005	+/-	0.003	0.006	+/-	0.003	0.007	+/-	0.004
$^{130}Xe/^{132}Xe$	0.012	+/-	0.002	0.012	+/-	0.002	0.013	+/-	0.001	0.015	+/-	0.001
$^{131}Xe/^{132}Xe$	0.278	+/-	0.004	0.289	+/-	0.003	0.296	+/-	0.002	0.293	+/-	0.004
$^{134}Xe/^{132}Xe$	1.178	+/-	0.006	1.173	+/-	0.022	1.178	+/-	0.011	1.165	+/-	0.033
$^{136}Xe/^{132}Xe$	1.689	+/-	0.029	1.661	+/-	0.055	1.654	+/-	0.029	1.647	+/-	0.080
Sample	**6U3K09 (ZIRLO)**			**3D8E14 (ZIRLO)**			**3F9N05 (ZIRLO, heat treated)**			**F35P17 (Zirc-4, heat treated)**		
Isotope ratio	**SP-Gr-01***			**SP-Gr-03***			**SP-Gr-07****			**SP-Gr-08****		
$^{82}Kr/^{84}Kr$	0.016	+/-	0.005	0.022	+/-	0.004	0.033	+/-	0.010	0.034	+/-	0.011
$^{83}Kr/^{84}Kr$	0.311	+/-	0.005	0.277	+/-	0.001	0.310	+/-	0.006	0.278	+/-	0.005
$^{85}Kr/^{84}Kr$***	0.100	+/-	0.004	0.073	+/-	0.004	0.088	+/-	0.005	0.050	+/-	0.003
$^{86}Kr/^{84}Kr$	1.537	+/-	0.008	1.474	+/-	0.007	1.530	+/-	0.008	1.469	+/-	0.008
$^{128}Xe/^{132}Xe$	0.005	+/-	0.003	0.007	+/-	0.004	0.011	+/-	0.006	0.011	+/-	0.006
$^{130}Xe/^{132}Xe$	0.012	+/-	0.002	0.015	+/-	0.002	0.019	+/-	0.002	0.018	+/-	0.002
$^{131}Xe/^{132}Xe$	0.278	+/-	0.004	0.254	+/-	0.005	0.290	+/-	0.004	0.249	+/-	0.003
$^{134}Xe/^{132}Xe$	1.178	+/-	0.006	1.126	+/-	0.033	1.156	+/-	0.018	1.094	+/-	0.017
$^{136}Xe/^{132}Xe$	1.689	+/-	0.029	1.582	+/-	0.083	1.600	+/-	0.048	1.545	+/-	0.046

* Uncertainty for samples defined as a 1σ external standard deviation of the replicate analyses (for 01, 03, and 04, $n = 2$; for 02, 05, and 06, $n = 4$).

** For SP-Gr-07 and 08, only one replicate was performed; the assigned uncertainties are the averages of the other six samples.

*** ^{85}Kr was decay-corrected to February 2019 in each case.

Table 11. Fission gas isotopic composition, atom %*.

Sample	30AK09 (M5)	30AD05 (M5)	30AE14 (M5, heat treated)	3A1F05 (LT Zirc-4)
Isotope	SP-Gr-02*	SP-Gr-05*	SP-Gr-06*	SP-Gr-04*
^{82}Kr	0.69 ± 0.34	0.59 ± 0.30	0.64 ± 0.32	0.81 ± 0.40
^{83}Kr	10.73 ± 0.32	10.34 ± 0.31	10.62 ± 0.32	10.67 ± 0.32
^{84}Kr	33.37 ± 0.67	33.65 ± 0.67	33.39 ± 0.67	34.43 ± 0.69
^{85}Kr ****	4.04 ± 0.20	4.08 ± 0.20	4.12 ± 0.21	2.03 ± 0.10
^{86}Kr	51.17 ± 0.51	51.33 ± 0.51	51.24 ± 0.51	52.06 ± 0.52
^{128}Xe	0.14 ± 0.07	0.13 ± 0.07	0.17 ± 0.09	0.16 ± 0.08
^{129}Xe	< 0.05	< 0.05	< 0.05	< 0.05
^{130}Xe	0.31 ± 0.16	0.30 ± 0.15	0.39 ± 0.19	0.36 ± 0.18
^{131}Xe	7.09 ± 0.35	6.98 ± 0.35	6.38 ± 0.32	7.11 ± 0.36
^{132}Xe	23.97 ± 0.48	24.16 ± 0.48	25.14 ± 0.50	24.24 ± 0.48
^{134}Xe	28.39 ± 0.57	28.33 ± 0.57	28.30 ± 0.57	28.23 ± 0.56
^{136}Xe	40.15 ± 0.40	40.10 ± 0.40	39.74 ± 0.40	39.90 ± 0.40
Sample	**6U3K09 (ZIRLO)**	**3D8E14 (ZIRLO)**	**3F9N05 (ZIRLO, heat treated)**	**F35P17 (Zirc-4, heat treated)**
Isotope	**SP-Gr-01***	**SP-Gr-03***	**SP-Gr-07****	**SP-Gr-08****
^{82}Kr	0.56 ± 0.28	0.77 ± 0.39	1.10 ± 0.55	1.20 ± 0.60
^{83}Kr	10.49 ± 0.31	9.75 ± 0.29	10.45 ± 0.31	9.83 ± 0.29
^{84}Kr	33.74 ± 0.67	35.14 ± 0.70	33.74 ± 0.67	35.30 ± 0.71
^{85}Kr ****	3.36 ± 0.17	2.56 ± 0.13	3.06 ± 0.15	1.81 ± 0.09
^{86}Kr	51.85 ± 0.52	51.78 ± 0.52	51.63 ± 0.52	51.86 ± 0.52
^{128}Xe	0.12 ± 0.06	0.17 ± 0.09	0.27 ± 0.20	0.28 ± 0.21
^{129}Xe	< 0.05	< 0.05	< 0.05	< 0.05
^{130}Xe	0.29 ± 0.15	0.39 ± 0.19	0.46 ± 0.23	0.45 ± 0.23
^{131}Xe	6.68 ± 0.33	6.38 ± 0.32	7.12 ± 0.36	6.36 ± 0.32
^{132}Xe	24.03 ± 0.48	25.14 ± 0.50	24.54 ± 0.49	25.54 ± 0.51
^{134}Xe	28.31 ± 0.57	28.30 ± 0.57	28.36 ± 0.57	27.92 ± 0.56
^{136}Xe	40.57 ± 0.41	39.74 ± 0.40	39.25 ± 0.39	39.44 ± 0.39

* Reported numerical uncertainties are the 2σ external standard deviation of all duplicate analyses. The last digit in the measurements and uncertainties is provided for information and is not intended to convey a significant degree of reliability. The accuracy of the analysis was confirmed using a National Institute of Standards and Technology traceable standard, and a bias correction did not measurably alter the data within the uncertainty of the 2σ standard deviation.

** SR-Gr-02, 05, and 06 also incorporate the uncertainty between two different modes of mass analysis, namely scanning electron microscopy (SEM) and Faraday.

*** For SR-Gr-07 and 08, only one replicate was analyzed; for conservatism, the uncertainty attributed to those data was taken as the worst-case scenario observed for samples 01–06.

**** ^{85}Kr was decay-corrected to February 2019 in each case.

Table 12 provides the measured xenon-to-krypton ratio for the sister rod samples. The ratios are within the expected range. The xenon-to-krypton ratio was also evaluated to determine whether there was any additional xenon or krypton preferentially released as a result of the FHT performed on three of the sister rods. Based on the data available, if additional fission gas is released as result of the heat treatment, then it does not significantly affect the proportion of xenon to krypton released.

The percentage of fission gas released (FGR) from the pellets to the void volume of the rod ranged from 1.6 to 3.6% and is included in Table 4.

Table 12. Measured xenon-to-krypton ratio for the sister rods.

Rod ID/condition	Cladding type	Measured xenon to krypton
30AK09/baseline	M5	9.6
30AD05/baseline	M5	10.0
30AE14/heat treated	M5	9.7
6U3K09/baseline	ZIRLO	9.4
3D8E14/baseline	ZIRLO	9.5
3F9N05/heat treated	ZIRLO	9.0
3A1F05/baseline	LT Zirc-4	9.4
F35P17/heat treated	Zirc-4	10.3

10. Fuel Burnup Measurements

Three specimens were sent to the ORNL Radiochemical Engineering Development Center for chemical determination of burnup (Nd, U, Pu only). Sixteen other specimens are being analyzed in more detail (~51 isotopes measured). The specimens cover the range of the Phase 1 sister rods that are being mechanically tested and will verify the code-predicted rod burnups and validity of the linear scaling of gamma scan profiles. Appendix D provides the details of the testing protocols.

Burnup measurement results are available for twelve samples. The results are provided in terms of g/gU in Table 13 and in GWd/MTU in Table 14 for the three burnup only specimens. The burnup results for the other nine specimens processed to date are listed in Table 15. More detailed information can be found in Appendix D of this report and as described by Canann et al. in their report to the Nuclear Regulatory Commission [35].

Table 13. Chemical isotopic analysis (burnup only) of sister rod specimens.

Project ID	**3D8E14-700-719**		**3D8E14-3206-3225***		**6U3K09-3506-3525**	
Specimen weight (g)	6.648		4.532		6.707	
Units	**g/gIHM**	**Uncertainty**	**g/gU**	**Uncertainty**	**g/gIHM**	**Uncertainty**
Nd (isotopics over six runs)	7.526E-03	3.919E-05	7.724E-03	3.987E-05	5.237E-03	2.755E-05
^{124}Nd wt %	0.8687%	0.0080%	0.7634%	0.0034%	0.4903%	0.0039%
^{143}Nd wt %	15.1330%	0.0017%	16.3629%	0.0011%	20.1298%	0.0016%
^{144}Nd wt %	36.4023%	0.0034%	35.2676%	0.0019%	32.3057%	0.0021%
^{145}Nd wt %	14.9920%	0.0016%	15.2970%	0.0010%	16.5945%	0.0014%
^{146}Nd wt %	18.7087%	0.0025%	18.4323%	0.0014%	17.1489%	0.0016%
^{148}Nd wt %	9.2956%	0.0019%	9.3012%	0.0016%	9.0248%	0.0016%
^{150}Nd wt %	4.5996%	0.0017%	4.5756%	0.0016%	4.3059%	0.0015%
Units	**g/gIHM**	**Uncertainty**	**g/gSoln**	**Uncertainty**	**g/gIHM**	**Uncertainty**
U	9.150E-01	3.235E-03	3.424E-03	0.342E-05	9.418E-01	1.561E-03
^{233}U wt %	0.0010%	NA	0.0010%	NA	0.0010%	NA
^{234}U wt %	0.0248%	0.0002%	0.0254%	0.0002%	0.0272%	0.0003%
^{235}U wt %	0.4368%	0.0005%	0.5822%	0.0007%	1.3359%	0.0016%
^{236}U wt %	0.6425%	0.0066%	0.6370%	0.0066%	0.5944%	0.0061%
^{238}U wt %	98.8958%	0.0066%	98.7554%	0.0066%	98.0425%	0.0063%
Units	**g/gU**	**Uncertainty**	**g/gU**	**Uncertainty**	**g/gU**	**Uncertainty**
Pu (isotopics over six runs)	1.119E-02	1.976E-04	1.276E-02	4.890E-04	1.028E-02	7.288E-05
^{238}Pu wt %	3.4261%	0.0598%	3.6434%	0.2286%	2.1232%	0.0597%
^{239}Pu wt %	50.9118%	0.1726%	51.7021%	0.9671%	59.1770%	0.4432%
^{240}Pu wt %	27.8080%	0.1372%	27.3843%	0.8421%	24.6114%	0.4178%
^{241}Pu wt %	6.3293%	0.1139%	6.5196%	0.2642%	8.3739%	0.1013%
^{242}Pu wt %	11.5248%	0.1091%	10.7505%	0.3482%	5.7145%	0.0265%

* During the dissolution of sample 3D8E14-3206-3225, there was a loss of sample while filtering the final digested solution in the hot cell to remove undigested solids. At the time of loss, the solution was homogeneous; therefore, the ratio of ^{148}Nd burnup indicator to uranium and plutonium was not compromised. Therefore, for this sample, burnup was calculated using total atom ratios in the final solution vs. the pellet as-is convention. Performing the calculation in this manner does not affect the results, and the final results are considered accurate.

Table 14. Measured Burnup for Sister Rod Burnup Only Specimens.

Project ID	**3D8E14-700-719**	**3D8E14-3206-3225**	**6U3K09-3506-3525**
Lab ID	**TAL SR-719**	**TAL SR-3225**	**TAL SR-3525**
Measured FIMA (%)	6.651	6.239	4.473
Measured burnup (GWd/MTU)	63.849	59.895	42.940
Measured burnup uncertainty, 1σ (%)	0.9	0.8	0.7
Operator-estimated burnup (GWd/MTU)	63.564	56.779	40.658
Measured/operator burnup ratio	1.004	1.055	1.056

Table 15. Measured Burnup for Sister Rod Extended Isotopic Specimens.

Sample ID	^{148}Nd		FIMA%	Burnup
	g/gU	2σ (%)		(GWd/MTU)
3D8E14-1375-1450	7.85E-04	0.24	6.81	65.4
F35P17-2383-2402	8.08E-04	0.25	7.00	67.2
30AE14-2675-2694	7.04E-04	0.24	6.15	59.1
3D8E14-0775-0796	7.77E-04	0.24	6.75	64.8
F35P17-3050-3069	7.88E-04	0.25	6.84	65.6
3F9N05-3593-3615	3.99E-04	0.35	3.59	34.5
3A1F05-0150-0165	4.51E-04	0.27	4.04	38.8
30AD05-0200-0215	5.50E-04	0.27	4.88	46.9
3A1F05-0225-0240	5.23E-04	0.27	4.66	44.7

11. Fatigue Testing

SNF assemblies must be shipped to other sites for processing and disposal. During shipment, the fuel is typically oriented horizontally, and the fuel rods are subject to periodic alternating loads related to the movement of the vehicle that result in the alternating bending of the SNF fuel rods. The number of bending cycles is related to the length of the shipping route with longer routes producing more cycles. Since it is well-known that cyclic loads can produce failures even when the stress and strain imposed are below the yield point of the material, it is prudent to investigate the SNF fatigue behavior.

Wang et al. [12, 13] developed a method for SNF fatigue testing segments called the *Cyclic Integrated Reversible-Bending Fatigue Tester* (CIRFT). CIRFT (DE.05) has been used to test several sister rod specimens. Appendix F summarizes the test method, data collected during the test, and results of previous tests. Appendix F also provides a detailed documentation and discussion of the results of tests performed on sister rod specimens. Measurement uncertainty for the measured data and calculated parameters was evaluated in Appendix G. A range of test loads are applied with a goal of defining the characteristic fatigue life curve.

In Phase 1 of the sister rod test program, seven of ORNL's 15 sister rods were selected for paired testing: one baseline fuel rod and one FHT fuel rod of each cladding type—M5, ZIRLO, and Zirc-4/LT-Zirc-4)—plus an extra ZIRLO-clad rod for additional data points since no ZIRLO-clad rods were tested in previous campaigns. The results from the FHT rods were compared with the results from the baseline rods to determine whether the fatigue lifetime is affected by dry storage thermal transients, and the results for the ZIRLO-clad rods are inspected to determine whether they are consistent with the results for rods clad with other alloys.

Twenty-five dynamic and six static CIRFT tests were performed using sister rod specimens, and one specimen slated for dynamic testing is yet to be tested. One data point that had erratic load cell data was discarded. A specimen that was tested in static mode and then further tested in dynamic mode was actually fractured in the static test and that datapoint has also been discarded. The results are tabulated in Table 16 with paired specimens shown together for easy comparison. Averages are provided for burnup, cycles to failure, strain, and flexural rigidity for comparison purposes. The results are consistent with previous data for the same size of fuel rods (17 × 17), as shown in Figure 15, although when trended with stress amplitude, as shown in Figure 16, the sister rod fatigue lifetimes appear to be on the lower side of other lifetime estimates, and some data are below the fatigue limit estimates [14, 15].

In FY22, ORNL performed tests of Zirc-4 unirradiated cladding tubes to provide data for comparison with the fuel rod segment tests. The empty cladding tests were also used to verify that previously reported fatigue data [14] on zirconium alloys (specifically Zircaloy-2 and Zirc-4) are representative of the tube geometry. Tests using irradiated defueled sister rod cladding will be performed in FY23 as a final verification with the O'Donnell-Langer data. A comparison of empty cladding tube fatigue with fuel rod fatigue also offers a direct indication of the effect of the pellet on fatigue performance. The discontinuities in the pellet cause stress concentrations on the cladding, so it is expected that the inclusion of the pellet will have a detrimental effect on the fatigue life of the fuel rod compared with cladding-only performance.

A review of the O'Donnell-Langer fatigue design limit development process [14] prompted a second look at the sister rod fatigue evaluation and its approach, as discussed in Appendix F and Appendix F2 of this report. Defining the fatigue data in terms of strain amplitude, as opposed to stress amplitude, is concluded to be more appropriate because it is independent of the composite nature of the fuel rod while stress can be calculated two different ways: (1) using the modified equivalent stress approach defined by Wang and Wang [12,13] to represent the cladding surface stress and (2) using the equivalent stress approach per Eq. (F-7). Further, strain is directly measured in the shipping tests that provide representative data for the expected applied fatigue cycles, which means it can be compared directly with the strain amplitude fatigue data.

As shown in Figure 17, a comparison of the high burnup fuel rod fatigue data with the fatigue performance of the cladding-only unirradiated tubes and open literature data on unirradiated and irradiated cladding alloys in terms of strain amplitude, it can be clearly observed that the fatigue performance of high burnup fuel rods is degraded compared with fatigue of cladding-only test specimens and test coupons. This degraded performance is likely caused by stress concentrations in the cladding where pellet cracks (or pellet-pellet interfaces) occur. A proposed ORNL fatigue design limit has been defined and is shown in Figure 17. Fatigue damage is concluded to not occur at strain amplitudes below the ORNL design fatigue limit. The fatigue limit decreased from ~0.20% for cladding alloys to ~0.06% for the high burnup fuel rods and is significantly lower than the O'Donnell-Langer design curve for zero-mean strain conditions. The stress concentration in the cladding due to pellet cracks is estimates as the ratio of the cladding fatigue limit to the fuel rod fatigue limit or 0.2%/0.06% = 3.3.

The review in Appendix F2 also considered whether to calculate fatigue damage as the sum of the ratio of applied cycles to cycles-to-failure or to compare a conservative representation of the applied cycles to the fatigue limit (the fatigue limit is strain amplitude below which fatigue damage does not occur—typically taken at 10^7 cycles). It was concluded that it is inappropriate to calculate fatigue damage when the applied cycles are less than the fatigue limit, because the fatigue curve must be extrapolated well beyond where there is fatigue data. Thus, the recommended approach is to define a conservative strain amplitude-based fatigue limit based on the fatigue data reported herein and show that a conservative estimate of the strain amplitude during transportation is below that fatigue limit.

In FY23, a deeper review of the O'Donnell-Langer fatigue design limit development process [14] illuminated that while the historic design limit includes the effect of non-zero mean stress the data were generated at zero-mean stress. This prompted a second look at the sister rod fatigue evaluation and its approach, as discussed in Appendix F. Because the SNF rods will be pressurized during transportation, the transportation-induced fatigue cycles will be applied at a non-zero mean stress. To evaluate the effects of the non-zero mean stress on the fatigue limit developed based on zero mean stress cycles, 4 tests were completed using 2 ZIRLO-clad segments (1 baseline and 1 FHT), 1 M5-clad segment (FHT), and 1 Zirc-4-clad segment (FHT). The resulting test data indicate that the non-zero mean strain may reduce the fatigue performance by ~40%. Even so, as shown in Figure 17, currently available transportation load and frequency estimates are significantly lower than the data and evaluated fatigue limits, suggesting fatigue damage will not occur.

Flexural rigidity is measured during the dynamic test at the specific test conditions. The results of the average dynamic flexural rigidity measurements are provided in Table 16. Although there is a mild trend of CIRFT-measured flexural rigidity with burnup, when considered with previous CIRFT data and the measurement uncertainty, it appears rigidity could also be relatively constant with burnup. The flexural rigidity of the specimen changes over the duration of the CIRFT test; and a rod subjected to many bending cycles is expected to have a lower flexural rigidity than an uncycled rod, especially at large applied moments. Because there is a relatively large uncertainty associated with the CIRFT-measured flexural rigidity, analysts using a flexural rigidity to assess structural performance should consider their application (pseudo-static or dynamic) and the range of values obtained through CIRFT and in four-point bending to select appropriate values as inputs to their models.

For the M5-clad and ZIRLO-clad segments, the FHT rods generally have a shorter fatigue lifetime and lower flexural rigidity than the corresponding baseline specimens, as shown in Figure 18. There are at least three potential sources for a reduction in flexural rigidity with heat treatment: (1) a permanent increase in cladding OD and the pellet-cladding gap that resulted from the increased pressure at temperature during the heat treatment, (2) the annealing of irradiation defects resulting from the heat treatment, and (3) the reorientation of precipitated hydrides in the cladding during the heat treatment that make it more susceptible to cladding fracture. Since hydride reorientation was not observed for all FHT rods, the difference in flexural rigidity and fatigue lifetime is unlikely to be related to hydride reorientation. Also, the primary

stresses during bending are in the axial direction, and failure is not expected to be significantly influenced by the direction of precipitated hydrides. However, some irradiation defect annealing could have occurred during the heat treatment, particularly on the M5-clad rod, as discussed in Appendix A. The reduced fatigue lifetime is produced at similar applied bending moments because a larger deflection of the specimen is imposed at lower flexural rigidity. A comparison between the LT Zirc-4-clad baseline and the Zirc-4-clad FHT specimen flexural rigidity is not valid due to the differences in operation of the reactor rods.

One specimen with visible grid-to-rod fretting (GTRF) marks was tested with the marks aligned (as possible) with the point of the peak rod deflection (expected to be the highest cladding strain location), and the GTRF marks did not reduce the fatigue lifetime. The GTRF marks on this specimen are not considered representative or bounding; the specimen was selected based on availability only, and further tests should be completed to fully explore the effect.

The fractured CIRFT specimens were imaged, and all photos are provided in Appendix F. Typical optical views of the different fracture observations are provided in Figure 19. There is no visible difference in the fracture mode from baseline to FHT rods. The specimens with fatigue lifetimes lower than other data did not fracture in an anomalous manner. The F35P17 Zirc-4-clad rods seemed to fracture in a more brittle mode than the other specimens with deeper tearing of the cladding across the pellet body.

Scanning electron microscopy (SEM) is being used to further explore the fracture modes. Fractography of two unirradiated cladding-only CIRFT specimens are documented in Appendix F; they provide better understanding of how failure occurs without the presence of the pellet, which will provide a reference for the fractography on the failed fuel rods. SEM imaging of two CIRFT specimens has been completed and are discussed in Appendix F, Section F-8.5. Figure 19 shows the apparent fatigue crack initiation site for 3D8E14-2963-3116, a baseline ZIRLO specimen, that was fractured in the CIRFT test. Future work will investigate the role of precipitated hydrides in the fracture.

Equipment for performing the cumulative shock tests has been developed and was tested out of cell. This test was meant to simulate the cumulative effects of rod-to-rod or rod-to-basket impacts. The physical testing and finite element analysis performed, as discussed in Appendix F, indicate that delivering a shock to a CIRFT specimen mounted in a dogbone yields too high an impact load. Further, in FY22 it was determined that this type of shock is highly unlikely to occur. Given these facts, the planned cumulative tests were canceled, and the allocated test specimens were used in FY23 for non-zero mean stress tests.

In FY23, calibration testing of the in-cell CIRFT equipment was completed. The tests included a comparison with the calibrated out-of-cell CIRFT system because the load cells and linear variable differential transducers (LVDTs) in the hot cell cannot be directly calibrated. The uncertainty in the strain amplitude was determined to be ± 0.022%. In addition, during the calibration of the in-cell CIRFT, it was determined that the dynamic correction factor used in processing the data is 1.0, rather than the value used previously (i.e., ~0.82). This suggests that there is a small conservative bias in the previously reported strain amplitudes for high burnup fuel rods. However, because this bias results in a conservative change in the reported strain amplitude that is within the uncertainty, the previous dynamic correction factor (~0.82) remains acceptable for strain amplitude calculations when fatigue testing irradiated fuel rods. More details of the calibration testing are provided in Appendix F3.

Also, in FY23, the ORNL-developed Fuel Rod Fatigue Design Curve (see Figure 17) was used to further evaluate outlier data points. The evaluation points towards a potential effect of total hydrogen content (unrelated to hydride orientation) on fatigue performance.

In FY22, simulation of flexural rigidity, pellet-pellet bonding, and pellet-clad bonding were initiated to better understand test results and provide prediction capability, and this work continued in FY23. Results are reported in Sections 12.1 and 12.3 of this report, and, once the quasi-static condition tests are well simulated, the developed understanding will be applied to dynamic fatigue conditions.

Table 16. Results arranged by paired specimens (baseline vs. FHT) for static/dynamic and dynamic CIRFT.

See Appendix F and G for a discussion of the dynamic flexural rigidity and applied strain amplitude uncertainties.

Baseline rods								Heat-treated rods							
Specimen ID			Cladding type	Estimated specimen average burnup (GWd/MTU)	Cycles to failure	Dynamic flexural rigidity (N-m^2)	Applied strain amplitude (%)	Specimen ID			Cladding type	Estimated specimen average burnup (GWd/MTU)	Cycles to failure	Dynamic flexural rigidity (N-m^2)	Applied strain amplitude (%)
30AD05	0697	0850[a]	M5	58	3,368	15.6	0.47	30AE14	0672	0825[a]	M5	56	1,630	20.5	0.36
30AD05	2050	2203		59	133,000	28.7	0.08	30AE14	3156	3309		56	113,000	23.2	0.10
30AD05	2630	2783		59	22,300	28.0	0.18	30AE14	2850	3003		60	9,800	23.6	0.22
Average				59	52,889	24.1	0.24					57	41,477	22.4	0.23
3A1F05	1853	2006[a]	LT Zirc-4	56	1,300	19.3	0.39	F35P17	1855	2008[a,b,c]	Zirc-4	53	525	28.7[d]	0.16[d]
3A1F05	3367	3520		44	214,000	29.7	0.06	F35P17	2027	2180		52	1,340,000	26.8	0.07
3A1F05	2025	2178		56	48,200	23.2	0.18								
3A1F05	3214	3367		48	3,450	21.6	0.19	F35P17	3159	3312[b]		47	773	30.7	0.15
Average				51	66,738	24.8	0.14					51	447,099	28.8	0.11
3D8E14	0719	0872[a]	ZIRLO	64	9,589	18.4[d]	0.39[d]								
3D8E14	2412	2565[e]		64	191,000	31.3	0.08								
3D8E14	2963	3116		62	39,700	28.1	0.15								
3D8E14	1178	1331		63	212,000	30.9	0.08								
6U3K09	2310	2463		59	17,500	30.2	0.20	3F9N05	0719	0872[a]	ZIRLO	59	3,540	18.0	0.41
6U3K09	2463	2616		59	39,200	32.4	0.13	3F9N05	2329	2482		59	189,000	22.6	0.10
6U3K09	2635	2788		58	110,000	37.1	0.08	3F9N05	2710	2863		57	33,000	21.8	0.19
6U3K09	3200	3353		50	34,900	30.0	0.15								
6U3K09	3353	3506		46	14,100	27.0	0.21								
Average zero mean tests				60	50,400	31.4	0.15					58	75,180	21.8	0.19
Non-zero mean strain tests[f]															
3D8E14	3225	3378	ZIRLO		352,000	32.1	0.08	3F9N05	3440	3593	ZIRLO		280,000	27.4	0.06
								F35P17	3312	3465	Zirc-4		188,000	27.5	0.06
								30AE14	3003	3156	M5		315,000	28.6	0.05

[a] Dynamically tested following a static test.
[b] Erratic load cell data were recorded during the test. The applied moment and strain amplitude were likely higher.
[c] Deeper examination indicates that this specimen broke during the static test; therefore, the dynamic test results are invalid.
[d] Estimated.
[e] Specimen had a GTRF mark in the gauge section that was aligned (as possible) with the expected maximum strain location.
[f] Target non-zero mean strain, 0.05%.

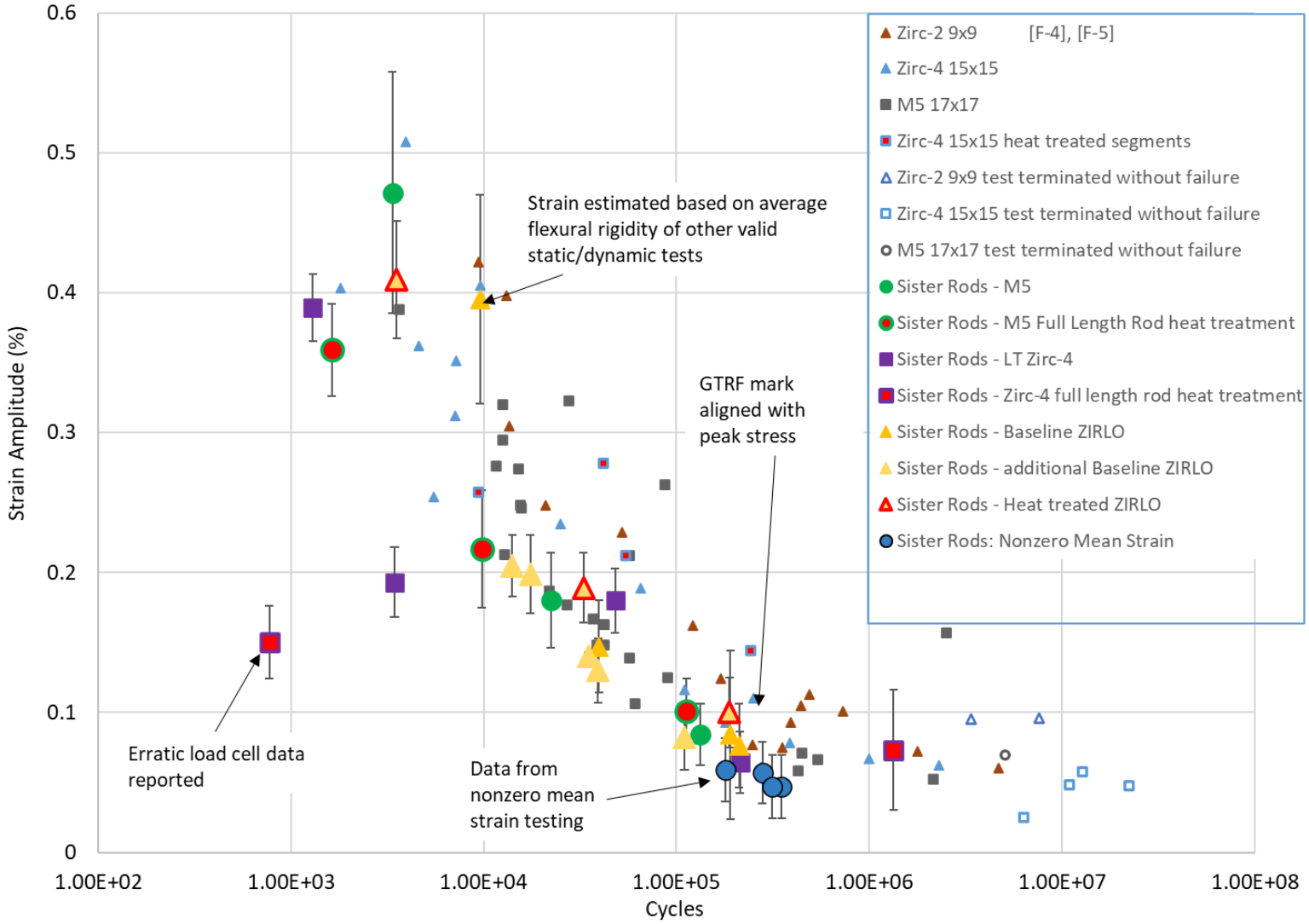

Figure 15. Results of sister rod CIRFT tests plotted with previous data, applied moment vs. cycles to failure. The error bars on the sister rod data represent the calculated uncertainty (0.8 N-m) (see Section G-3.3, Appendix G).

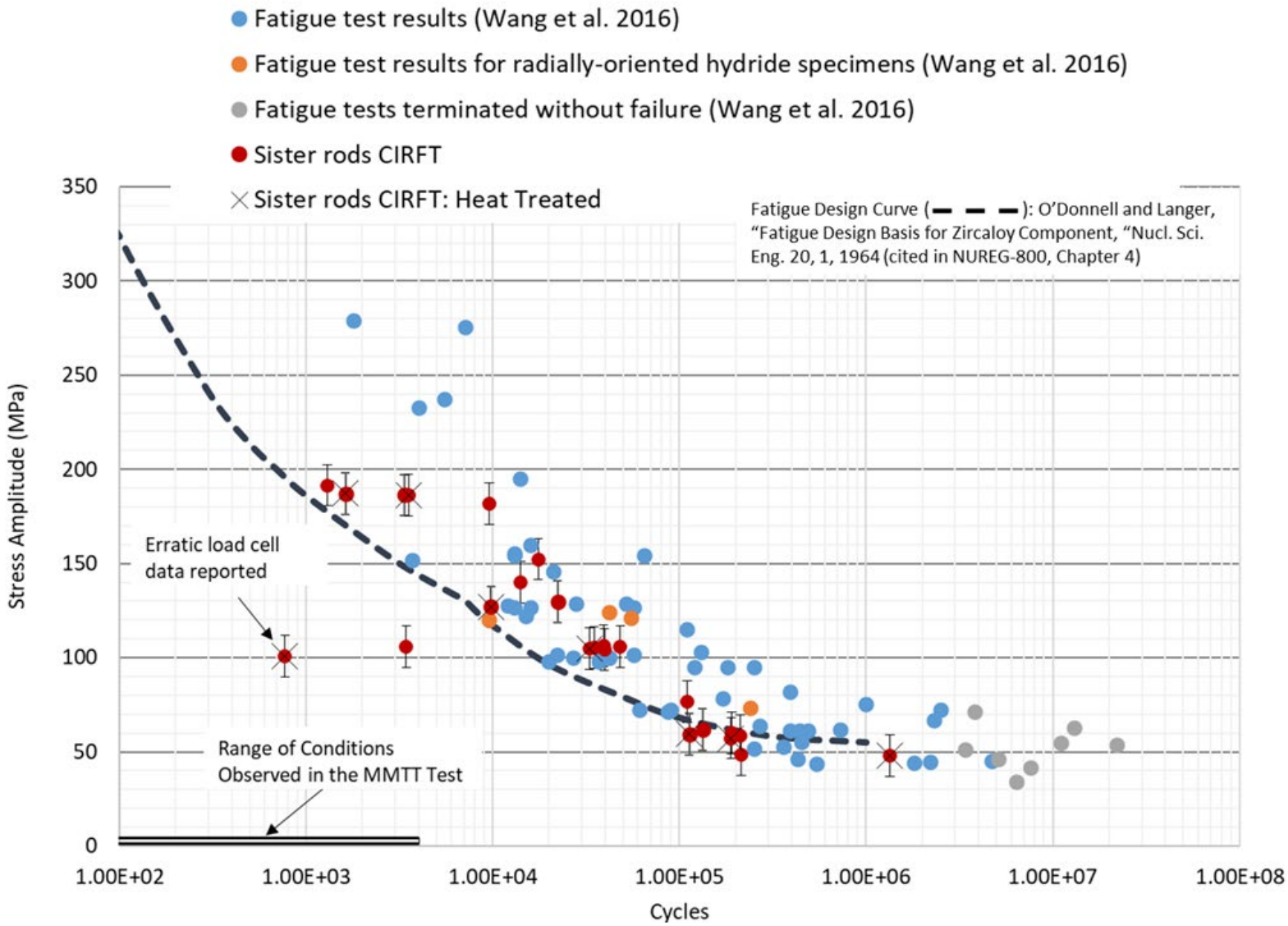

Figure 16. Comparison of CIRFT stress amplitude vs. cycles to failure with other fatigue limits. The error bars on the sister rod data represent the calculated uncertainty (see Section G-3.5, Appendix G). The range of conditions observed in the MMTT test are provided for perspective.

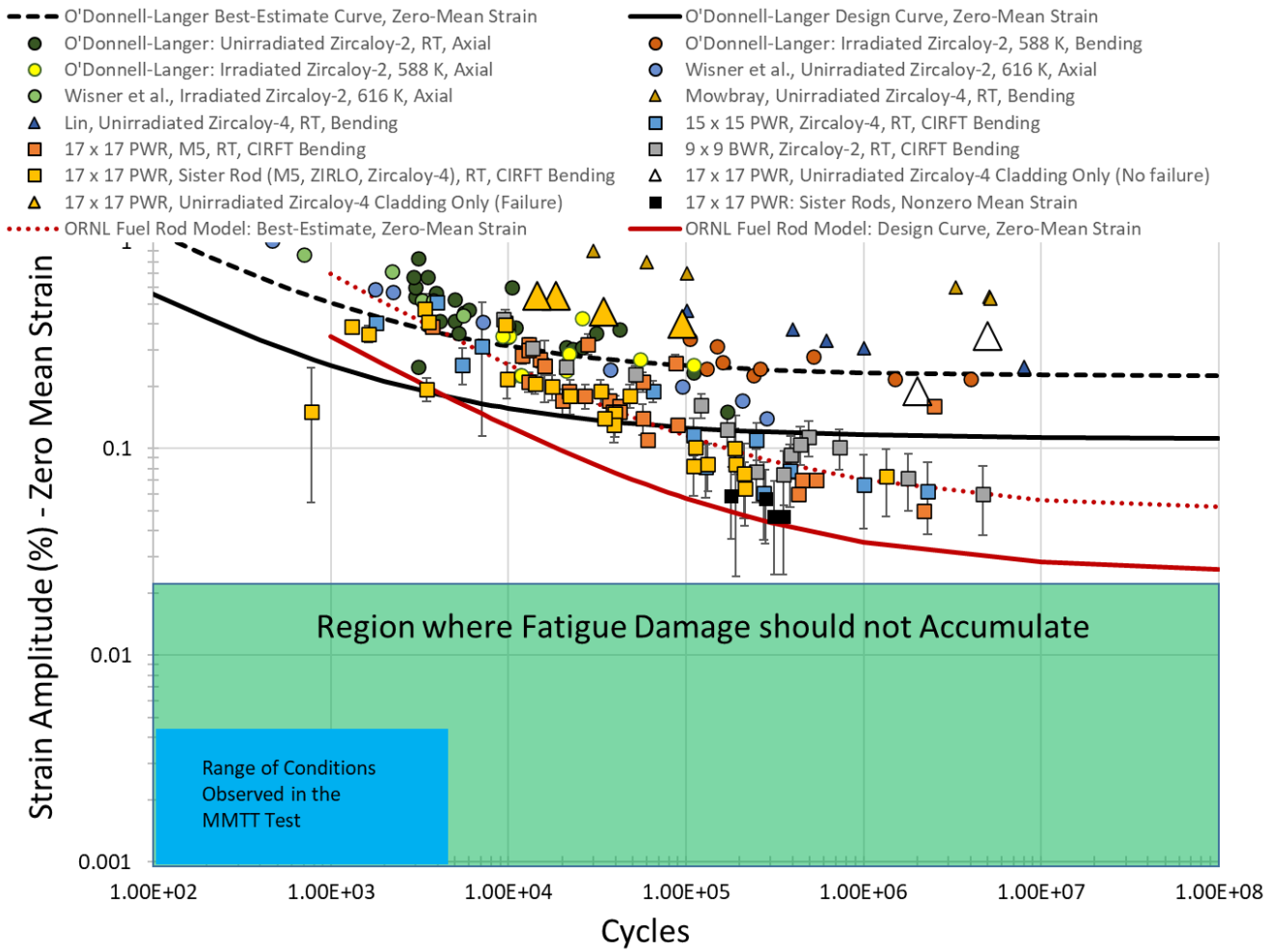

The error bars on the sister rod data represent the calculated uncertainty in Section G-3.5, Appendix G.

Figure 17. Strain amplitude as a function of cycles to failure for the sister rods compared with the fatigue data on cladding alloys [14], the proposed ORNL limit for fuel rods, the region where fatigue damage does not accumulate, and the range of conditions observed in the MMTT test (see Appendix F2).

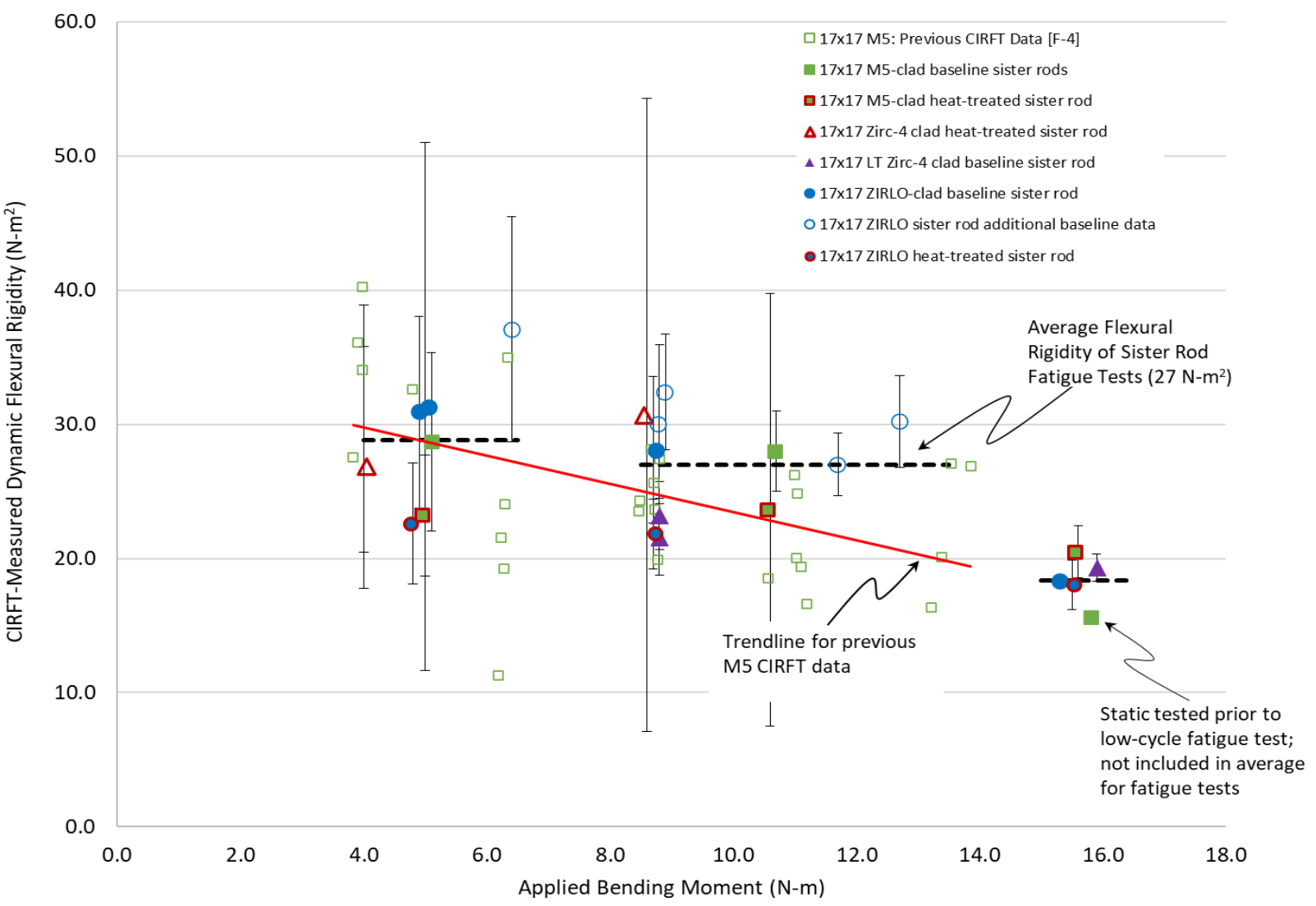

Figure 18. CIRFT-measured dynamic flexural rigidity of the heat-treated and baseline specimens.

(a) Typical view of a circumferential fracture at a pellet-pellet interface (3F9N05-2710-2863)

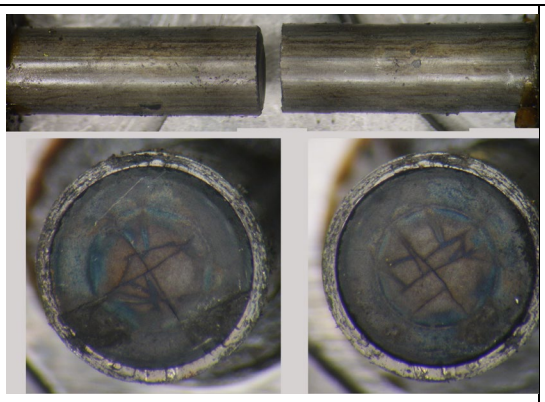

I Jagged fracture observed on the Zirc-4-clad specimens (F35P17-1855-2008)

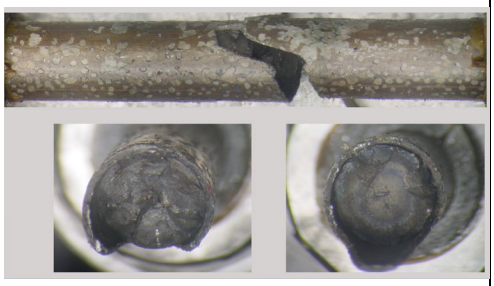

(b) Typical view of a fracture through the pellet body with partial tearing of the cladding (30AE14-3156-3309)

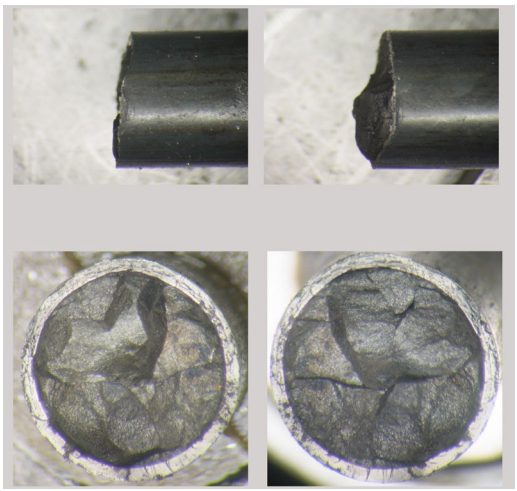

(d) 120× and 350× images of quadrant 4 in sample 3D8E14-2963-3116 showing signs of fatigue striations typical of fatigue crack propagation. The flatness of the feature on the cladding ID might be associated with fatigue initiation. There are also circumferential cracks near the cladding OD that might be associated with hydrides.

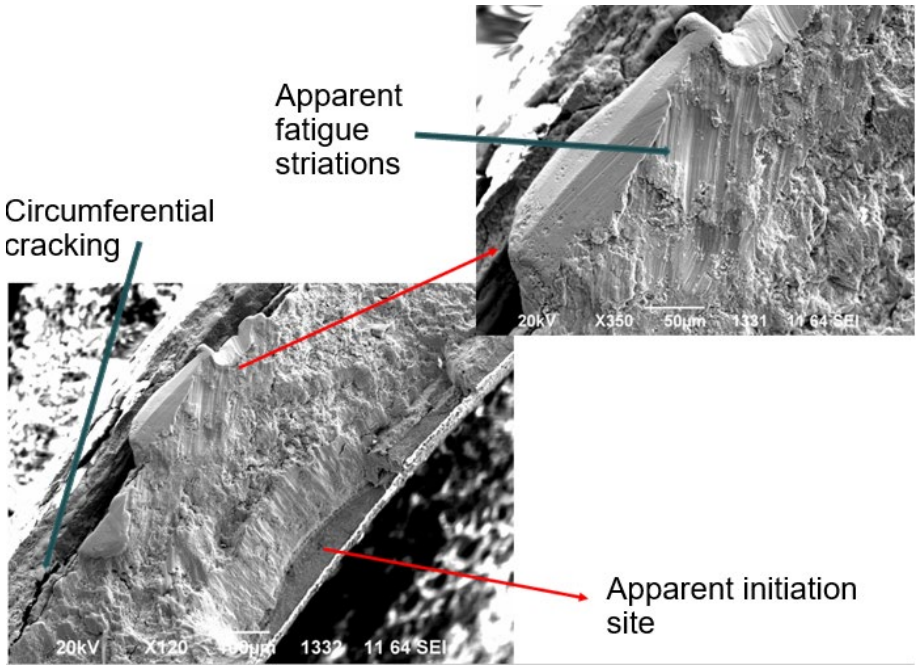

Figure 19. Representative (a, b, and c) optical images of CIRFT-fractured rod segments and (d) SEM fractography images.

12. Mechanical Testing

To provide the capability for mechanical testing, a large Instron load frame (65 × 31 × 29 in.) with a 30 kN capacity (~1 ton of loading force) was installed in the IFEL north hot cell in June 2020. The cell location was selected based on its accessibility and its lower dose rates (~150 R/h). During FY20, the load frame was modified for durability in the radiation field and to provide remote manipulation capabilities. Lead shielding was placed around the load frame's instrumentation string to provide more protection from radiation damage. Unfortunately, the Instron load frame succumbed to the high-radiation environment in the hot cell early in FY22 and is no longer functional. A replacement load frame has been procured and is expected to be available for continued testing late in FY24. In the interim, the "MiniMight" load frame was designed and fabricated to provide a capability for four-point bending and aerosol collection within the limited hot cell space and within the near-term time frame (see Appendix E).

Although testing of unpressurized segments in 4PB, axial tension, and ring compression provide relevant and useful data, pressurized segments are needed for aerosol collection experiments. In FY22, a process for pressurizing fuel rod segments for aerosol testing was designed and tested on unirradiated cladding segments. The approach uses off-the-shelf Swagelok® compression tube fittings, as shown in Figure 20, and has been demonstrated to hold pressures up to 1,500 psi. Pressure is monitored by a miniature diaphragm pressure transducer (Omega® PX600-2KGV). Procedures for attaching the Swagelok® fittings in the hot cell had been previously developed and will be adapted in a specific jig for assembling the capped rod segment test assemblies. In FY23, the assembly jig was fabricated. The set up will be used for pressurized aerosol specimen tests in FY24.

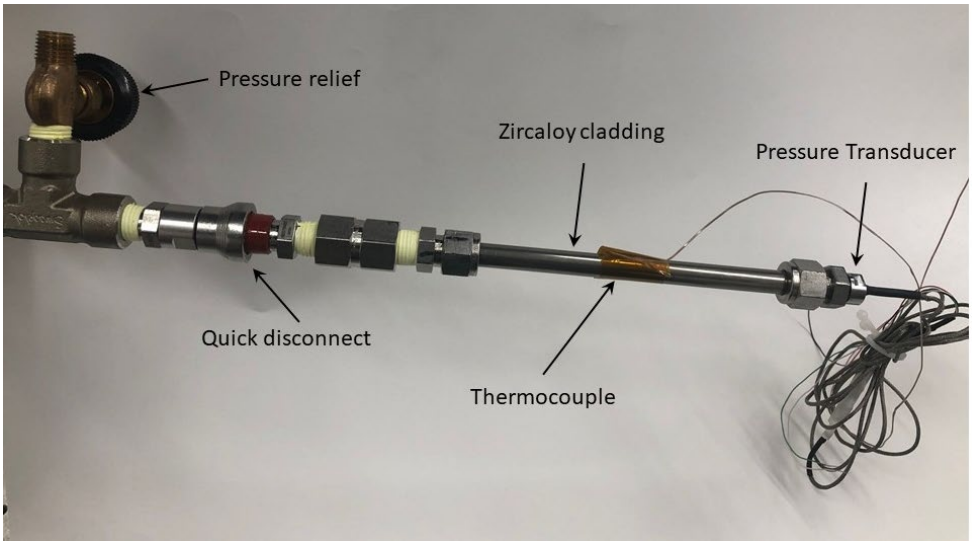

Figure 20. Set up for pressurization of sister rod segments for aerosol collection experiments.

However, this configuration is not compatible with the CIRFT machine and the required dogbone specimen end fittings, so a second system is being developed to support pressurized CIRFT tests.

12.1 Four-Point Bend Tests

The 4PB test provides values for the elastic modulus in bending and the flexural stress and flexural strain response. It is the test traditionally used to study brittle materials in which the number and severity of flaws exposed to the maximum stress is directly related to the flexural strength and crack initiation. The load frame with its test fixturing (described in Appendix E) applies a constant bending moment over the inner 42.42 mm (1.67 in.) of the 152.4 mm (6 in.) test specimen. For these tests, the upper fixture is advanced at 0.050 mm/s in the downward direction, whereas the lower fixture is fixed and does not move. The 4PB test can be evaluated using simple beam theory given the nominal dimensions of the rod specimen and test fixture, idealizing the composite fuel rod segment as a solid cylindrical geometry made of an isotropic material. The evaluation method and its uncertainties are discussed within Appendix E and Appendix H. The beam theory approach treats the fuel rod segment as a simplified elastic beam as a practical approach to evaluate the test data and allow for comparisons with other materials, but the resulting evaluated properties should not be considered cladding material properties.

At the end of FY21, all Phase 1 4PB (DE.07) tests were complete except for five tests planned for aerosol collection. Both RT and 200°C tests were completed. Video and audio records of the tests were acquired, along with the displacement and load. Each test segment was weighed before testing. A tray was placed below the specimen to catch debris, and the broken segments and debris were weighed after each test.

Table 17 summarizes the evaluated results of the tests completed to date. Stress, strain, 0.2% offset yield strength, flexural modulus, and flexural strength were calculated. The uncertainty of the 4PB test in ORNL's configuration was calculated (Appendix H) and integrated with the results. In the process of calculating the uncertainties, errors in the stress and strain calculations reported in the 11/30/2020 revision of this report were found and corrected. Figure 21 provides the stress vs. strain plot for the RT tests, and Figure 22 plots the stress vs. strain for the 200°C tests. The FHT M5 and ZIRLO-clad specimens generally have higher ductility than the baseline specimens, but it is difficult to come to any firm conclusions about whether the heat treatments affected specimen performance with the limited data available. Given the limited number of tests, it is possible that the difference between the FHT and baseline specimens is within the normal variation and/or could be a trend related to burnup. The M5-clad rods are more ductile than specimens that have ZIRLO, Zirc-4, or LT Zirc-4-clad specimens. The flexural rigidity measured using 4PB, as listed in Table 17 and plotted Figure 23, is consistent with that measured using CIRFT (Section 11) but does not indicate lower rigidity for heat-treated rods, as shown in Figure 24. As expected, the rigidity at 200°C is lower than the RT rigidity.

The amount of fuel released during fracture was monitored by weighing each specimen before and after the test and weighing the debris collected. The largest difference from pretest to posttest weight was 1.7 ± 0.1 g for F35P17-1472-1625 (RT test). There is not a trend of mass loss with test temperature or burnup. There is a tendency for the RT tests to have more mass loss, likely because the cladding fracture is more energetic at RT than at 200°C. The maximum mass lost represents about one-quarter of a pellet, whereas the more typical mass loss is less than one-tenth of a full pellet. Often, the released material was composed of small particulate, as shown in Figure 25. Several 4PB tests will be completed with the aerosol collection system to better quantify the size distribution and quantity of aerosol particles released during fracture, as discussed in Section 13. Images of the fractured 4PB segments are available in Appendix E2.

Table 17. Measured and calculated 4PB data.

Test specimen	Cladding alloy	Heat-treatment	Estimated burnup (GWd/MTU) [E-7]	Test temp. (°C)	Average specimen OD [E-7]	Crosshead extension, Δ_f, at failure (mm)	Maximum deflection, Δmax, at failure (mm)*	0.2% yield strength (MPa)*	Flexural strength (MPa)
30AD05-1299-1452	M5	---	60	25.7	9.423	8.33	9.57 ± 0.09	533 ± 11	641 ± 13
30AE14-0978-1131	M5	FHT	59	26.6	9.459	11.69	13.43 ± 0.13	481 ± 10	609 ± 12
3D8E14-1025-1178	ZIRLO	---	64	25.3	9.500	7.41	8.51 ± 0.08	617 ± 12	766 ± 15
3F9N05-2063-2216	ZIRLO	FHT	59	24.7	9.471	10.64	12.22 ± 0.12	526 ± 10	717 ± 14
3A1F05-1279-1432	LT Zirc-4	---	57	26.4	9.465	7.47	8.59 ± 0.08	616 ± 12	768 ± 15
F35P17-1319-1472	Zirc-4	FHT	52	24.9	9.503	5.36	6.16 ± 0.06	555 ± 11	640 ± 13
F35P17-1472-1625	Zirc-4	FHT	53	27.2	9.531	6.52	7.49 ± 0.07	565 ± 11	693 ± 14
30AD05-0850-1003	M5	---	60	200.0	9.429	5.77	6.63 ± 0.06	405 ± 8	461 ± 9
30AD05-1800-1953	M5	---	59	200.0	9.423	6.07	6.97 ± 0.07	443 ± 9	502 ± 10
30AE14-0825-0978	M5	FHT	58	200.0	9.457	11.60	13.33 ± 0.13	401 ± 8	503 ± 10
30AE14-2050-2203	M5	FHT	60	200.0	9.454	12.11	13.91 ± 0.13	385 ± 8	502 ± 10
3D8E14-0872-1025	ZIRLO	---	64	200.0	9.497	6.91	7.93 ± 0.08	518 ± 10	644 ± 13
3D8E14-1907-2060	ZIRLO	---	64	200.0	9.492	6.97	8.01 ± 0.08	460 ± 9	583 ± 12
3F9N05-0872-1025	ZIRLO	FHT	59	200.0	9.465	7.89	9.07 ± 0.09	461 ± 9	583 ± 12
3F9N05-1910-2063	ZIRLO	FHT	59	200.0	9.469	9.15	10.51 ± 0.10	448 ± 9	588 ± 12
3A1F05-1432-1585	LT Zirc-4	---	56	200.0	9.459	5.03	5.78 ± 0.06	519 ± 10	589 ± 12
3A1F05-2230-2383	LT Zirc-4	---	54	200.0	9.480	4.91	5.64 ± 0.05	481 ± 10	550 ± 11
F35P17-2230-2383	Zirc-4	FHT	51	200.0	9.514	7.50	8.61 ± 0.08	461 ± 9	588 ± 12
				Average at RT:		8.20	9.42 ± 0.09	556 ± 11	691 ± 14
				Average at 200°C:		7.63	8.76 ± 0.08	453 ± 9	554 ± 11

Table 14. Measured and calculated 4PB data (continued).

Test specimen	Cladding alloy	Heat-treatment	Estimated burnup (GWd/MTU) [E-7]	Test temp. (°C)	Average specimen OD [E-7]	Failure strain (%)*	Flexural modulus (GPa)	Elastic region flexural rigidity (N-m^2)	Plastic region flexural rigidity (N-m^2)*
30AD05-1299-1452	M5	---	60	25.7	9.423	2.6 ± 0.04	57.88 ± 1.45	22.4 ± 0.5	1.9 ± 0.04
30AE14-0978-1131	M5	FHT	59	26.6	9.459	3.8 ± 0.06	57.17 ± 1.43	22.5 ± 0.5	1.1 ± 0.03
3D8E14-1025-1178	ZIRLO	---	64	25.3	9.500	2.3 ± 0.04	58.04 ± 1.45	23.2 ± 0.5	5.1 ± 0.12
3F9N05-2063-2216	ZIRLO	FHT	59	24.7	9.471	3.3 ± 0.06	55.34 ± 1.38	21.9 ± 0.5	3.9 ± 0.09
3A1F05-1279-1432	LT Zirc-4	---	57	26.4	9.465	2.3 ± 0.04	59.25 ± 1.48	23.3 ± 0.5	6.7 ± 0.15
F35P17-1319-1472	Zirc-4	FHT	52	24.9	9.503	1.7 ± 0.03	54.24 ± 1.36	21.7 ± 0.5	8.5 ± 0.20
F35P17-1472-1625	Zirc-4	FHT	53	27.2	9.531	2.2 ± 0.04	54.72 ± 1.37	22.2 ± 0.5	6.2 ± 0.14
30AD05-0850-1003	M5	---	60	200.0	9.429	2.0 ± 0.03	51.44 ± 1.29	20.0 ± 0.5	2.0 ± 0.04
30AD05-1800-1953	M5	---	59	200.0	9.423	2.0 ± 0.03	53.60 ± 1.34	20.7 ± 0.5	2.2 ± 0.05
30AE14-0825-0978	M5	FHT	58	200.0	9.457	3.7 ± 0.06	55.97 ± 1.40	22.0 ± 0.5	0.8 ± 0.02
30AE14-2050-2203	M5	FHT	60	200.0	9.454	4.6 ± 0.08	53.66 ± 1.34	21.0 ± 0.5	1.2 ± 0.03
3D8E14-0872-1025	ZIRLO	---	64	200.0	9.497	2.2 ± 0.04	54.09 ± 1.35	21.6 ± 0.5	4.7 ± 0.11
3D8E14-1907-2060	ZIRLO	---	64	200.0	9.492	2.2 ± 0.04	50.97 ± 1.27	20.3 ± 0.5	4.7 ± 0.11
3F9N05-0872-1025	ZIRLO	FHT	59	200.0	9.465	2.5 ± 0.04	50.60 ± 1.27	19.9 ± 0.5	3.5 ± 0.08
3F9N05-1910-2063	ZIRLO	FHT	59	200.0	9.469	2.9 ± 0.05	50.64 ± 1.27	20.0 ± 0.5	3.3 ± 0.08
3A1F05-1432-1585	LT Zirc-4	---	56	200.0	9.459	1.6 ± 0.03	54.27 ± 1.36	21.3 ± 0.5	7.4 ± 0.17
3A1F05-2230-2383	LT Zirc-4	---	54	200.0	9.480	1.6 ± 0.03	51.25 ± 1.28	20.3 ± 0.5	6.9 ± 0.16
F35P17-2230-2383	Zirc-4	FHT	51	200.0	9.514	2.4 ± 0.04	48.77 ± 1.22	19.6 ± 0.5	4.3 ± 0.10
				Average at RT:		2.6 ± 0.04	56.66 ± 1.42	22.5 ± 0.6	5.7 ± 0.11
				Average at 200°C:		2.4 ± 0.04	52.30 ± 1.31	20.6 ± 0.5	4.4 ± 0.09

* These values are based on the calculated maximum specimen deflection using elastic beam theory as described in Appendix E, Section E-2.1.4.

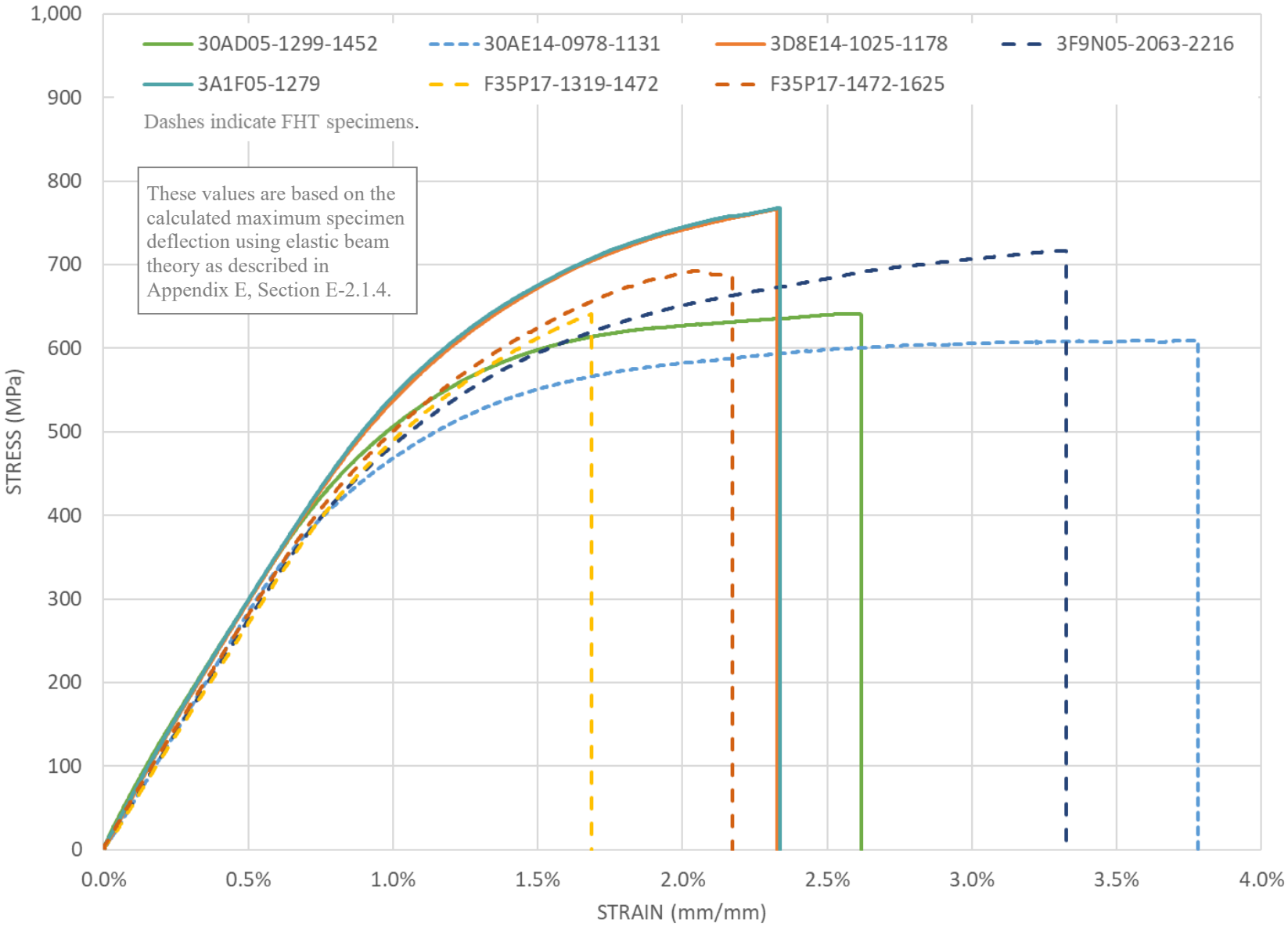

Figure 21. Stress vs. strain plot for RT data.

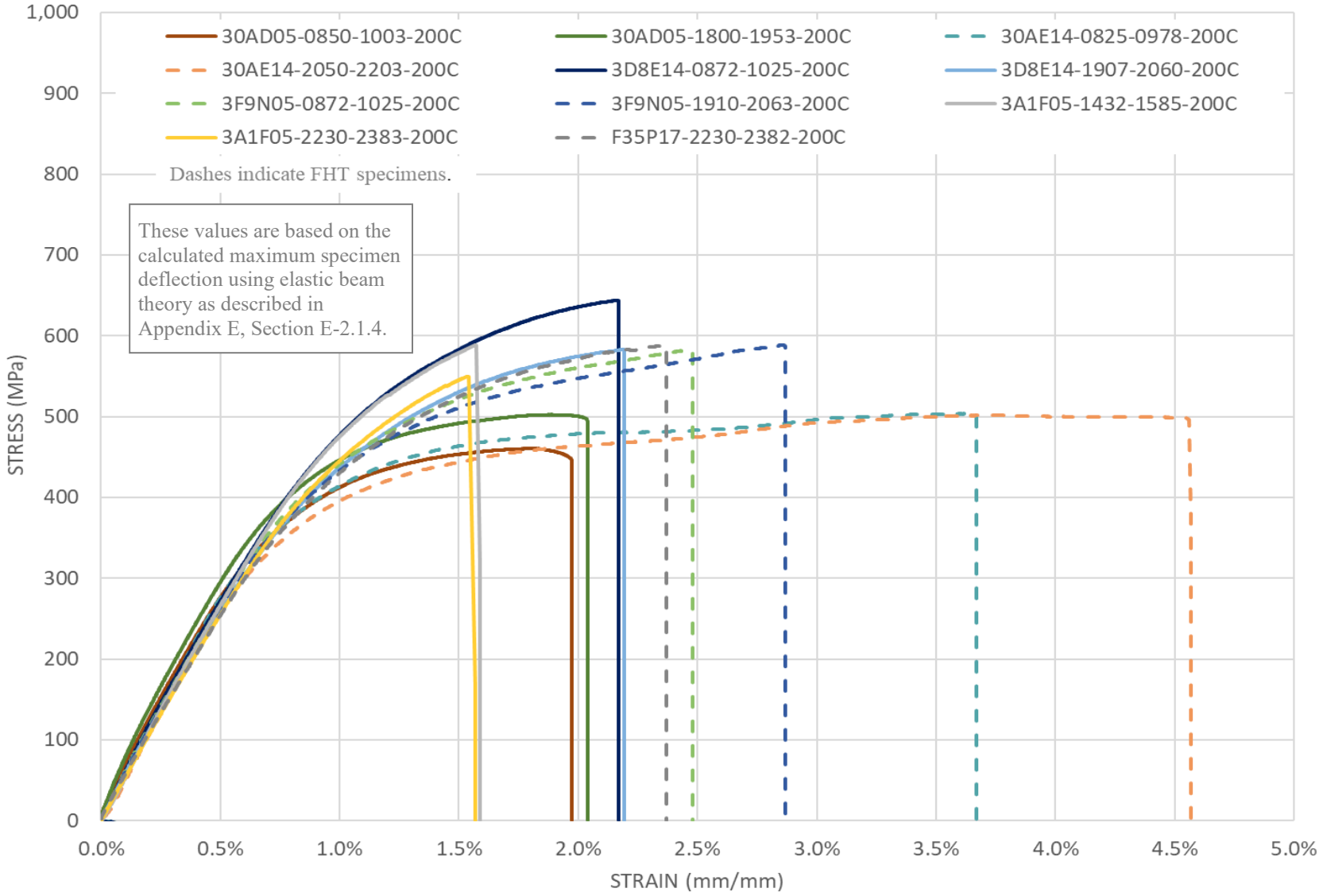

Figure 22. Stress vs. strain plot for 200°C data.

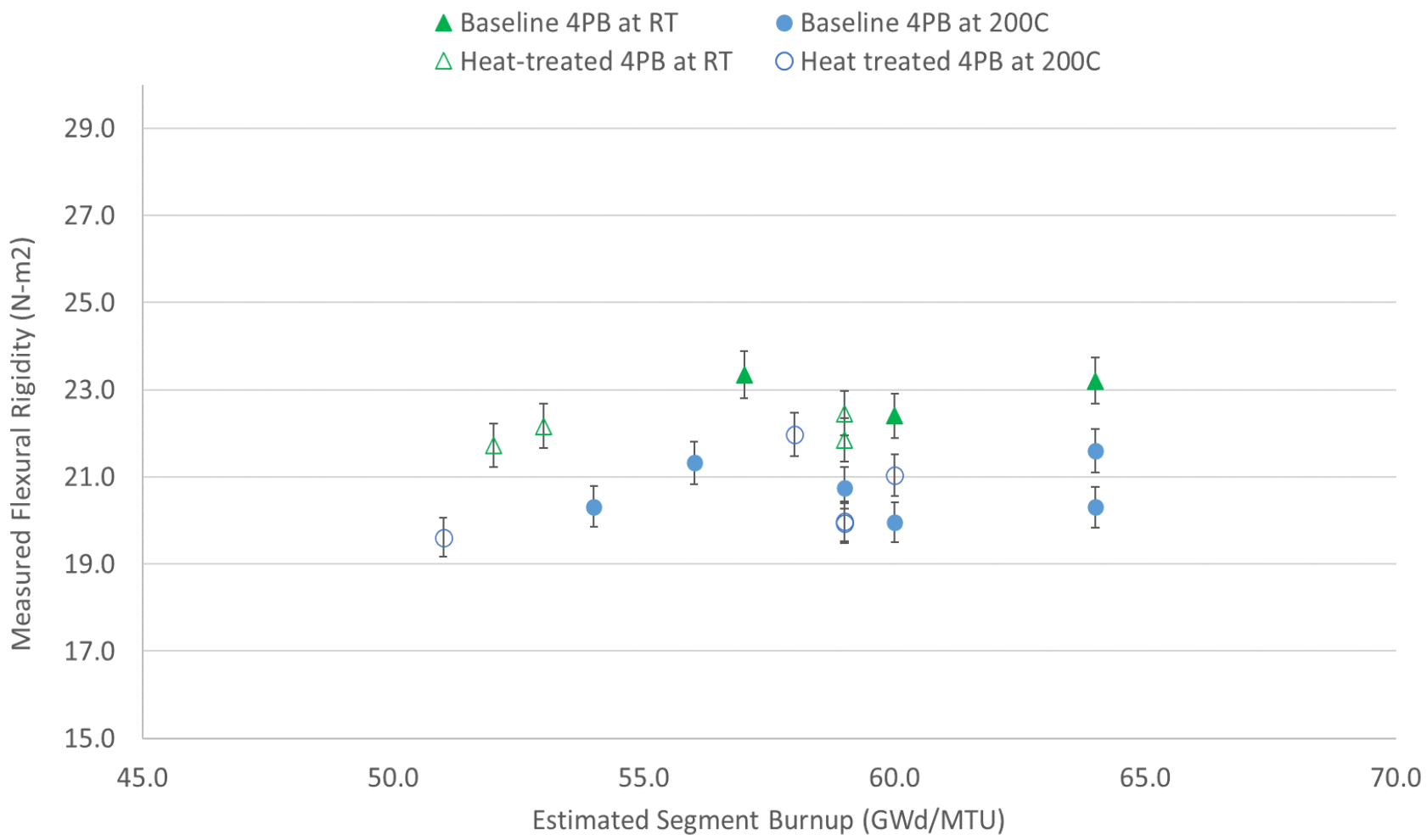

Figure 23. Segment rigidity in the elastic region measured in 4PB vs. estimated local burnup at RT and 200°C.

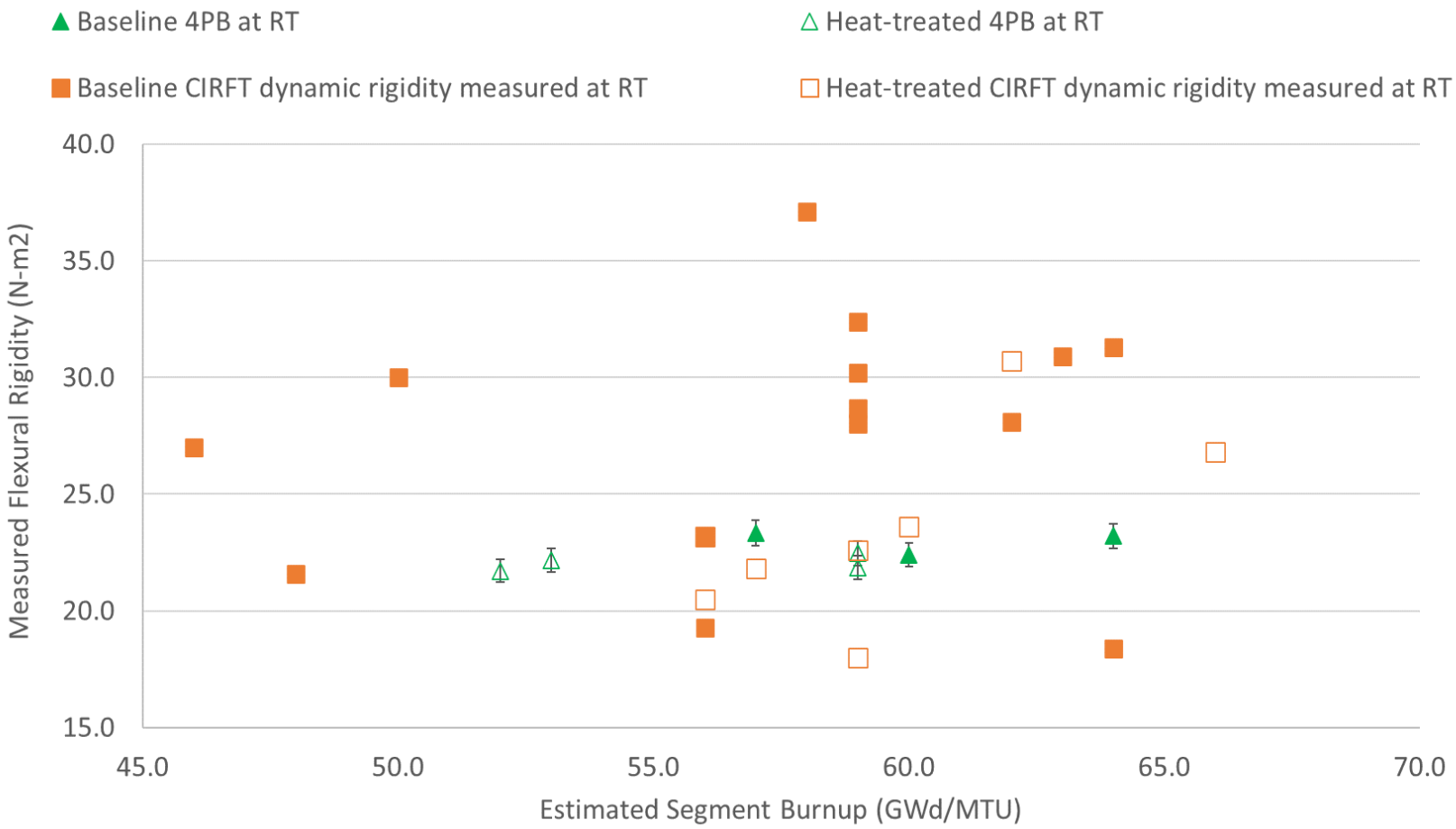

Figure 24. A comparison of CIRFT-measured flexural rigidity and 4PB-measured flexural rigidity for heat-treated and baseline rods at RT.

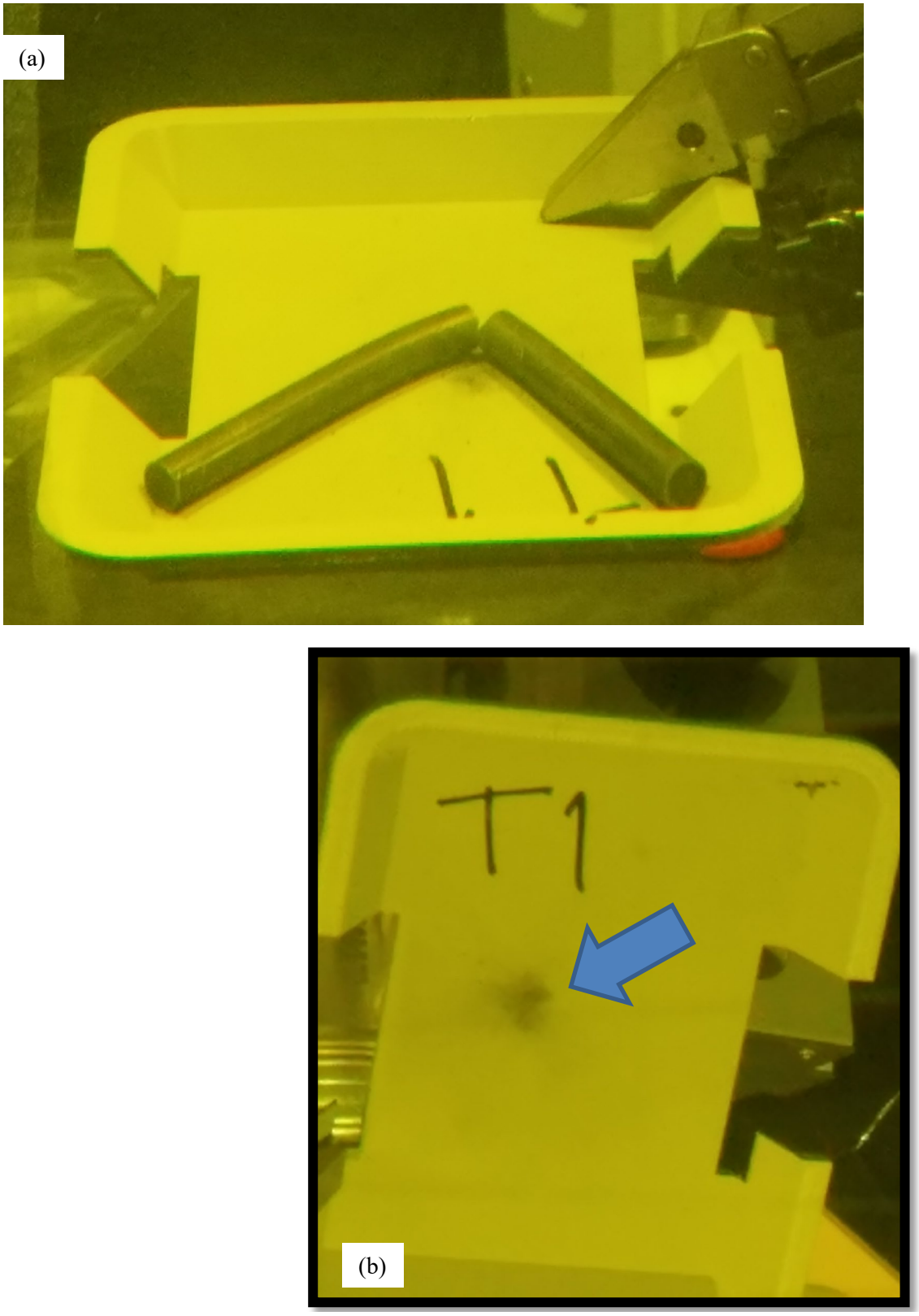

Figure 25. (a) Post-test debris was captured by a catch tray located below the specimen with (b) the typical RT debris field composed of small particles.

In FY22, Finite element modeling of the 4PB test was performed using ANSYS Workbench 2022. The simplified modeling of fragmented pellets in cladding is the first step toward better understanding of the 4PB test results, the overall performance of a composite rod, and the functionality of pellet-clad bonding, pellet-pellet interfaces, and pellet cracks in bending. The improved understanding allows for better informed modeling of normal and accident transport conditions and more accurate predictions from transportation models.

The simplified fragmented pellet finite element model was constructed with the support and loading fixtures used in the 4PB test included, as shown in Figure 26. The fuel rod segment modeled is ~152 mm in length and 9.5 mm in diameter.

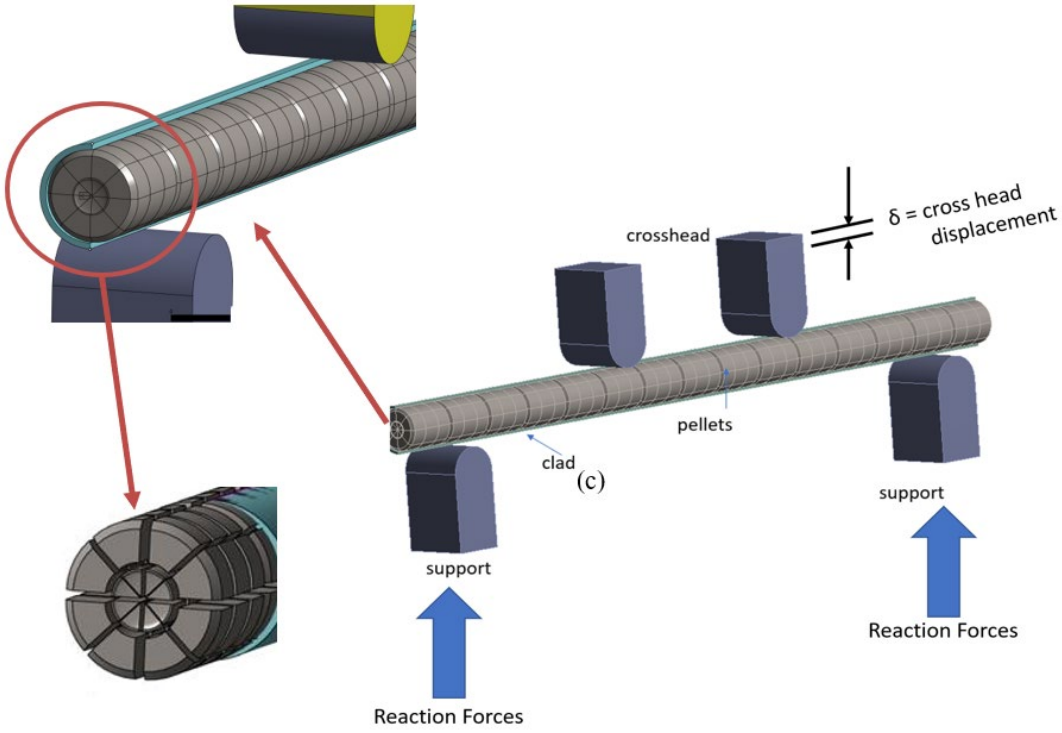

Figure 26. The 4PB finite element model with explicit pellets having simplified wedge cracks.

Using an elastic modulus of 200 GPa [30] and Poisson's Ratio of 0.32 [30] for the UO_2 pellet fragments, the 4PB test of LT Zirc-4 segment 3A1F05-1279-1432 was simulated assuming (1) pellet fragment OD bonding with the cladding ID and frictional sliding at cracks internal to each pellet and (2) a fully frictional response with no bonding between the cladding and the pellet fragments. As shown in Figure 27, neither of these bounding cases accurately predict the test measurements, and some combination of the two extremes is more appropriate. Initial work to refine the model was focused on calibrating the model using Young's modulus, and a very good model prediction of the test results can be obtained in this manner, as shown in Figure 28. While using the pellet modulus as a calibration factor is considered non-physical, it suggests potential future model changes needed to better predict the data. The need to reduce the elastic modulus to calibrate the model, with the corresponding reduction in bending stiffness, is thought to be related to the network of cracks in the pellets, and future simulations are recommended to incorporate a better representation of true crack patterns, similar to the RCT realistic pellet crack model (see Section 12.3).

The details of the modeling are provided in Appendix E, Section E-2.4.

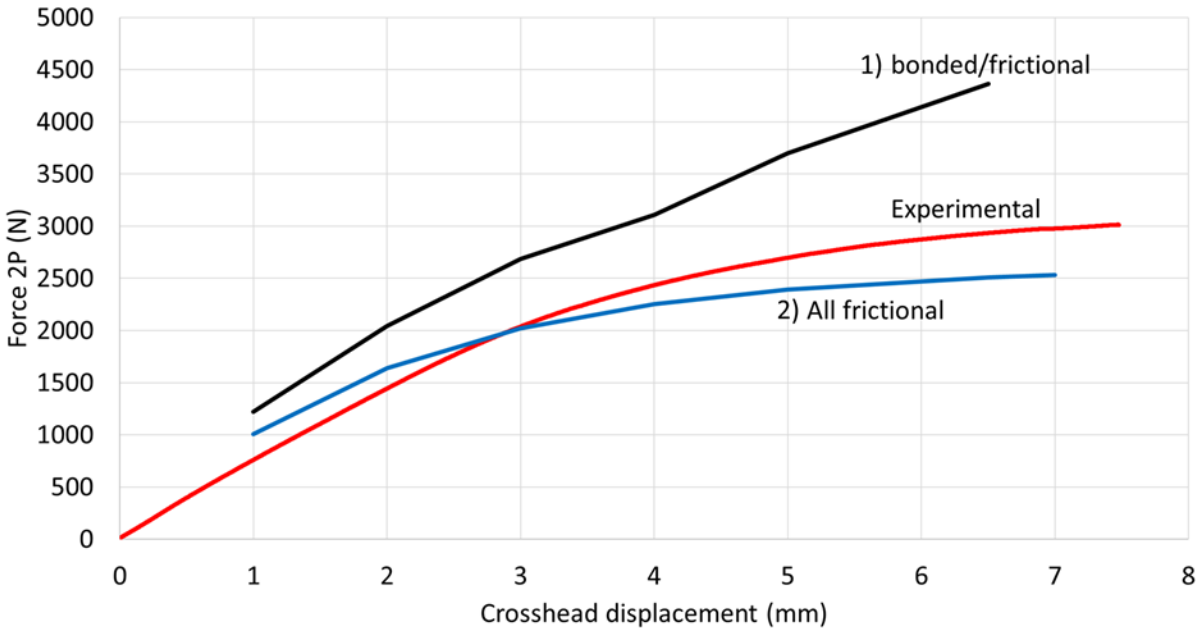

Figure 27. Predicted force vs. displacement using UO_2 material properties: (1) cladding bonded to the pellet OD with frictional cracks and (2) fully frictional (no clad to pellet bond) compared with RT test results for sample 3A1F05-1279-1432.

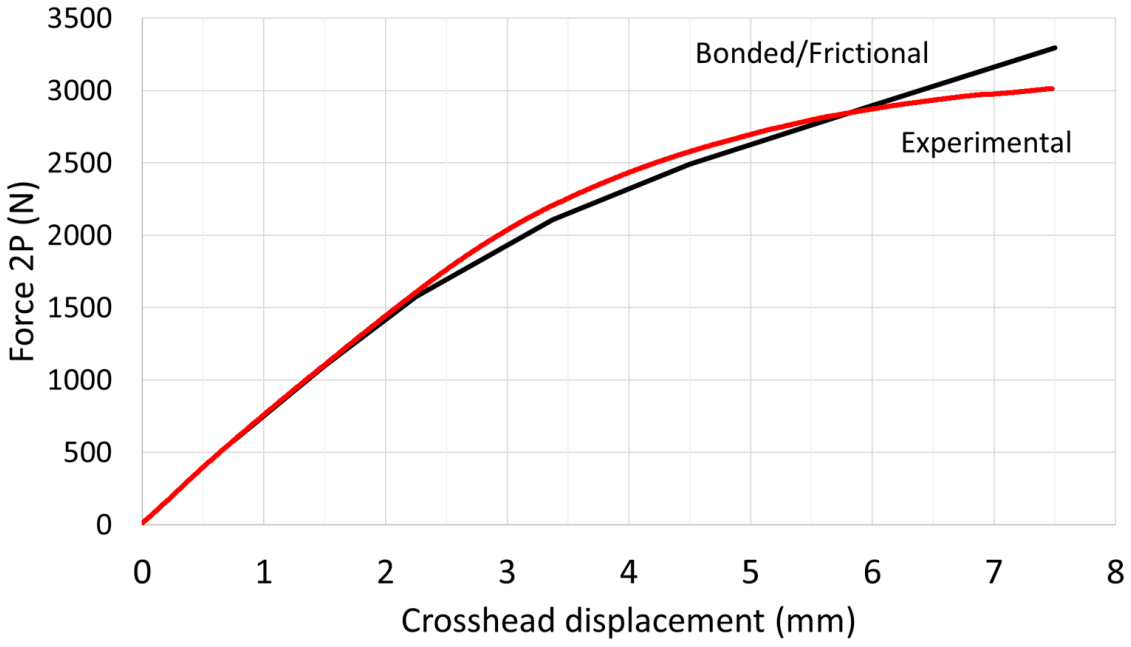

Figure 28. The finite element model can be tuned to simulate the 4PB test results if a calibrated Young's modulus is used. The calibrated Young's modulus is thought of as a surrogate for the more complex pellet cracking than is represented in the current model.

12.2 Axial Tension Testing

To perform axial tension testing (DE.08), a small amount of fuel must be dissolved from each end to allow for the insertion of a grip. The grip is used to prevent specimen crushing at the load point. Therefore, although the rough-cut segments are available, they must be further processed to prepare them for the test. RT and 200°C tests are planned.

In FY21, PNNL reported a sensitivity of the cladding-only axial tension specimens related to clamping the specimen for testing and also related to the clamp-on extensometer, as well as slippage of the specimen within the tensile test clamps [29]. ORNL has a setup for axial tension tests that is essentially identical to PNNL's setup. To determine if the sensitivity also applied to fueled specimens, ORNL tested a specimen available from a previous program (M5 clad PWR rod). Four trials were performed, and the specimen broke each time at the lowest mark associated with the serrated teeth of the upper axial tension jaws, as shown in Figure 29. An alternative method to clamp the specimens in the load frame is being investigated.

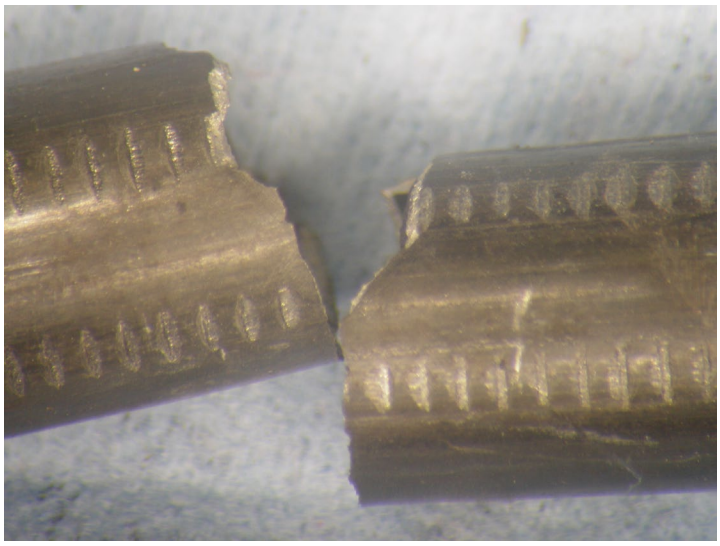

Figure 29. Axial tension failure at serrated grip notches.

In FY22, ORNL obtained a set of grips designed for use with tubing. Out-of-cell tests of the grips are promising. In-cell tests on irradiated materials will begin when the load frame is replaced. In FY23, the grips were tested out of cell, but in cell evaluation awaits the installation of the replacement load frame.

12.3 Fueled Ring Compression Testing

Argonne has developed a significant body of data on cladding hydride reorientation and the associated effects on cladding ductility using RCTs over the last decade, as summarized by Billone in 2019 [17]. Several baseline and FHT sister rod specimens were shipped to Argonne for RCTs.

ORNL's RCT (DE.10) data provide supplementary information on the load-bearing capability of intact fuel rods (cladding and pellets). Similar to RCT of cladding specimens, the fueled rod segment is loaded across its diameter, and the load to specimen failure is measured.

The RCT specimens are ~25 mm long, as shown in Figure 30, and each specimen should contain two full pellets. Five tests were completed at 200°C and 12 tests were completed at RT, and the results, which have not been corrected for machine compliance, are summarized in Table 18. The specimens typically carried load until at least one cladding fracture developed. Frequently, as shown in Figure 31, the specimen broke into two equal halves.

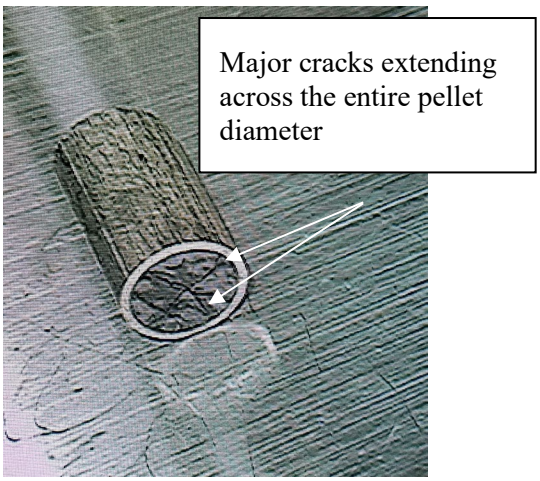

Figure 30. Typical test specimen.

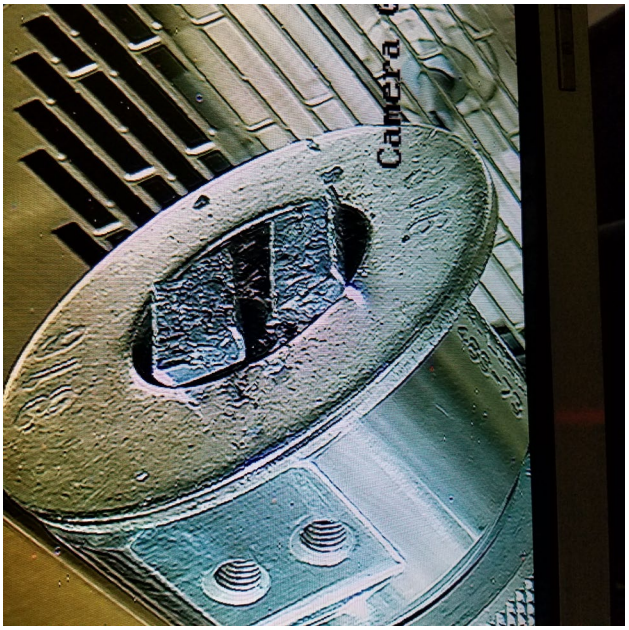

Figure 31. Typical post-RCT appearance.

The average load-bearing capability of the segments in transverse compression is 16,415 N (3,690 lb_f). The load-bearing capability does not trend with specimen average burnup, and there is not an appreciable difference in the maximum load from RT to 200°C. Cladding type also does not significantly influence the load-bearing capability, and there is no difference related to the heat treatment applied to some of the rods. The load-bearing capability of the fueled specimen is about eight times higher than that of a defueled cladding specimen (Appendix E, Figure E-21).

As the tests progressed, it became clear that fracture typically occurred at the location of one of the major diametrical pellet cracks, as illustrated in Figure 32. Usually there were two major cracks, defined as cracks extending through all or most of the pellet diameter, visible at the end of the specimen. Two specimens from F35P17 were tested with the major crack aligned along the loading path and perpendicular to the loading path. There is a difference in the results for those two samples, but unfortunately the data were not

recorded within the software for one of the tests, and only the notation on peak load in the laboratory notebook is available, which is not exact. If possible, further tests or finite element analyses should investigate load capacity as a function of pellet crack orientation.

Table 18. RCT peak load data.

Sample ID	Test temperature (°C)	Cell temperature (°C)	Cladding alloy	Heat treatment	Estimated specimen burnup (GWd/MTU)	Peak load (N)	Peak load (lbf)
30AD05 -2320-2345	25.2	25.2	M5	---	59	17,985	4,043
30AD05 -3150-3175	25.3	25.3	M5	---	56	17,000*	3,822*
30AE14-2585-2610	25.9	25.9	M5	FHT	60	17,632	3,964
30AE14 -3418-3443	25.9	25.9	M5	FHT	47	19,510	4,386
3D8E14 -2322-2347	25.1	25.1	ZIRLO	---	64	15,788	3,549
3D8E14 -3116-3141	25.1	25.1	ZIRLO	---	60	17,210	3,869
3D8E14-2347-2372	200	26.2	ZIRLO	---	64	17,752	3,991
3F9N05 -2482-2507	25.6	25.6	ZIRLO	FHT	59	17,444	3,921
3F9N05 -3350-3375	25.6	25.6	ZIRLO	FHT	50	17,049	3,833
3F9N05-3375-3400	200	25.8	ZIRLO	FHT	50	18,683	4,200
3A1F05 -3124-3149	24.8	24.8	LT Zirc-4	---	52	12,303	2,766
3A1F05 -2645-2670	24.9	24.9	LT Zirc-4	---	55	16,232	3,649
3A1F05-2670-2695	200	25.8	LT Zirc-4	---	55	12,384	2,784
F35P17-2645-2670	25.7	25.7	Zirc-4	FHT	51	12,476	2,805
F35P17-2960-2985	25.7	25.7	Zirc-4	FHT	50	12,961	2,914
F35P17-2670-2695**	200	25	Zirc-4	FHT	51	15,915	3,578
F35P17-2985-3010***	200	25.3	Zirc-4	FHT	50	12,500*	2,810*
					Maximum	20,732	4,661
					Minimum	12,303	2,766
					Average	16,415	3,690

* The data file was not saved for this test. The value is from the estimate recorded in the laboratory notebook.
** A major pellet crack as aligned with the loading direction.
*** A major pellet crack as aligned perpendicular to the loading direction.

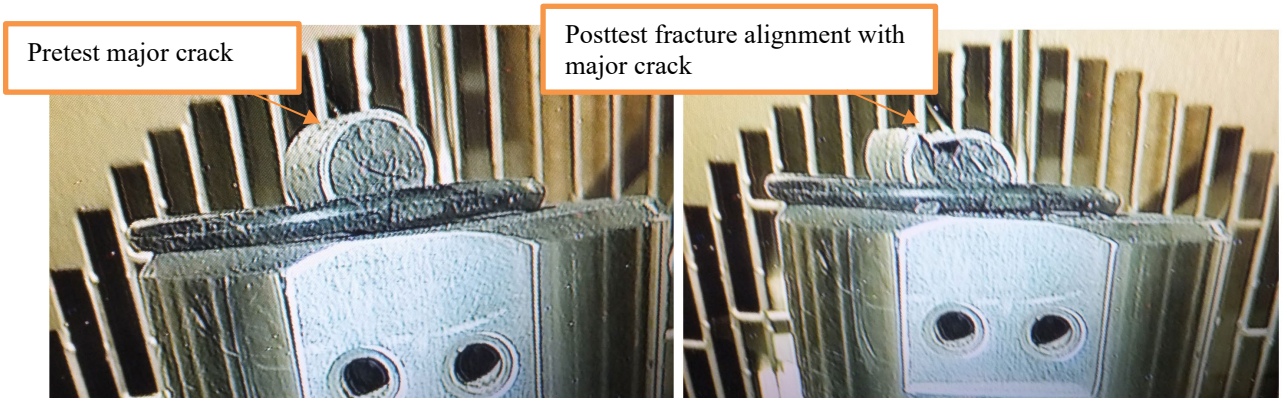

Figure 32. RCT fracture path along major pellet crack.

In FY22, to better understand the effects of cladding properties and pellet deformation characteristics, finite element modeling of the RCT was performed. The pellet was modeled as a collection of pellet fragments that are allowed to move within the cladding. The modeling examined several different pellet crack geometries and incorporated the crack structure observed for one ORNL fueled RCT, as shown in Figure

33(a) and (b). The current study highlights the difference in response depending on the crack configuration and orientation under loading, as shown in Figure 33(c) and (d).

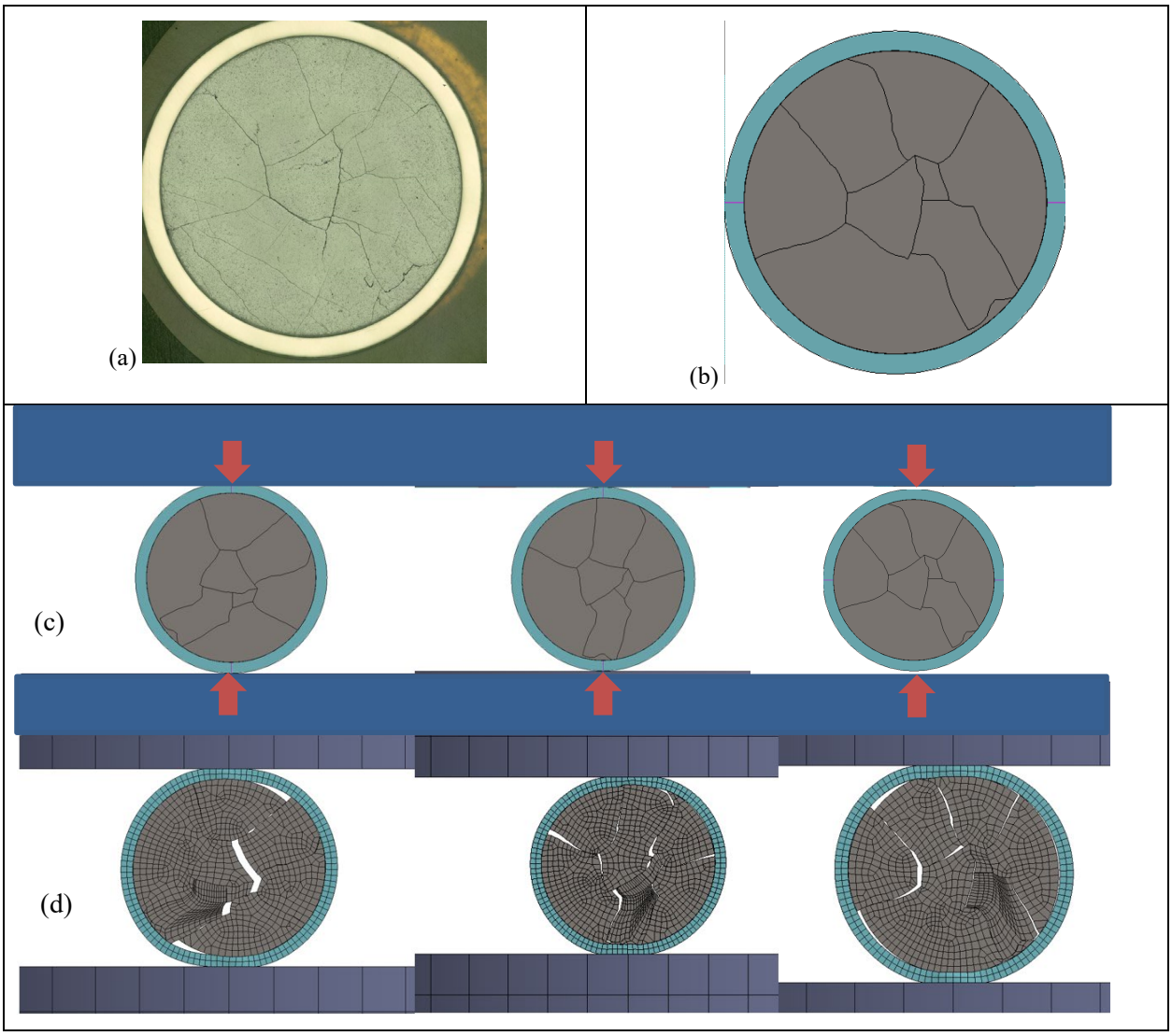

Figure 33. Fueled RCT finite element model: (a) a pretest crack pattern on a fueled RCT specimen, (b) the corresponding modeled geometry, (c) varied orientation of the crack pattern under RCT load (as indicated by the red arrows), and (d) the response of the cracked pellets.

The reaction loads from the models, which correspond to the load recorded during actual fueled RCT, were evaluated for the varied crack patterns and orientations examined and ranged from 49.6 to 80.2 kN for the actual pellet crack model. The reaction loads generated using the cracked pellet geometry are much larger than the measured RCT data. One known issue is that the cracks in real pellets are not continuous through the length of the pellet, as are modeled here. A more simplified wedge model incorporates more cracks which allow the pellet fragments to move more within the cladding, and these models are nearer the loads recorded in the fueled RCT testing. However, the inability of the model to capture the non-linear load-displacement profile suggests it may be necessary to model additional pellet cracking as the load increases, as observed during the test, and because of this, the initial crack configuration may not be a key parameter in the model. Future models will investigate this more by incorporating more detailed authentic pellet crack

patterns with segmentation along the pellet length. Appendix E, Section E-5.4, provides a more detailed discussion of the finite element modeling.

Work in FY23 explored the complex pellet interactions including sliding and rigid body motion using ANSYS LS-DYNA, a widely utilized finite element analysis software package designed specifically for simulating intricate, nonlinear, dynamic phenomena in materials, structures, and systems. Through the use of the explicit dynamics solver and parametric evaluations of pellet material properties, significant improvement in the model's ability to match experimentally-observed behavior was realized. This work informs the higher order models used in simulating transportation, supports the evaluation of the tested conditions, and is intended to allow for extrapolation to other untested conditions.

12.4 Microhardness Tests

Microhardness testing (DE.09) equipment is available at both the Low Activation Materials Development and Analysis (LAMDA) laboratory and the IFEL at ORNL. Vickers microhardness tests at LAMDA were conducted at RT on cladding-only specimens using a Buehler Wilson VH3100 microhardness tester. The tester has both Vickers and Knoop indentation capability with the maximum load capacity of 10 kg. Prior to microhardness examination of the sample, the equipment was tested using a Sun-Tec certified calibrated sample having a known HV value. The equipment at IFEL will be used for fueled specimen tests at RT and at 200°C.

In FY21, microhardness tests were performed on one defueled, polished, and lightly etched sample prepared from segment F35P17-2735-2754 (heat-treated Zirc-4 cladding). Visual inspection of the microhardness indents showed crisp uniform indent edges, the diagonal lengths are equal, and the diagonal corners can be easily distinguished. Each quadrant of the cladding was indented across its thickness, and a fifth test was performed at a location where extensive waterside oxide spalling occurred, as discussed in Appendix E. The measured HV increased from cladding ID to OD across the cladding thickness and ranged from 251 ± 9 to 298 ± 11 HV. The oxide layer was found to be significantly harder than the base cladding, at an average measured HV of 947 ± 67.

In FY22, 8 additional cladding elevations were tested (28 indentations per elevation, 7 indentions per quadrant, for a total of 224 indentions) at RT. As shown in Figure 34, some indentions were on top of hydride precipitates and others were not. The inclusion of the hydrides generally resulted in a higher HV.

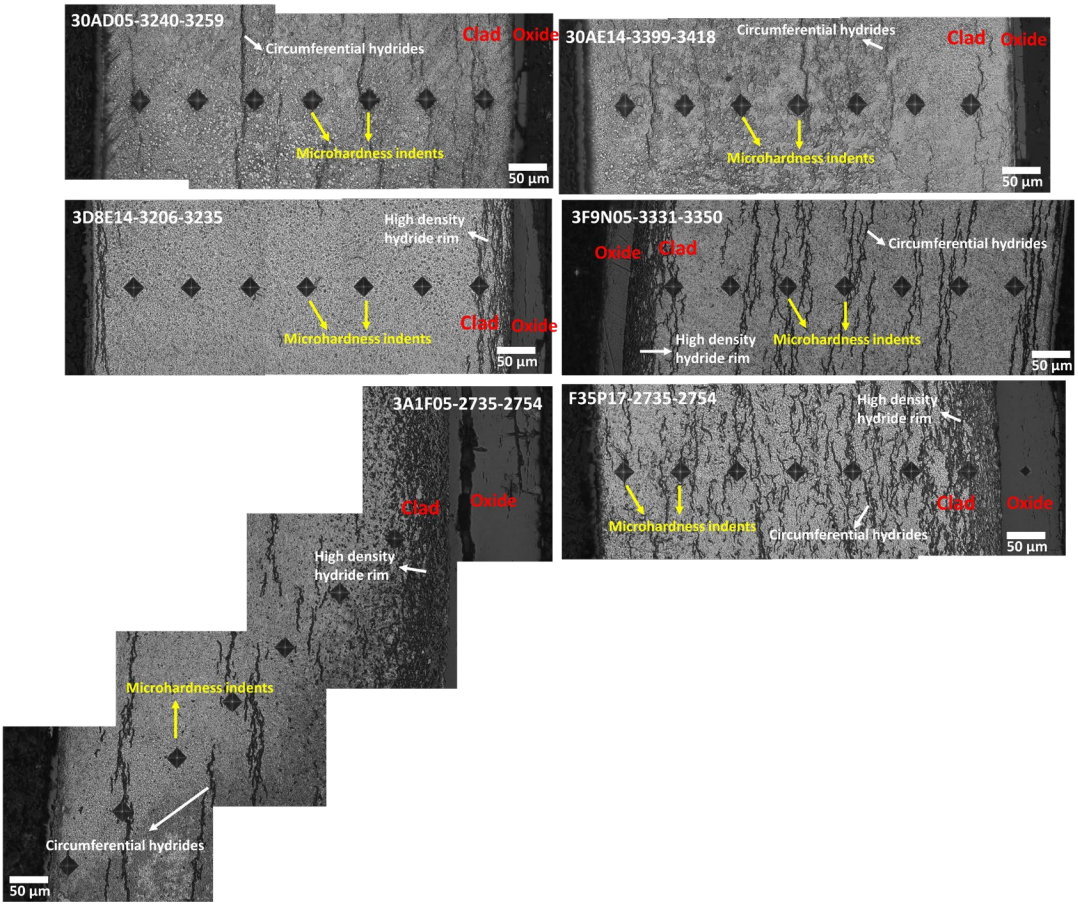

Figure 34. Summary view of microhardness indentions for each rod tested.

For ZIRLO, Zirc-4, and LT Zirc-4, most elevations had an increasing HV from cladding ID to OD of >10 HV that may be related to a higher density of hydride precipitates at the OD.

As shown in Figure 35, M5 has a lower hardness than the ZIRLO, Zirc-4, and LT Zirc-4 samples that is attributed to M5's recrystallized-annealed (RXA) microstructure, as opposed to the other alloys, which are cold-worked and stress-relief annealed (CWSRA).

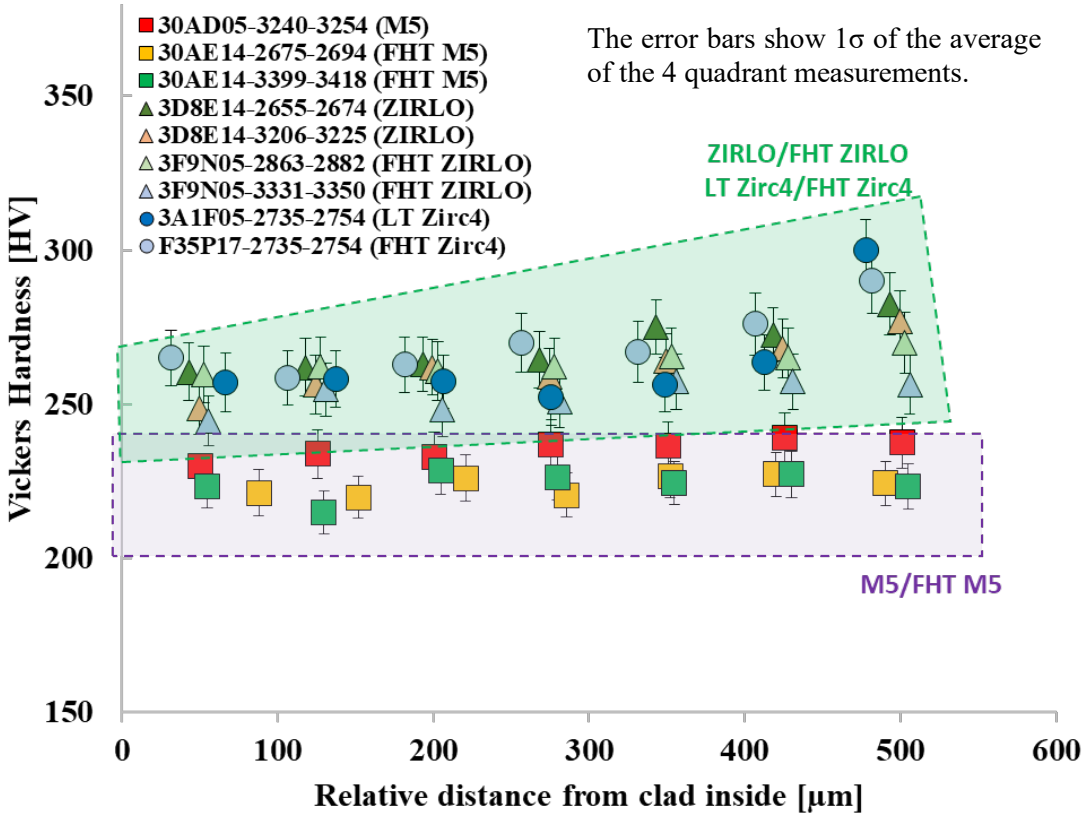

Figure 35. HV from cladding ID to OD by cladding alloy type.

A plot of the CWSRA HV as a function of estimated local burnup (Figure 36) as a surrogate for fluence seems to indicate a strong correlation, with an increase of ~7 % in HV for a corresponding increase of ~15 GWd/MTU in burnup. The same cannot be said for M5, but only three data points are available.

Another interpretation of the HV data could be that the FHT resulted in a hardness reduction. For the M5 cladding, the microhardness testing showed a pronounced reduction in cladding hardness after FHT. The difference is not as obvious for the ZIRLO/FHT ZIRLO and LT-Zirc4/FHT Zirc-4 cladding samples, suggesting that the impact of heat treatment on hardness is influenced by the cladding processing (CWSRA, RXA).

The microhardness testing and results are described in detail in Appendix E, Section E-4. Additional tests will be completed at other elevations and at 200ºC.

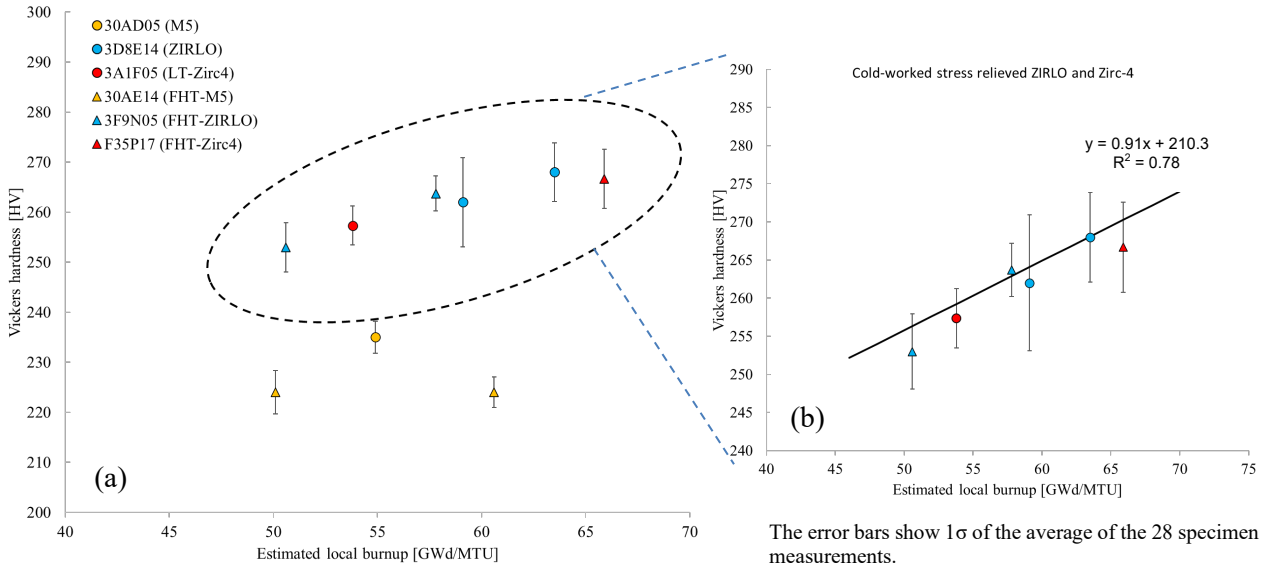

The error bars show 1σ of the average of the 28 specimen measurements.

Figure 36. Comparison of sister rod cladding Vickers hardness vs. estimated local burnup (cold-worked stress-relieved cladding samples circled with a dashed line (a); corresponding data shown as the inset (b).

12.5 Burst Tests

In FY21, ORNL investigated its existing equipment for use in burst testing fueled specimens. One goal of the burst tests is to capture aerosols released in the burst, and for this purpose, a gas must be used to pressurize the test specimen. Also, the test is to be conducted at RT. Given these criteria, the prior existing equipment in the hot cell, such as ORNL's Severe Accident Test Station, are not capable of reaching the necessary pressure.

In FY22, ORNL developed a pressurization system; however, pressures high enough to induce burst at RT have not been possible with this system. Further development is required and will continue in FY23.

In FY23, the program reduced the priority of fueled burst testing, as there is no anticipated storage or transportation scenario where fuel rod burst can occur. This work has been deferred.

13. Aerosol Collection Testing

To investigate the release of aerosolized radioactive material from an HBU fuel rod during fracture (10 μm aerodynamic equivalent diameter [AED] or less is generally considered to be the upper limit of human respirability [18]), an aerosol collection capability (AERO) is being developed for deployment on the CIRFT equipment (DE.05) and Instron load frame, which is used for DE.07, DE.08, and DE.10. Two different collection configurations—one for CIRFT and one for the load frame—will be developed, but the aerosol collection media and approach are expected to be the same. One test was completed in FY22 and a second was completed in FY23. Four more tests with unpressurized specimens are expected to be completed in FY24. Tests using pressurized segments are planned to follow the unpressurized tests.

13.1 Apparatus and Approach

Inertial impaction is the method used to collect particulates released from the sister rod specimen as it is fractured during testing. Impactors are devices that separate the particulates based on size. In the impactor, air containing the particulates to be sampled is accelerated through an orifice toward a collection filter placed at a fixed distance below an orifice. The collection filter forces the air stream to change direction abruptly, and particles that are large enough have enough inertia to escape the air stream and are collected on the filter. Particles that are smaller follow the air stream and remain suspended, moving on to the next stage of the impactor.

The *cut point* is the aerodynamic size (AED) of particles that are collected by the sampler with 50% efficiency. Ideally, all particles greater than a certain size are collected on the filter, and all particles that are smaller pass through. However, because impactors act on aerodynamic variables and do not perform like a mechanical barrier, such as a sieve, the collection efficiency is not 100%. Based on the orifice diameter and flow rate used, collection efficiency increases for particles larger than the cut point and decreases for smaller particles. For a 4 μm AED cut point, 100% of 10 μm AED particles and 50% of 4 μm AED particles are removed from the air stream and deposited on the filter.

A photo of the collection equipment is shown in Figure 37 and is further detailed in Appendix I. The collection enclosure is 3D printed plastic that can be rinsed, dissolved, or imaged. In FY22, the enclosure design has been modified to include a viewing window that will facilitate high speed images of the fracture and dust release. In FY23, several options for lighting and high-speed imaging were explored. The most viable option identified is lighting using a high lumen flashlight, in the hot cell, but external to the enclosure, through the enclosure window. Additionally, an anti-static coating was tested on the interior surfaces of the enclosure to facilitate rinsing of the collected dust-type materials post-test. The coating was found to be effective and will be used in future tests. Sampling tubing fixed in the bottom of the enclosure allows direct access to the location where the material is expected to be expelled from the specimen during 4PB fracture. The set up includes a commercially available four stage Sioutas cascade impactor (nominal particle collection cut points up to 2.5 μm AED). Because it is necessary to sample the range of respirable aerosol particles (up to 10 μm AED), the Sioutas cascade impactor was modified to include additional stages for aerosol collection up to nominally 14 μm AED. Table 19 summarizes the nominal collection cut points and corresponding physical UO_2 particle diameters of the modified cascade. A detailed discussion of the design and verification testing is provided in Appendix I. One test was performed in FY22 and a second test was performed in FY23; both are discussed in detail in Appendix I.

In FY22, the potential for dual sampling was investigated and is considered viable. The dual sampling approach will allow for dedicated SEM specimens, since there is concern that aerosol particulate could be lost during vacuum pumping of the SEM system. Further physical out-of-cell tests were completed in FY23 and they continue to support the case for dual sampling to enable SEM imaging while securing a specimen for isotopic examination. One test using dual sampling is planned for FY24.

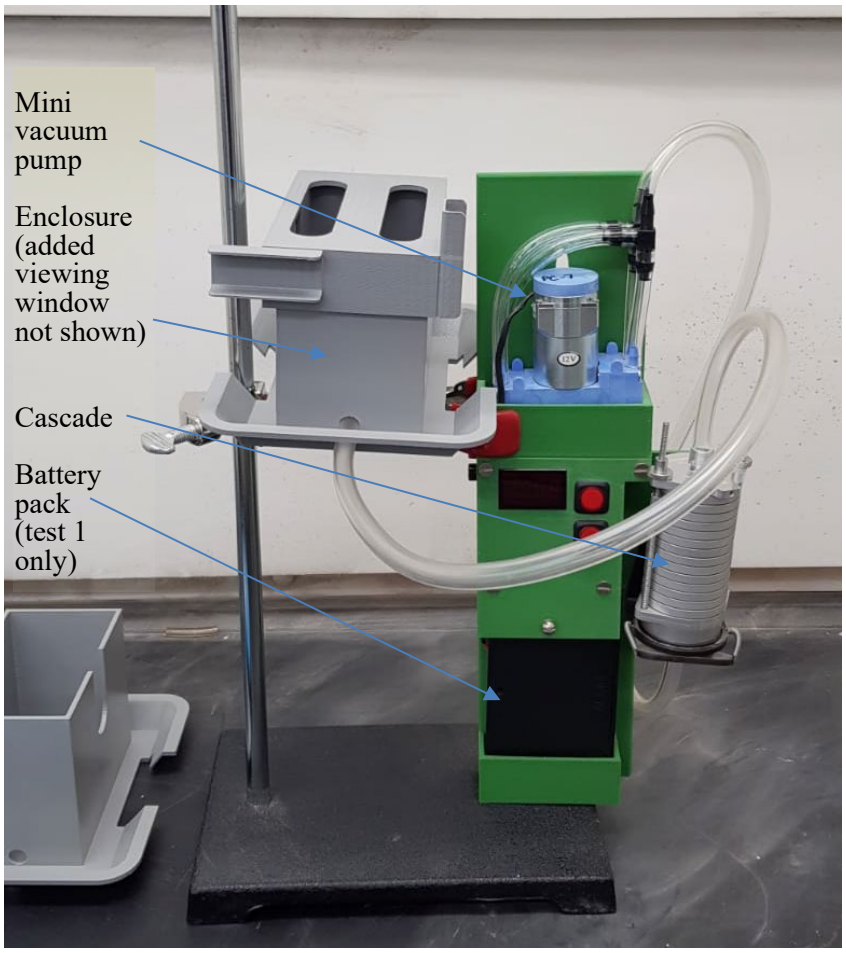

Figure 37. Aerosol collection enclosure with the sampling card and modified 7-stage Sioutas cascade.

Table 19. Seven-stage modified Sioutas cascade nominal cut points at 7 LPM based on design orifice dimensions with the corresponding UO_2 particle diameter.

	Stage MA	Stage MB	Stage MC	Stage PA	Stage PB	Stage PC	Stage PD
UO_2 Physical mean (µm)	4.2	2.3	1. 8	1.6	0.8	0.5	0.4
AED mean diameter (µm)	**14.0**	**7.5**	**5.9**	**4.5**	**2.7**	**1.7**	**1.2**

The first aerosol collection test was completed using an Instron load frame, as described in Section 12 and Appendix E. Unfortunately, the electronic components within the Instron load frame have been damaged by radiation which rendered it inoperable in early FY22. To provide 4PB aerosol collection capability

within a limited space and accelerated timeframe, ORNL designed and fabricated the *MiniMight* load frame. The frame supports the aerosol collection system and includes an LVDT to determine displacement during bending, a load cell for accurate in situ load measurements, and limit switches for end of travel system protection. The 4PB fixture is the same as that used on the Instron system, except the loading distances are modified slightly to accommodate Swagelok fittings used on the ends of pressurized segments.

The second aerosol collection test utilized MiniMight, as shown in Figure 39. The remainder of the aerosol collection tests are expected to be performed using MiniMight.

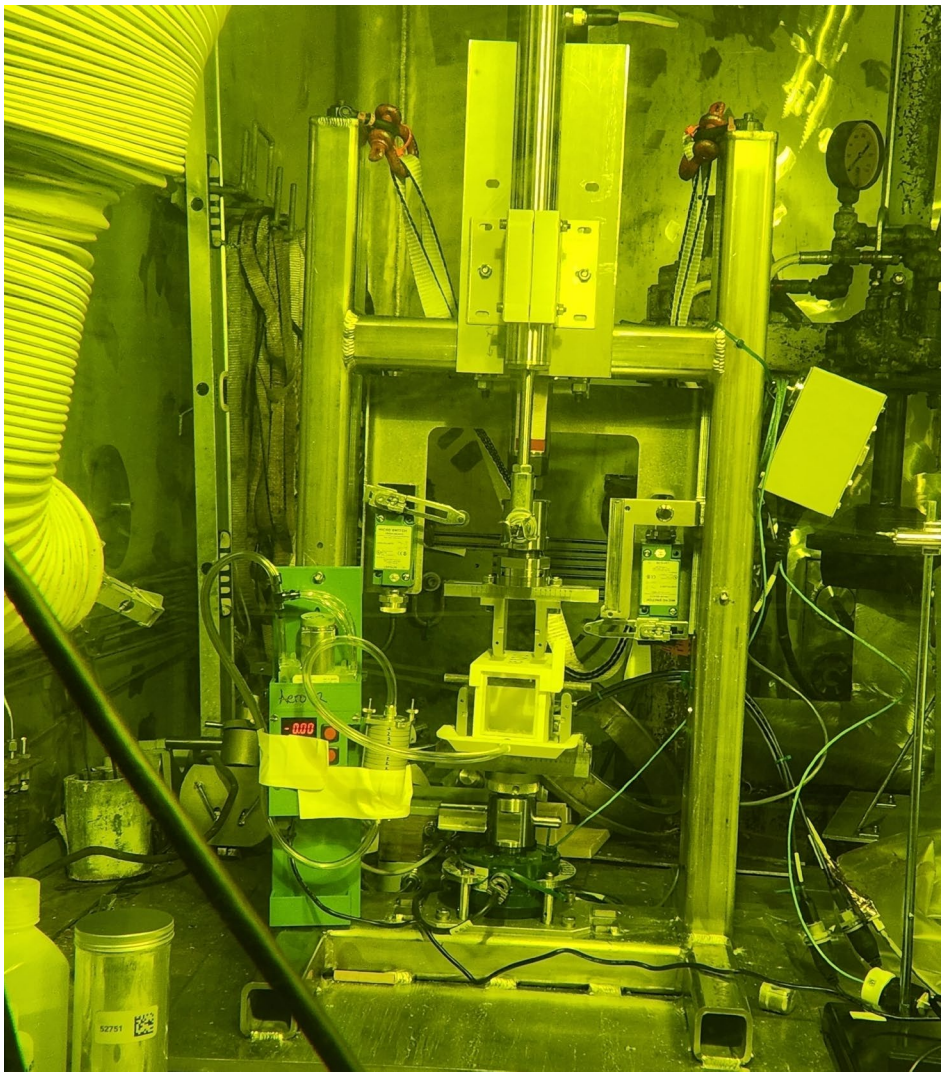

Figure 38. The MiniMight installed in the IFEL hot cell and set up for the second aerosol collection test.

13.2 Test AERO-1 – Unpressurized ZIRLO-clad specimen

One test using the modified Sioutas Cascade (7-stages) was completed in February 2021 with an unpressurized ZIRLO-clad specimen (3D8E14-2810-2963) having an estimated local burnup of 63 GWd/MTU and an average waterside cladding oxide thickness of 41 μm. Figure 40 provides post-test images of rod segment that was broken in 4PB. The rod broke in the body of a pellet, with a typical amount of fuel debris released (see Section 12.1) and spalling of the waterside oxide is evident at the maximum stress locations. The coarse SNF debris collected in the enclosure was poured out of the enclosure and weighed following the test. The mass of the coarse debris was 0.5 g, and this is the same as the mass loss from the specimen post-test, within the capabilities of the scale used at ±0.1 g. There was also dust collected on the sides and lid of the enclosure. This was collected and the total mass of the dust-sized debris left in the enclosure was 4,615.85 μg.

Dust-sized debris that was drawn into the cascade was deposited onto the various stages according to its AED. A view of the collection media prior to chemical dissolution is shown in Figure 41. Some particles also deposited onto the orifice plate itself, and this mass is attributed to the stage where it was collected. Table 20 summarizes the mass of material collected from the various surfaces in the flow path, including the collection enclosure, the connecting tubing, the cascade's collection stages, and the orifice plates. The total mass collected in the cascade on each stage along with the mass of each isotope measured is shown in Figure 42.

Within the error of the mass measurement technique (inductively coupled plasma mass spectroscopy, see Appendix I), it was observed that the enclosure and its lid yielded the maximum mass of dust-sized particulate—15 times more than that collected in the cascade impactor. The lowest mass of dust particulate was obtained from the tubing that connected the enclosure and the cascade. The AED of the particles adhered to the enclosure and tubing is unknown, but ongoing computational fluid dynamics simulations (see Appendix I) indicate particles smaller than 10 μm are pulled into the cascade sampler.

The initial analysis of the dust particulate collected in FY21 indicated that the total mass of SNF typically released as dust particulate during rod fracture in bending is less than 0.0046 g, with 494 μg collected in the cascade within the respirable AED range. The initial analysis was completed by dissolution of the collected materials and ICP-MS measurement. However, it was suspected that additional materials may have been embedded within the collection media, so the collection tabs were ashed and reanalyzed for the isotopes of interest, as described in Appendix I Section I-6.2.2. The additional isotopic mass from the ashed collection tabs was well below 2%, and in all but one case, less than 0.5% of the mass measured in the dissolution analysis.

The airborne release fraction and respirable fractions measured in the first test were calculated based on the mass of the SNF in the 6 in. rod length tested (~84.58 g) and a generic isotopic source term for isotopes that are solid at RT based on 4% ^{235}U enrichment at 60 GWd/MTU burnup accumulated over 1,150 days of operating and cooled for 10 years. Based on this approach and excluding the cladding materials, the amount of isotopic material at risk (as calculated based on [25]) for release as aerosolized particles is near 80 g.

The total airborne release fraction is calculated as 4,615.85 ± 388.35 μg /80 g = 5.8E-05.± 4.96E-06. Conservatively assuming all particles collected in the cascade are respirable, the respirable fraction is calculated as the fraction of airborne particles that are in the respirable range, 494 ± 46 μg /4,615.85 μg = 0.107 ± 0.010. As discussed in Appendix I, The respirable fraction tends to trend well with the source concentration, as shown in Figure 42, except for ^{139}La, ^{140}Ce, and ^{242m}Am. The histogram of the frequency of release fractions (isotope mass captured in the cascade impactor/isotope mass available for release from the source pellets) indicates that these same isotopes, along with ^{233}U and ^{232}Th, appear to have higher than typical release fractions.

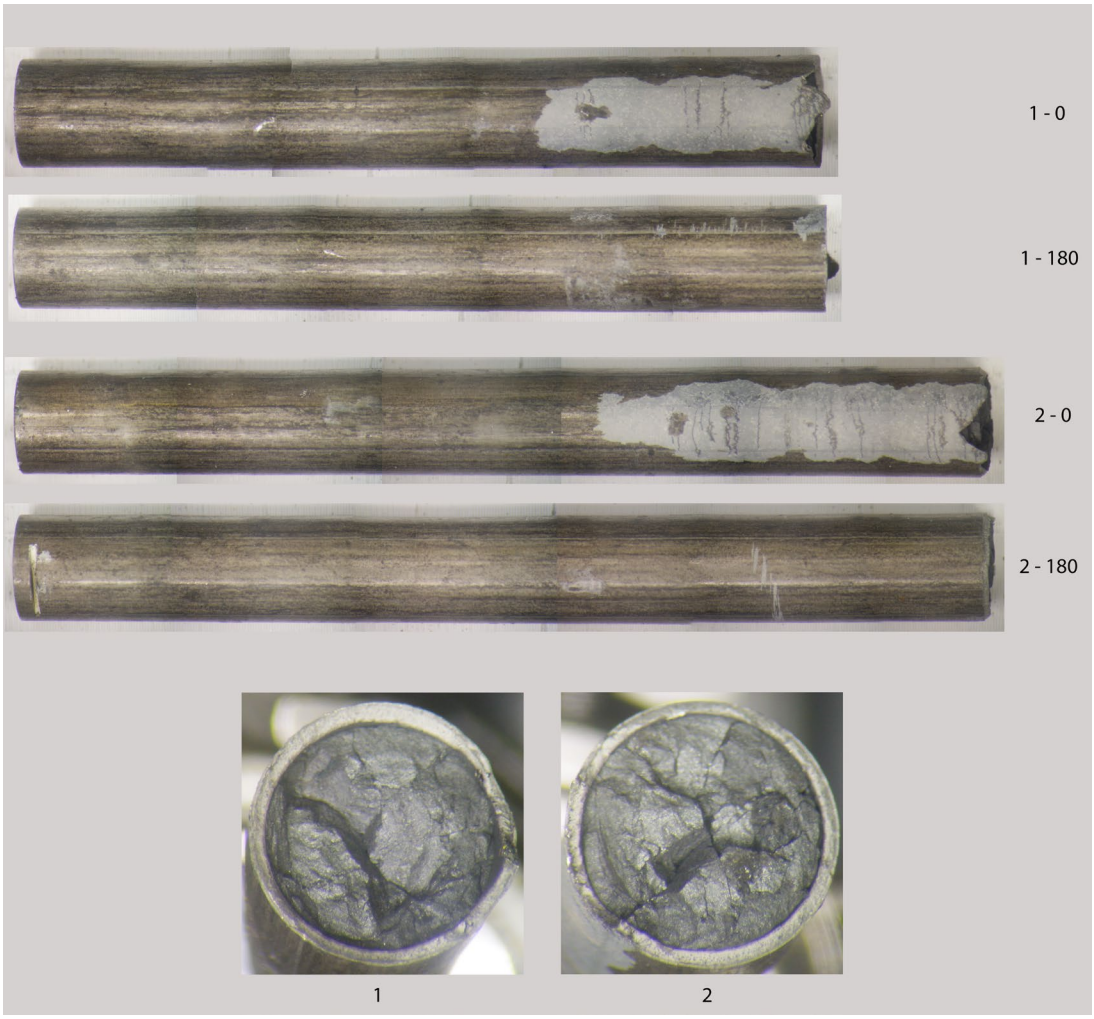

Figure 39. Image of the outer surfaces of the test rod following the aerosol collection 4PB test. The fracture occurred in the body of a pellet, producing coarse debris consistent with ORNL's past 4PB experience.

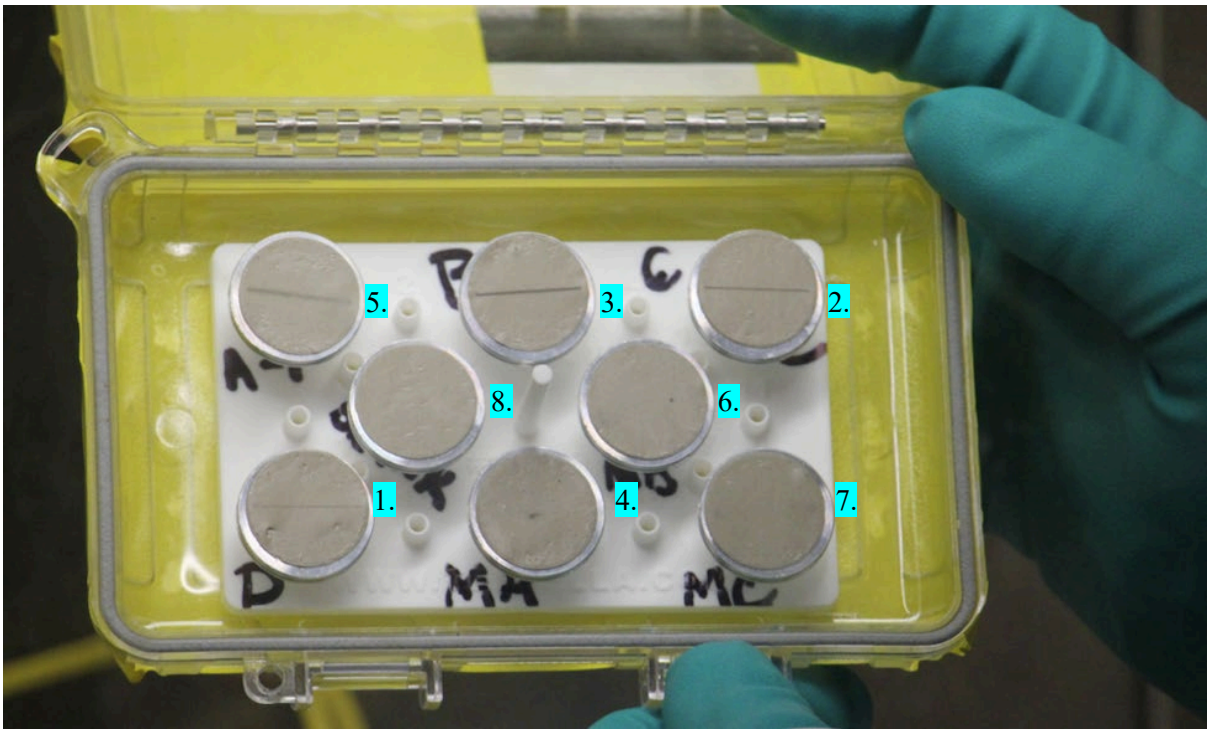

Figure 40. SEM tabs showing the aerosol collected in the experiment. The thin lines on the tabs are the collected aerosol particles from SNF: (1) MA-1, (2) MB-1, (3) MC-1, (4) A-1, (5) B-1, (6) C-1, (7) D-1, (8) blank substrate for contamination tracking.

Table 20. Collected mass total for each component with surfaces in the flow path.

Stage	Total, µg	Uncertainty, µg.	Relative error (%)
MA-1, AED ~14.0 µm	235.4	22.4	9.5
MB-1, AED, ~7.5 µm	139.6	13.3	9.5
MC-1, AED ~5.9 µm	45.8	4.4	9.6
A-1, AED ~4.5 µm	31.4	2.8	8.9
B-1, AED ~ 2.7 µm	27.7	2.5	9.1
C-1, AED ~1.7 µm	10.9	1.0	8.8
D-1, AED ~ 1.2 µm	3.52	0.3	8.3
Enclosure Lid	85.5	6.6	7.7
Enclosure Base	3988.7	332.6	8.3
Tubing	47.2	3.3	7.0
Total mass collected as dust-type particulate	4615.7	388.4	8.4

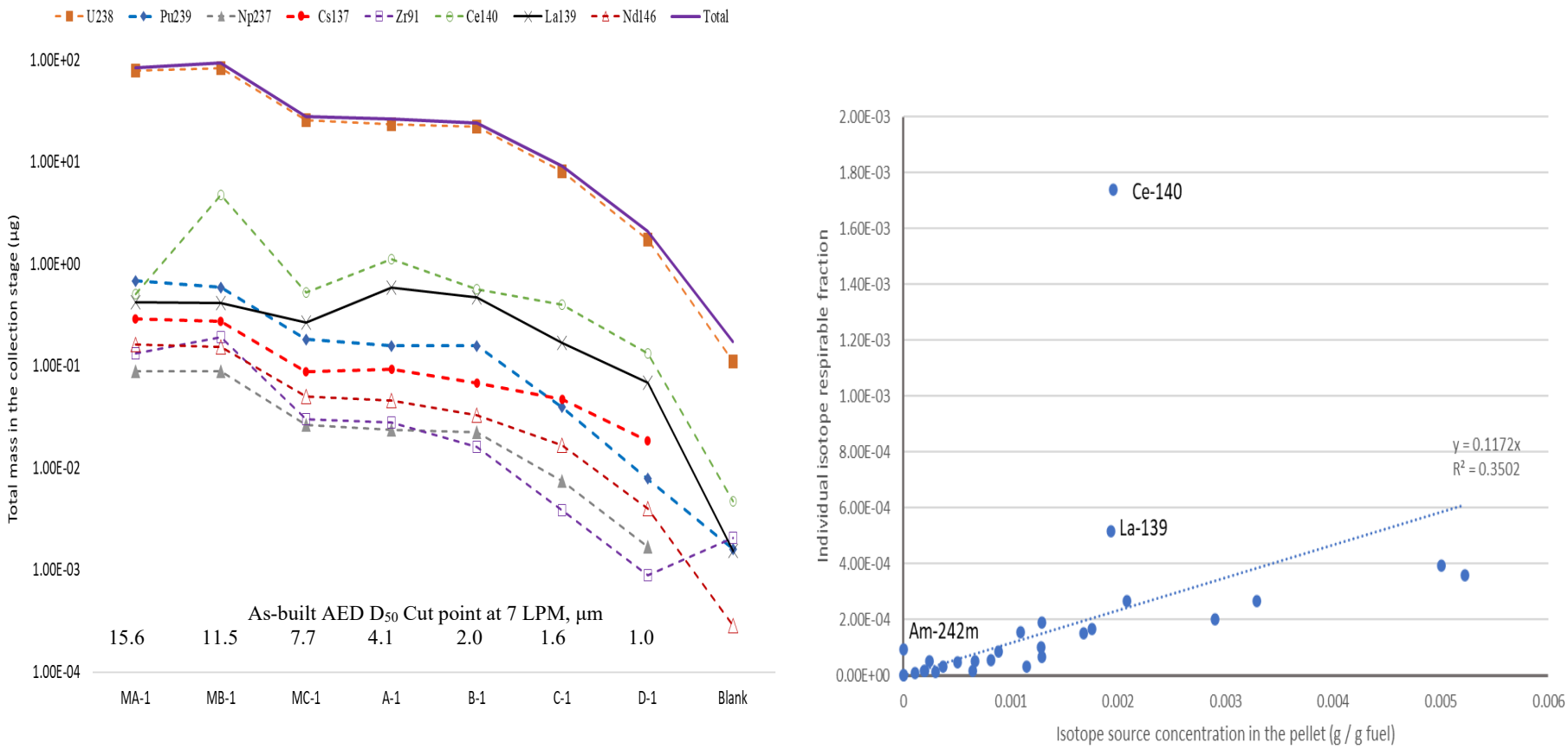

Figure 41. (left) Total mass and mass of measured isotopes deposited on the collection media by stage and (right) the source rod isotopic concentration vs. the measured isotopic concentration.

13.3 Test AERO-2 – Unpressurized LT Zirc-4-clad specimen

In September 2023, LT Zirc-4-clad specimen 3A1F05-2402-2555 was broken in 4PB, and aerosol collection was completed using the modified Sioutas cascade (7 stages). The specimen has an estimated local burnup of 55 GWd/MTU and a thick waterside cladding oxide thickness of 117 µm (local average) with widespread spalling. The specimen weighed 98.4 g pre-test. The post-test images clearly show that the fracture occurred at a pellet-pellet interface as opposed to in the body of a pellet. The right segment fragment impacted the enclosure lid during the fracture event, and it was lifted briefly from the enclosure base but reseated after the impact. The left fragment was ejected with considerable energy and was retrieved approximately 1 ft from the test frame.

The cascade impactor was disassembled and sent for analysis, as shown in Figure 43. The results are expected in early FY24.

Figure 42. (top) Disassembly of the cascade impactor in a glove box and (bottom) three of the collected specimens with their orifice plates.

14. Leach Testing of Waste Specimens

In FY21, ORNL hosted a doctoral candidate who worked with ORNL staff to perform leach tests of waste segments harvested from fractured CIRFT specimens using deionized (DI) water. The CIRFT testing leaves behind bulk fuel segments that provide ideal candidates for leaching experiments. These studies are of interest to the sister rod program because some fuel rods that will be placed into dry storage and transported may have unidentified cladding cracks and may contain residual water [19]. The movement of fission products from the pellets to water provides an additional source of radioactive materials that could be available for release via the water or through the corrosion of the fuel pellets. This section provides a brief description of the tests and results. Appendix J includes a complete discussion of the tests, analysis methods, and results. Note that in FY22, an error was found in the sample mass calculation, and the results here and in Appendix J have been updated.

One heat-treated specimen and its corresponding baseline specimen were selected for comparison. Table 21 lists the sample information.

Table 21. Selected leach samples.

Specimen ID (Parent rod – lower elevation – upper elevation in mm)	Cladding type	Heat treatment	CIRFT specimen ID	Leach specimen IDs	Estimated local burnup (GWd/MTU)
30AD05-2050-2203	M5®	No	DE50008	NHT-C, NHT-A1, NHT-A2	59.2
30AE14-2850-3003	M5®	Yes	DE50009	FHT-C, FHT-A1, FHT-A2	59.7

Bulk material from the post-CIRFT (fractured) specimens was cut from the CIRFT dogbone and then sectioned both axially and circumferentially to produce three samples from a dogbone: one ~2 mm segment cut circumferentially and two halves of a ~20 mm long axially cut segment (Figure 44) to produce varying exposed fuel surface areas. The fuel remained intact within the cladding. Thus, a total of six samples were used in this study. Each specimen was placed into a separate flask with 100 ml of DI water after being rinsed with DI water to remove any cutting debris.

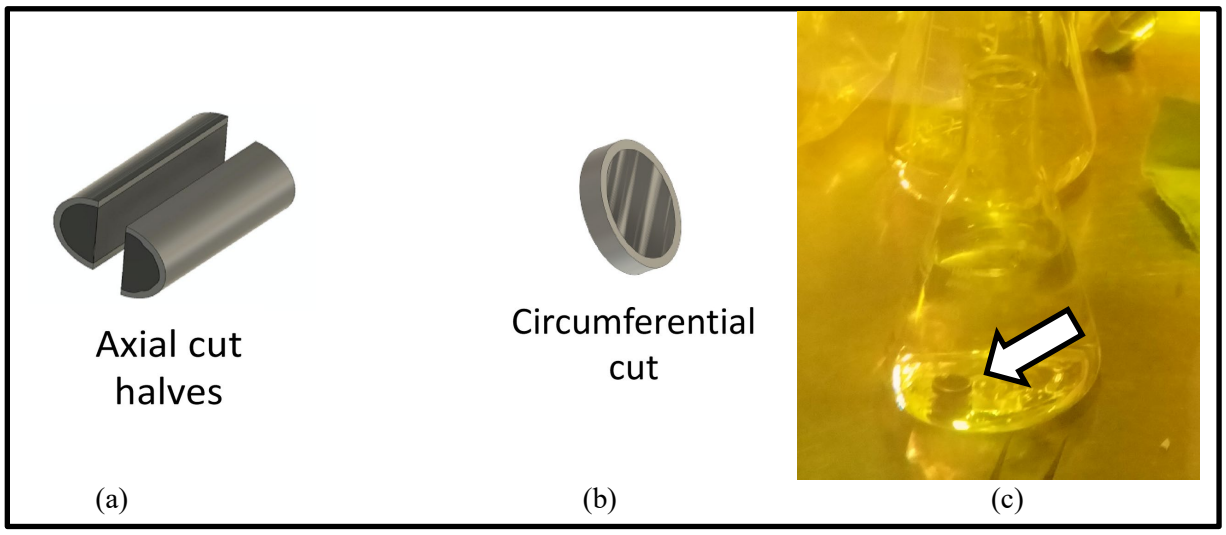

Figure 43. Schematic of the (a) axially and (b) circumferentially cut fuel samples and (c) a circumferential sample in DI water for testing.

A flask with the same amount of DI water but without a sample was used as a control to monitor for potential contamination. The control flask was kept open to the cell atmosphere for the time it took to place the sample in the flask.

Periodically, 1.5 ml of solution was removed from each flask for analysis. Samples were taken after 30, 60, 90 and 128 days of leaching. The samples were analyzed using ICP-MS and gamma spectroscopy. Figure 45 graphs the combined fractional release rates (FRRs) of the lanthanide fission products released during each sampling period of the experiment for the baseline and heat-treated specimens. FRRs are calculated by normalizing the fractional inventory in aqueous phase (FIAP) values to the sampling time period. Among the rare earth elements, ^{139}La was observed to have the maximum cumulative release rates in all samples across all sampling periods. This was followed by ^{153}Eu, ^{147}Sm, and ^{145}Nd, which showed comparable release rates. ^{141}Pr had a slightly lower release rate than isotopes of Eu, Sm, and Nd, and the slowest rate of release was seen from ^{140}Ce and ^{156}Gd, which exhibited comparable rates.

The gamma spectroscopy data from the leachate indicates that there is a steady release of ^{137} Cs in each sampling period and the rate of release consistently reduces as a function of time, which agrees with the ICP-MS trend. The low activities observed in the circumferential specimens as compared to the axial specimens are due to the lower initial ^{137}Cs source term present in the specimens and are not attributed to the difference in exposed surface area.

Following the leach, the samples were mounted for metallography. The images were analyzed before and after polishing. The pre-polished images seem to indicate that the DI water may have been able to move through the depth of the samples via pellet cracks and via the pellet-cladding gap, even though the HBU rods have extensive pellet-cladding interaction and closed gaps. Two samples, NHT-C and NHT-A1, were polished and re-imaged. The images revealed that the PCI layer is populated by a large number of openings having an average size of 5–10 μm^2 and it was concluded that the openings and defects in the PCI layer run deeper into the sample, with possible networks of connected defects, allowing the DI water to penetrate deeper into the specimen. The main conclusions drawn from this study are listed below:

- SNF dissolution follows a trend in which there is an initial instant release of radioisotopes of Cs, Sr, Mo, and Np, followed by a gradual matrix dissolution of U, Pu, Eu, Nd, La, Pr, Sm, and Gd. The leaching of less volatile isotopes of Ru, Rh, and Ce depend on matrix dissolution.
- There is a good agreement between ICP-MS and gamma spectroscopy in the leaching analysis of gamma-emitting isotopes such as ^{137}Cs.
- Circumferential sample NHT-C has the highest leached concentration of radioisotopes of all samples. Although the circumferential samples started out with lesser surface area of fuel exposed to the water as compared to the other samples, visual and metallographic observations indicate cracks running through the sample and opening of the pellet-clad interaction layers. This makes it more vulnerable to leaching because of the higher quantity of grain boundaries and pores in this region.
- There was no difference identified related to the heat-treatment applied to the FHT specimens tested.

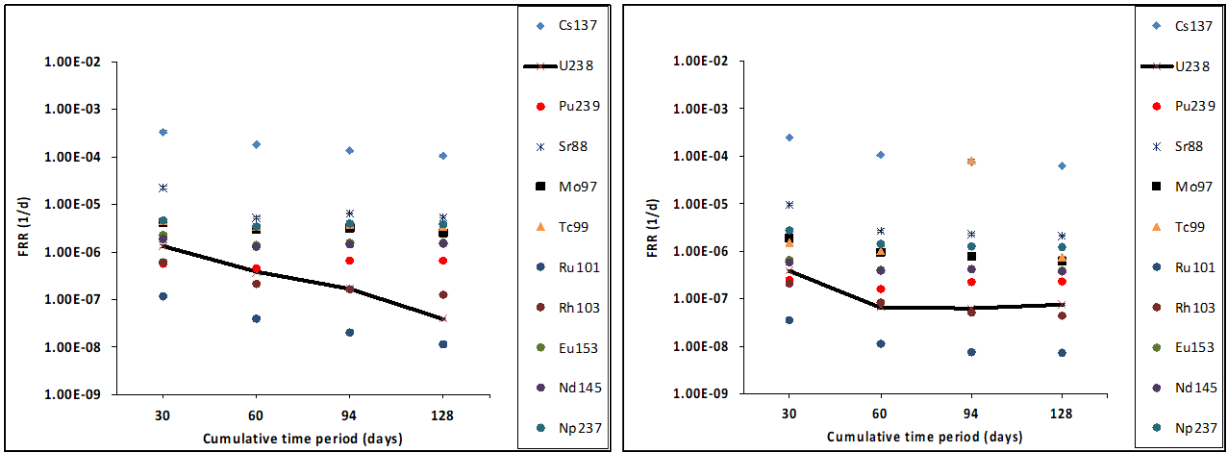

A) Combined FRR (in log scale) of NHT-C

B) Combined FRR (in log scale) of NHT-A1

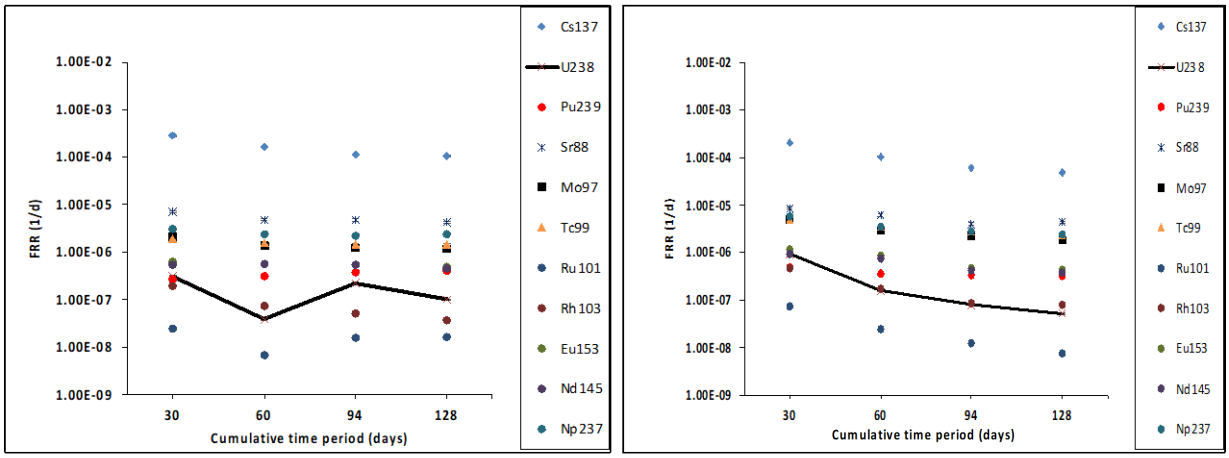

C) Combined FRR (in log scale) of NHT-A2

D) Combined FRR (in log scale) of FHT-C

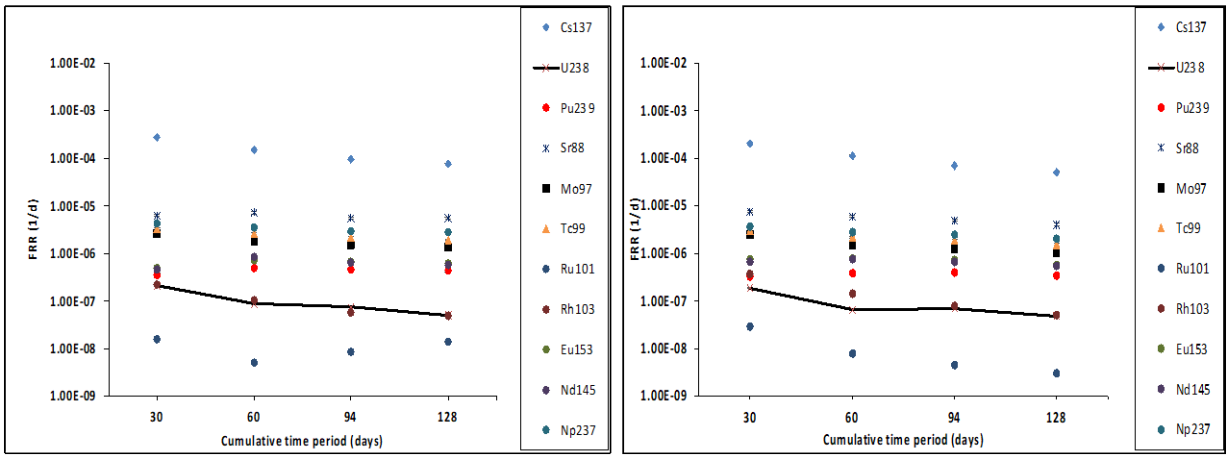

E) Combined FRR (in log scale) of FHT-A1

F) Combined FRR (in log scale) of FHT-A2

Figure 44. Combined FRRs for the baseline and FHT specimens in DI water.

This page is intentionally blank.

15. Disposal of Test Waste

During destructive testing of the sibling pins, the tested SNF sample material eventually becomes no longer useful for R&D purposes due to its reduced size and/or changes in its physical and mechanical properties. At that point the material is designated as sample examination waste and is readied for ultimate disposal. As a result of the material size reduction and the packaging employed, the concentration of special nuclear material contained in a given amount of waste becomes sufficiently low that it meets the criteria for Nuclear Material Attractiveness Level E. The testing generates crushed and broken rod segments after mechanical testing and acidic liquid waste generated by defueling for cladding total hydrogen, RCT, microhardness, SEM, and metallography. These wastes must be characterized, solidified, stabilized, and/or grouted within approved disposal packages.

The waste is packaged to meet remote-handled (RH) transuranic (TRU) waste requirements and managed as part of the ORNL enduring mission TRU waste inventory. The approach for management of the enduring mission TRU waste at ORNL is to perform critical real-time TRU waste certification activities (i.e., Visual Examination) as the waste is initially packaged, in accordance with waste certification requirements. Certification personnel support ORNL facilities on a full-time basis for certification activities to ensure compliance with established waste acceptance criteria and other key programmatic areas, such as applicable atomic energy defense activities defined in the Nuclear Waste Policy Act of 1982, Nuclear Material Control and Accountability requirements, and reduction of the nuclear material attractiveness level. The waste is moved to authorized on-site waste storage facilities, where it is stored awaiting final disposal.

Additionally, certain rods have material that was sourced from other countries and therefore have foreign obligations attached. Before being shipped off site, the rods must have these obligations removed. A request to remove the obligations has been submitted to the Nuclear Materials Management and Safeguards System; however, this request has not yet been approved. While the waste is authorized to move to on-site waste storage facilities, these foreign obligations must be removed before the shipping campaign begins.

The sample examination waste included High Burn Up fuel and four different kinds of fuel rod cladding: standard Zircaloy-4 (Zirc-4), low-tin Zircaloy-4 (LT Zirc-4), ZIRLO, and M5™, which can contain Resource Conservation and Recovery Act (RCRA)-regulated heavy metal impurities. As an example, M5 cladding can contain cadmium (≤ 0.5 ppm), chromium (≤ 150 ppm), and lead (≤ 30 ppm) impurities. However, available data indicate the waste is not expected to exceed the RCRA regulatory threshold values for toxicity [26].

In addition to evaluating the radioactive material content, the sample examination waste was evaluated prior to packaging to document that the contact dose rate was ≤ 1,000 R/hr. Sample examination waste was packaged in small (< 4 liters) vented containers, which were loaded in Lead Shield Cans and disposal drums for worker protection purposes during load-out from the hot cell.

In FY22, sample examination waste was selected from all 7 sister rods underwent destructive examination with the goal of keeping contact dose within disposal limits. 78.03 in. of the 2,280 in. total received at ORNL for sister rod testing was packaged in 4 vented cans; these cans were then packaged in the 2 shield cans and placed in the single shielded overpack (SOP), as shown in Figure 46. The SOP was then loaded in the transport canister and taken to an on-site storage facility and is awaiting shipment to a geologic repository.

Acidic waste is created when the solid fuel material is dissolved. Dissolution is required for some of the Sister Rod program examinations, including cladding total hydrogen, RCT, microhardness, SEM, and metallography. Prior to the sister rod program, the Irradiated Fuels Examination Facility did not have a formalized process for solidification and disposal of acidic liquid radioactive wastes. In FY22, a process has been demonstrated for safely neutralizing and solidifying these wastes using a commercial spill-control product (Ansul Spill-X-A ™), which has been shown in tests at ORNL to be effective on concentrated nitric

acid, as well as dilute solutions containing hydrofluoric acid. The final product is a magnesium oxide-based grout-like material that no longer exhibits the Environmental Protection Agency characteristic of corrosivity for hazardous waste. The waste process has been granted a path forward by ORNL waste specialists for disposal as TRU waste. Details of packaging and accountancy for the solidified material are being developed. Current plans are to co-package the solidified wastes with an equal volume of tested fuel rod pieces and debris together into a 55-gallon overpack drum for disposal.

In FY23, further details for solidification and disposal were developed, including the specification and development of a container that can be used for both solidification and disposal while maximizing the disposal capacity of the package. One change from FY22 is the expectation that the solidified waste will be comingled with equal volume of tested fuel rod pieces and debris – SFWST has agreed to share the tested rod material with the Isotopes program, and that work requires dissolution of all rod material. Therefore, all material will be solidified liquid waste and the volume of tested fuel rod pieces is expected to be minimal. The Isotopes program will fund the additional cost and is working to develop the required accountancy plans.

Also in FY23, ORNL waste management services expanded the on-site storage facility for SOPs, which was a required action before any additional Sister Rod SNF waste material could be loaded into SOPs from the hot cell. Sister Rod material will be removed from the hot cells after the MOX waste material is loaded into the appropriate canisters and removed from the hot cell. The Sister Rod waste material will first be dissolved as part of the Kr-85 recovery program, then will be solidified and loaded into SOPs for final disposition.

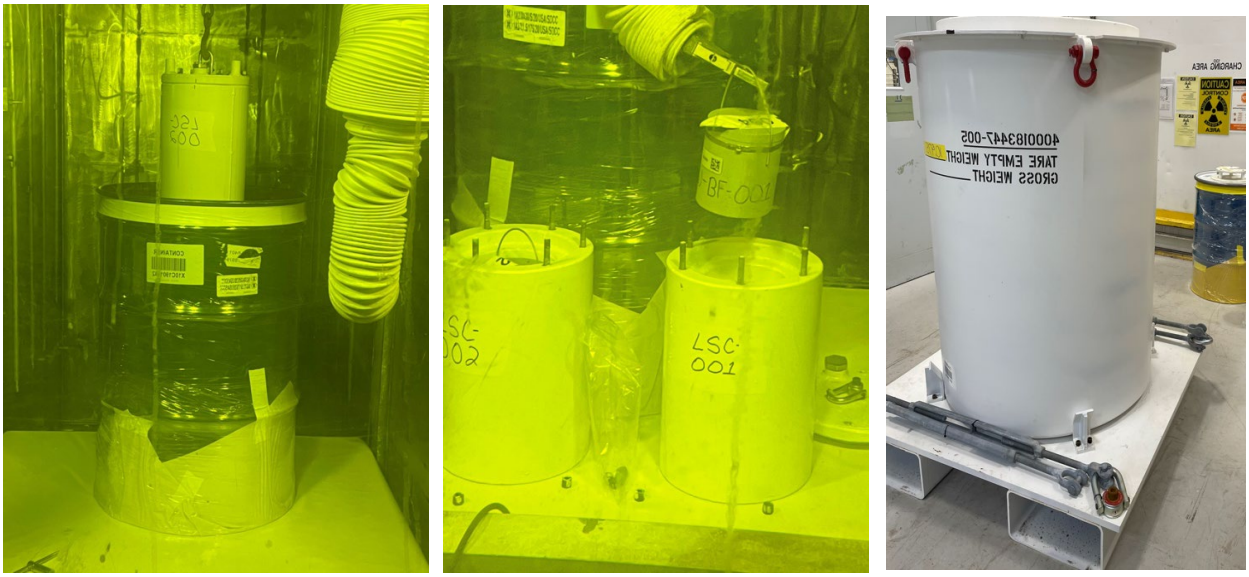

Figure 45. A shield can being loaded into a drum (left), a vented container being loaded into a lead shield can (center), and a SOP package (right).

Figure 46. Waste containers used for sister rod wastes: a drum with two shield cans (left) and a vented container for holding sample examination waste (right).

.

This page is intentionally blank.

16. Summary of Results

Table S-1 details the testing completed to date and statuses of the tests still to be completed.

To date, three fuel rods have been heat-treated: one Zirc-4-clad (F35P17), one ZIRLO-clad (3F9N05), and one M5-clad (30AE14) rod. Following FHT, the three rods were segmented along with four baseline rods, and all are being examined in detail.

Rod internal pressure, void volume, and fission gas release measurements are as expected, although it seems that the FHT has resulted in a larger void volume for the ZIRLO-clad rod. Pellet stack gas transmissibility at RT was measured, and in all cases, gas was transmissible through the pellet stack at RT, requiring between 30 min and 24 h to reach equilibrium conditions, depending upon the pressure differential applied. The data correlate well using porous media prediction models and strong correlations of porosity with pellet manufacturer, in-reactor operating temperature, and maximum in-reactor duty were identified. Comparisons of rod internal pressure and void volume measurements with predictions from fuel rod performance codes FAST and BISON indicate a tendency for FAST to overpredict void volume and BISON to underpredict void volume. Steam transmission testing was performed on discarded segments using a test system prototype. Evaluation of the system's performance indicates that over-tightening the seals with the rod segment may reduce or prevent flow to the segment, making the quantitative porosity values unreliable. However, qualitatively, the tests indicate that steam transmission along the stack is slow in comparison with inert gas and air.

Fission gas sampling and analysis yielded the expected ratio of gases; the percentage of fission gas released from the pellets to the rod void space ranges from 1.6 to 3.6% for the rods punctured. Burnup analysis results are available for three specimens, and the isotopic content of eight other samples are being analyzed.

Fueled and defueled METs are available for each of the Phase 1 rods. Additional views are in progress. Section views were inspected for hydride orientation, and radial hydrides are visible in the heat-treated M5-clad specimen and the ZIRLO-clad heat-treated specimen. There is a high hydride density in the heat-treated Zirc-4 specimen, and a large hydride blister was found in one MET view. The few radial hydrides are short. The baseline ZIRLO-clad specimen includes short radial hydrides. The other baseline specimens did not have radial hydrides.

Specimens were defueled, and the ONH analyzer was set up in preparation for total cladding hydrogen measurements. Out-of-cell verification testing of the analyzer was completed, and it was installed in a custom enclosure at IFEL. All 20 planned cladding hydrogen tests have been completed, and the specimen average cladding hydrogen content ranges from 34 to 152 wppm for M5, 130 to 616 wppm for ZIRLO, and 130 to 1,440 wppm for LT Zirc-4/Zirc-4 for the clad specimens measured. The results trend well with measured local average waterside oxide layer thickness. An axial MET was created at a pellet-pellet gap, and METs through the gap do not visually indicate a change in the hydride precipitation density. The cladding hydrogen content was measured above, below, and within the gap; the gap location has a lower hydrogen concentration than nearby areas that contacted a pellet during operation, but the cladding just below the gap has a higher total hydrogen concentration.

Thirty-one zero mean stress tests (6 static tests and 25 dynamic tests using unpressurized segments) using CIRFT were completed on 25 specimens. The results are consistent with other rods of the same type that were tested in the past but fall on the lower side of the database, especially the rods with Zirc-4 and LT Zirc-4 cladding. One dynamic test was removed from the fatigue database because, after closer examination of the data, it was determined the rod failed during the preceding static test. The heat treatments applied to selected rods resulted in a shorter fatigue lifetime, which is suspected to be the result of reduced flexural rigidity. Four non-zero mean stress tests were completed to estimate the effects of rod internal pressure on the fatigue lifetime. The results indicate that the rod internal pressure must be considered and results in a ~40% reduction in fatigue lifetime compared to the zero mean stress condition. The flexural rigidity

measured for the baseline sister rods is consistent with, although on the lower side of, previously tested 17 × 17 specimens for M5-, ZIRLO-, and LT Zirc-4 clad specimens. Based on the CIRFT data alone, the heat-treated rods have a lower flexural rigidity than the corresponding baseline rod, except the Zirc-4 clad specimens, which have a higher flexural rigidity possibly related to the design's longer pellet length. However, because of the recent calculation of large uncertainty in the CIRFT-measured flexural rigidity values (see Appendix G), there is now less certainty in these observed trends. A test on a specimen with a GTRF mark in the maximum strain location did not result in a reduced fatigue lifetime. One test remains to be completed on a specimen with multiple pellet-pellet gaps. The specimen will be tested to determine whether the gaps have an impact on the fatigue lifetime. The cumulative effects test will not be performed because the rod-to-rod or rod-to-basket impact scenario is considered unlikely. ORNL presented a strain-based fatigue lifetime limit based on the precedents established by O'Donnell in development of the historic fatigue limits established based on empty cladding and coupon tests of zirconium-based alloys. The discontinuities in the pellet cause stress concentrations on the cladding that have a detrimental effect on the fatigue life of the fuel rod compared with cladding-only performance. Defining the fatigue data in terms of strain amplitude, as opposed to stress amplitude, is concluded to be more appropriate because it is independent of the composite nature of the fuel rod and because strain is directly measured in the shipping tests that provide representative data for the expected applied fatigue cycles, which means it can be compared directly with the strain amplitude fatigue data.

All Phase 1 4PB tests are complete except for those planned for aerosol collection. Tests were conducted at room temperature (RT) and at 200°C. The flexural strength and strain at fracture, 0.2% offset yield strength, and flexural modulus were calculated for the tests completed. Generally, the heat-treated M5 and ZIRLO-clad specimens have higher ductility than the baseline specimens, but the limited data make it difficult to make any firm conclusions about whether the heat treatments affected specimen performance. The gross mass lost from the specimen during fracture was measured during the 4PB tests. There was no trend of pellet mass loss related to test temperature, although the RT fractures seemed more energetic than the 200°C fracture. The maximum mass released from the cladding represents about ¼ of a pellet, whereas the more typical 0.4 g mass released is less than ⅒ of a full pellet. The uncertainty of the 4PB test in ORNL's configuration was calculated and integrated with the results. Finite element modeling of the 4PB configuration using cracked pellet models produced a good match to test data through calibration of Young's modulus, but the simulations will be further developed to improve prediction capability. Because the major loading response of fuel rods is bending, the basic understanding of how the pellets in the rod influence rod performance will inform the simplified beam models used for transportation simulation.

ORNL tested a specimen available from a previous program in axial tension to evaluate the performance of the system setup, since PNNL had reported cladding fractures at the test clamp and extensometer grip locations. Four trials were performed, and the specimen broke every time at the clamp on the upper axial tension jaws. This indicates a sensitivity of the cladding to pressure at the clamp location and is consistent with PNNL's experience. ORNL has obtained an axial tension fixture for tubing materials and is testing it out of cell. In-cell tests with irradiated materials will begin when the load frame is replaced. ORNL's in-cell load frame succumbed to radiation damage in FY22 and is expected to be replaced in FY24.

All Phase 1 fueled RCT are complete. There is not an appreciable difference in the maximum load from RT to 200°C. Cladding type does not appear to have a large influence on the load-bearing capability either, and there does not appear to be a difference related to the heat-treatment applied to some of the rods. The main observed variant is the orientation of the major cracks in the pellet, as these appear to determine the specimen fracture plane and nucleate fracture of the adjacent cladding. Observed transverse-bearing load of the specimen is 16.4 kN (3,690 lb_f) on average, with a minimum load-bearing capability of 12.3 kN (2,766 lb_f) for the segments tested. The load-bearing capability of the fueled RCT specimen is about eight times higher than that of a defueled cladding specimen. In FY22 and FY23, finite element modeling of the RCT configuration using cracked pellet models provided insight into observations of fracture patterns during fueled RCT testing but greatly overpredicted the load-bearing capability of rods in the transverse

direction. In FY23, ORNL further refined its cracked pellet geometry and material models to improve prediction capability.

An aerosol collection system with fixturing and sampling devices was designed to characterize and quantify the respirable fraction of UO_2 particles released during rod fracture. Modified collection stages were designed and added to a commercially available Sioutas cascade to allow for collection of a larger range of particle diameters. Testing and computational fluid dynamics simulations indicate adequate performance of the system. An alternative commercially available cascade (Marple) was examined but did not provide a better sampling capability for UO_2 and was discarded. A commercially available coating was tested and was found to reduce the potential for static attraction of aerosols to the walls of the plastic test enclosure. The coating will be used for all future tests. One aerosol collection test was completed in cell with a ZIRLO-clad segment in FY21 (AERO-1), and chemical processing was completed in FY22. 4,615.85 μg of dust-type particulate was collected in the test. 494 μg was collected in the cascade sampler and is within the range of respirable AED. The total airborne release fraction is calculated as 5.8E-05 ± 4.9E-06, and the respirable fraction is 0.107 ± 0.010. A second test was performed in FY23 (AERO-2), and isotopic analysis will be completed in FY24. Four more tests with unpressurized specimens are expected to be completed in FY24. Tests using pressurized segments are planned to follow the unpressurized tests. The capability to pressurize fuel rod segments has been developed and is ready for installation in the hot cell. To facilitate completion of the tests, a small load frame called *MiniMight* was fabricated by ORNL and was installed in the hot cell in FY23. The MiniMight was used to perform the AERO-2 test.

224 microhardness indentions were completed in FY22. M5 has a lower hardness than the ZIRLO, Zirc-4, and LT Zirc-4 samples that is attributed to M5's recrystallized-annealed microstructure, as opposed to the other alloys, which are cold-worked and stress-relief annealed (CWSRA). CWSRA HV appears to be strongly correlated with estimated local burnup (as a surrogate for fluence). The same cannot be said for M5, but only three datapoints are available. Another interpretation of the HV data could be that the FHT resulted in a hardness reduction, especially for the M5 cladding.

A leach test was performed using DI water and two fractured post-CIRFT specimens. The results indicate that SNF dissolution follows a trend in which there is an initial instant release of radioisotopes of Cs, Sr, Mo, and Np, followed by a gradual matrix dissolution of U, Pu, Eu, Nd, La, Pr, Sm, and Gd. Less volatile isotopes of Ru, Rh, and Ce are dependent on matrix dissolution in order to be leached. The circumferential samples with less exposed fuel surface area leached more than the axial samples in the majority of the isotopes during the timespan studied. The PCI layer may be more vulnerable to leaching because of its increased quantity of grain boundaries and pores. In FY22, an error in the mass calculation was discovered and minor corrections were made in Appendix J.

In FY22, ORNL addressed the method of disposal of acidic liquid wastes and solid wastes, and 78.03 in. of the 2,280 in. total sister rod inventory received at ORNL was packaged and is awaiting disposal. In FY23, further details for acidic waste solidification and disposal were developed, including the specification and development of a container that can be used for both solidification and disposal while maximizing the disposal capacity of the package. Also in FY23, ORNL waste management services expanded the on-site storage facility for packaged waste, which should facilitate the disposal of more waste in FY24.

Design of a fueled burst test experiment has been deferred by the program.

REFERENCES

1. Electric Power Research Institute, *High Burnup Dry Storage Cask Research and Development Project: Final Test Plan*, contract no. DE-NE-0000593, Palo Alto, California, 2014.
2. S. Saltzstein et al., *Visualization of the High Burnup Spent Fuel Rod Phase 1 Test Plan*, SAND2018-8042-O, 2018.
3. J.M. Scaglione, R.A. Montgomery, and B.B. Bevard, Post-Irradiation Examination Plan for High Burnup Demonstration Project Sister Rods, FCRD-UFD-2016-000422 ORNL/SR-2016/111, Oak Ridge National Laboratory, 2016. (superseded)
4. R. A. Montgomery et al., *Sister Rod Nondestructive Examination Final Report*, SFWD-SFWST-2017-000003 Rev. 1 (M2SF-17OR010201021) / ORNL/SPR-2017/484 Rev. 1 (ORNL/SPR-2018/801), Oak Ridge National Laboratory, 2019.
5. B. Bourdiliau et al., "Impact of Irradiation Damage Recovery During Transportation on the Subsequent Room Temperature Tensile Behavior of Irradiated Zirconium Alloys," *J. ASTM Int.*, 7, no. 9 (2010). Paper ID JAI103006.
6. Electric Power Research Institute, *End-of-Life Rod Internal Pressures in Spent Pressurized Water Reactor Fuel*, 3002001949, Palo Alto, California, 2013.
7. R. W. Shimskey et al., *PNNL Phase 1 Update on Sister Rod Destructive Examination Results*, SFD-SFWST-M2SF-19PN010201037, Pacific Northwest National Laboratory, September 2019.
8. G. Pan et. al., "Performance Characteristics of High Burnup ZIRLO Cladding Fuel Rods," *Proceedings of TopFuel/Global Fuel Performance Meeting*, Seattle, Washington, 2019.
9. K. Geelhood, *Sister Rod Thermomechanical Modeling with FAST*, PNNL-28224, 2018.
10. S. Stimpson, *Sister Rod Predictions of End-of-Life Rod Internal Pressure and Void Volume*, ORNL/SPR-2019/1173 M4SF-19OR0102010210, Oak Ridge National Laboratory, 2019.
11. V. V. Rondinella et al., "Measurement of Gas Permeability Along the Axis of a Spent Fuel Rod," *Top Fuel 2015*, Zurich, Switzerland, 2015.
12. J.-A. Wang and H. Wang, *FY 2017 Status Report: CIRFT Data Update and Data Analyses for Spent Nuclear Fuel Vibration Reliability Study, Revision 1*, ORNL/SPR-2017/521, SFWD-SFWST-2017-000030/R1, 2017.
13. J.-A. Wang and H. Wang, *Mechanical Fatigue Testing of High Burnup Fuel for Transportation Applications*, NUREG/CR-7198/R1, 2017.
14. W. J. O'Donnell and B. F. Langer, "Fatigue Design Basis for Zircaloy Components," *Nuclear Science and Engineering* 20 (1964): 1–12.
15. K. Geelhood et. al., "Modeling Structural Loading of Used Nuclear Fuel under Conditions of Normal Transportation," *Ceramic Materials for Energy Application IV*, The American Ceramic Society, 2015.
16. P. McConnell et al., *Normal Conditions of Transport Truck Test of a Surrogate Fuel Assembly*, SAND2014-20495/FCRD-UFD-2014-000066, Revision 0.1, Sandia National Laboratories, December 2014.
17. M. C. Billone, *Ductility of High-Burnup-Fuel ZIRLO™ Following Drying and Storage*, ANL-19/14, M2SF-19AN010201011 Rev. 3, Argonne National Laboratory, June 2019.
18. NUREG-2125, *Spent Fuel Transportation Risk Assessment, Final Report*, 2014, pp. E21-22.

19. Teague, M., Saltzstein, S., Hanson, B., Sorenson, K., & Freeze, G. (2019). *Gap Analysis to Guide DOE R&D in Supporting Extended Storage and Transportation of Spent Nuclear Fuel: An FY2019 Assessment (Final Report)*, https://doi.org/10.2172/1592862

20. O. Roth et al., "Leaching of Spent Nuclear Fuels in Aerated Conditions: Influences of Sample Preparation on Radionuclide Release Patterns," *Journal of Nuclear Materials, Elsevier B V.*, vol. 527, p.151789 (2019).

21. L. Johnson et al. *Rapid Aqueous Release of Fission Products from High Burn-Up LWR Fuel: Experimental Results and Correlations with Fission Gas Release*. *J. Nucl. Mater.* 420, 54–62 (2012).

22. R. Forsyth. 97-25 *The SKB Spent Fuel Corrosion Programme An Evaluation of Results from the Experimental Programme Performed in the Studsvik Hot Cell Laboratory* (1997).

23. Not used.

24. E. A. Kalinina et al. *Data Analysis of ENSA/DOE Rail Cask Tests*, SFWD-SFWST-2018-00049/ SAND2018-13258R (2018).

25. US DOE, Airborne Release Fractions/Rates and Respirable Fractions for Nonreactor Nuclear Facilities, https://www.nrc.gov/docs/ML1307/ML13078A031.pdf.

26. DOE/SNF/REP-002 *National Spent Fuel Program, Preliminary Report Resource Conservation and Recovery Act, Characteristics of DOE-Owned Spent Nuclear Fuel DOE-SNF-REP-002*, Rev. 3.

27. S. E. Cole et al. *AREVA Optimized Fuel Rods for LWRs*. Proceedings of the Water Reactor Fuel Performance Meeting / Top Fuel 2012, (p. 230). Manchester, UK.

28. Anand M. Garde and William H. Slagle (2009). *Hydrogen Pick Up Fraction for ZIRLO™ Cladding Corrosion and Resulting Impact on the Cladding Integrity*. Proceedings of the Water Reactor Fuel Performance Meeting – WRFPM / Top Fuel 2009, (p. 268). France.

29. R. W. Shimskey et al., *PNNL FY 2021 Sibling Pin Testing Results*, M2SF-21PN010101057/PNNL-32783, Pacific Northwest National Laboratory, March 2022.

30. Wang, J.-A. et al., *FY 2016 Status Report: Documentation of All CIRFT Data including Hydride Reorientation Tests*. M2FT-16OR080202031 ORNL/TM-2016/424 , Oak Ridge National Laboratory, 2016.

31. "Regression Analysis: How Do I Interpret R-squared and Assess the Goodness-of-Fit?" https://blog.minitab.com/en/adventures-in-statistics-2/regression-analysis-how-do-i-interpret-r-squared-and-assess-the-goodness-of-fit

32. NIST, "How Can I Tell If a Model Fits My Data?" https://www.itl.nist.gov/div898/handbook/pmd/section4/pmd44.htm

33. G. Radulescu, I. C. Gauld, G. llas, and J. C. Wagner. *An Approach for Validating Actinide and Fission Product Burnup Credit Criticality Safety Analyses—Isotopic Composition Predictions,* NUREG/CR-7108, ORNL/TM-2011/509, 2012, https://www.nrc.gov/docs/ML1211/ML12116A124.pdf

34. Penn State, "The Coefficient of Determination, R-Squared," https://online.stat.psu.edu/stat462/node/95/

35. R. D. Canaan, J. D. Couch, J. S. Delashmitt, J. M. Giaquinto, C. Hexel, G. Ilas, T. Keever, S. C. Metzger, J. D. Partridge, J. D. Roach, K. T. Rogers, N. A. Zirakparvar. *Analytical Report for*

Nuclear Regulatory Commission High Burnup Fuel Specimens, ORNL/TM-2022/2788, Oak Ridge National Laboratory (2023). https://www.osti.gov/servlets/purl/1923161